Analysis and Optimization of Monolithic RF Downconversion Receivers

Christopher D. Hull

Electrical Engineering and Computer Sciences
University of California at Berkeley

Technical Report No. UCB/EECS-2009-51
http://www.eecs.berkeley.edu/Pubs/TechRpts/2009/EECS-2009-51.html

April 26, 2009

Analysis and Optimization of Monolithic RF Downconversion Receivers

by

Christopher D. Hull

B.S. (University of California at San Diego) 1987
M.S. (University of California at Berkeley) 1989

A dissertation submitted in partial satisfaction of the

requirements for the degree of

Doctor of Philosophy

in

Engineering-Electrical Engineering
and Computer Science

in the

GRADUATE DIVISION

of the

UNIVERSITY OF CALIFORNIA at BERKELEY

Committee in charge:

Professor Robert G. Meyer, Chair
Professor Edward A Lee
Professor Heinz O Cordes

1992

The dissertation of Christopher D. Hull is approved:

_____

Chair Date

_____

Date

_____

Date

University of California at Berkeley

1992

Analysis and Optimization of Monolithic RF Downconversion Receivers

by

Christopher D. Hull

Doctor of Philosophy in

Engineering-Electrical Engineering and Computer Science

University Of California at Berkeley

Professor Robert G. Meyer, Chair

Design considerations for the front-end of radio-frequency receivers are presented. Emphasis is on silicon bipolar technology for receivers in the 1-3 GHz frequency range, though theoretical principles derived apply over a broad range of frequencies. Basic mixer and amplifier topologies are presented and their performance characteristics are analyzed. Analytic expressions for noise and distortion in linear amplifiers are presented. The performances of different topologies are compared.

A new method of noise analysis for mixers is presented. The noise analysis is applied to the emitter-coupled pair mixer over a wide range of parameters variation to allow the designer to understand how noise performance changes with parameter variations. Results of distortion simulations over a range of parameters values are also presented. The mechanisms that create the distortion are explained, and the simulations results are presented in a way that allows an intuitive link between the simulated value of the distortion and the mechanism that creates that distortion.

For verification of the methodology presented, the analysis techniques are applied to a specific circuit and compared to measured values. Computed values are close to the measured ones.

Abstract Approved: _____

Thesis Chairman

Chapter 1: Introduction

Wireless communication is a convenient way to transmit voice or data from point to point, and is essential for mobile communications. Commercial applications include cellular telephony, global-positioning satellite, direct-broadcast satellite, and wireless computing. A block diagram of a radio-frequency *transceiver* structure used for wireless communication is shown in Figure 1.

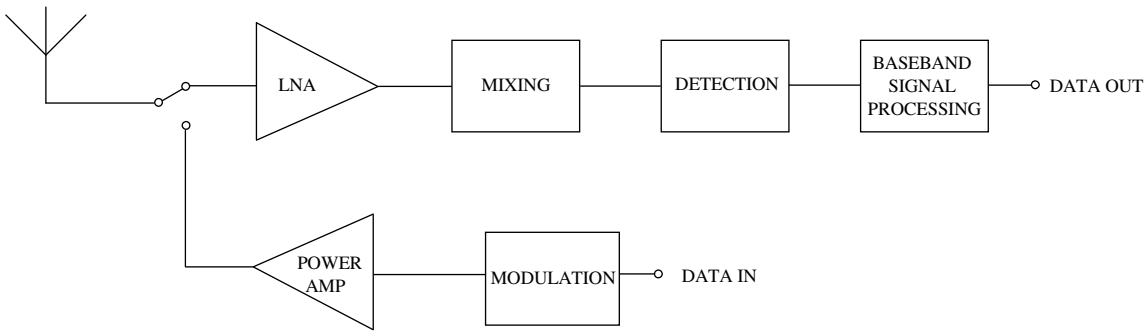

Figure 1: Low-Power Transceiver Architecture

The modulator and power amplifier blocks form the *transmitter.* The LNA (low-noise amplifier), mixer, detection circuitry, and baseband signal processor form the *receiver.* The receiver *front-end* consists of the LNA and mixing blocks. The purpose of these blocks is to amplify the weak signal received from the antenna and convert the carrier frequency down to a range that is more easily processed. Detection and baseband signal processing techniques are dependent on the type of transmission modulation (e.g. AM,FM,QPSK). The front-end of the receiver will be the focus of this dissertation.

1.1: System Requirements for Commercial RF Receivers

Among the important design considerations are power consumption, cost, physical size, reliability, selectivity and dynamic range. Selectivity is the ability of a receiver to select the desired signal and reject the unwanted signals. Dynamic range is the ratio of the maximum signal level the receiver can tolerate with an acceptable level of distortion over the minimum signal level before noise makes detection impossible.

In addressing the design considerations, one must consider the technologies available. Current technology choices are monolithic circuits vs. discrete circuits, silicon vs. gallium-arsenide, and bipolar junction transistors vs. field-effect transistors.

Monolithic technology offers the advantages of compact size, higher reliability, and lower assembly costs. However, discrete designs are easier to adjust. Monolithic implementations involve considerable start-up costs, and thus are appropriate for high-volume commercial applications. Discrete implementations are more appropriate for custom design. It should be noted that most systems use a combination of discrete and monolithic elements.

While GaAs technology offers state-of-the-art performance and is widely used for military applications, its high cost and low yield make it appropriate where performance is of paramount importance. The relatively low cost and high yield of silicon technology make large scale integration practical. This gives silicon a substantial advantage for high-volume commercial applications.

In silicon technology, bipolar transistors offer higher performance than FET devices. While FETs have comparable device gain-bandwidth products (f_T), they require substantially higher gate-source operating voltages than the base-emitter operating voltage of a bipolar transistor. Associated with this is a much lower transconductance-to-current ratio. For low-power applications (both low current and low voltage) the BJT offers considerably better performance. An alternative for FETs is to operate them at low gate-source voltages. While use of low gate-source voltages improves the transconductance-to-current ratio, the high-frequency current gain and f_T drop considerably, and the parasitic capacitances become quite large. As FET sizes scale down, FETs may become practical alternatives to bipolar transistors in the low GHz range. However, in the current 0.8 micron technology, the performance of FETs suffers drastically beyond a few hundred MHz. One of the major advantages of FET technology is the ability to integrate with CMOS digital circuitry. However, with the advent of BiCMOS technology, it is not necessary to sacrifice performance for integration. It should be noted that PMOS transistors give far better performance than the parasitic PNPs available in many bipolar and BiCMOS processes. These may be quite useful for active loads and biasing.

1.2: Front-end Receiver Architecture

Figure 2 shows a block diagram of an RF receiver front end. Image rejection, IF (intermediate frequency), and loop filters are off chip, since high Q inductors are not currently available in monolithic technology. The LNA output and mixer input must be matched to the impedance of the image filter (often 50Ω). The VCO, divider, XCO (crystal controlled oscillator) and loop filter form a frequency-multiplying *phase-lock loop*. An external crystal provides a stable reference frequency. The frequency divider in the feedback loop of the phase-locked loop yields a frequency multiplication of the reference. Often the frequency divider is controlled digitally, allowing f_o to be varied by digital control. This is convenient when the receiver is to be used to decode a number of input channels that are separated in frequency (*frequency-domain multiplexing*).

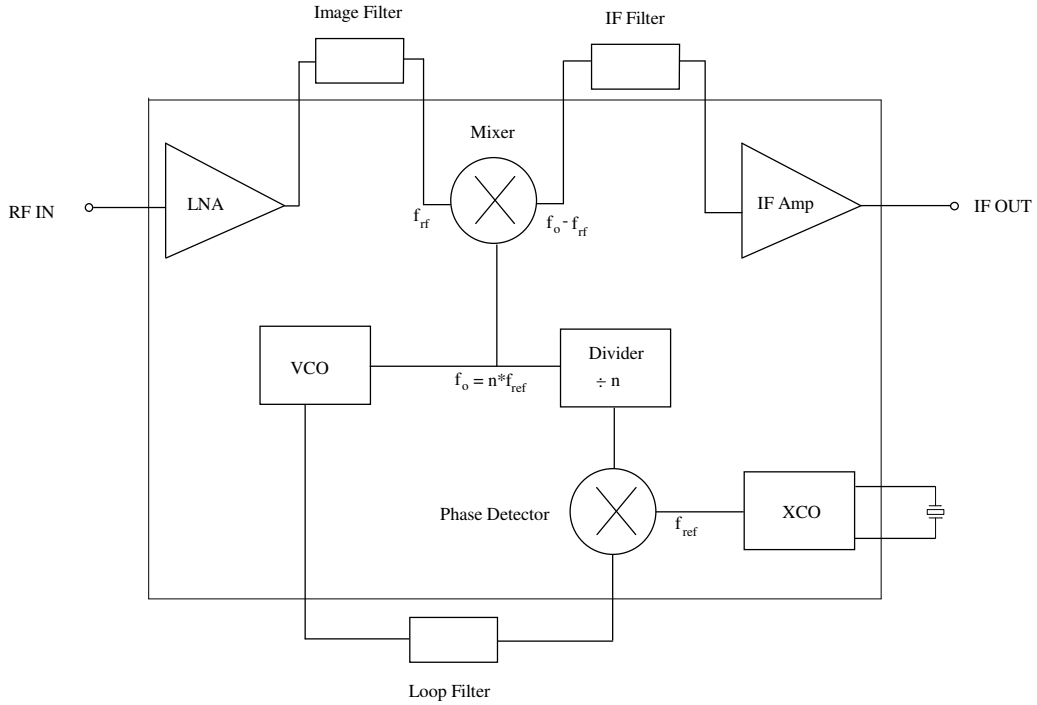

Figure 2: Simplified RF Front End Receiver Architecture

Chapter 2: Circuit topology for RF Amplifiers and Mixers

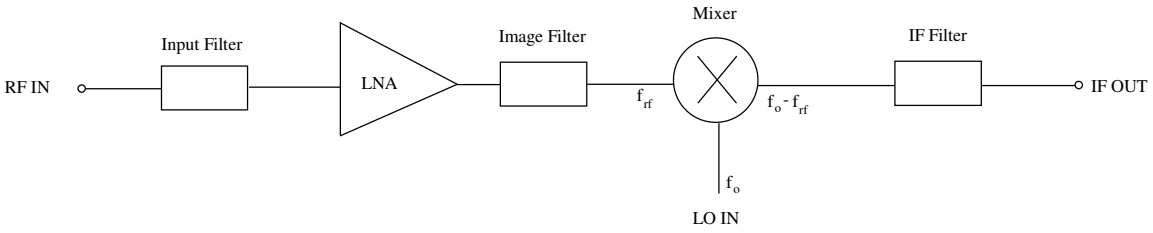

Figure 1: RF Amplifier and Mixer

Figure 1 shows the arrangement of the RF amplifier and the mixer, which together with the local oscillator, form the front end of the receiver. An input filter is necessary to prevent overload of the LNA from out of band signals coming from the antenna, and also improves image rejection. Since the amplifier and mixer take their inputs and outputs from off chip, they must have matched impedances at both the inputs and the outputs. Impedance matching networks may be used for this purpose. If an *image-rejection mixer* is used, then use of an image filter between the preamp and mixer is unnecessary, and hence, the output impedance of the LNA and input impedance of the mixer need not be matched. Image-rejection mixers require twice the hardware and power consumption of an equivalent mixer that does not reject the image frequency. Thus there is a tradeoff between the advantage gained from the increased level of integration of an image-rejection mixer and the increased power consumption.

2.1: Low-Noise Amplifier Configurations

Of the three basic configurations (common-emitter, common-base, and common collector), the common-emitter (or common-source for FETs) is the only one offering both current and voltage gain. This is quite advantageous for noise purposes. Hence, the first stage of any low noise amplifier is almost always a common-emitter. At high frequencies the common-emitter has a low input and output impedance making it suitable for matching to the lower impedances typically seen in RF filter systems, cables, and antennas.

Common-base stages offer low input impedances, but very high output impedances, and a matching network is necessary at the output of a common-base stage. Shunt feedback may also be used to reduce the output impedance, but has limited applicability at high frequencies, as the excess open-loop gain required to give adequate loop gain is not readily available. Multiple stages may be used to obtain the required loop gain, but stability issues generally limit the number of stages to two or three. Common-collector stages are commonly used at low frequencies; however, at high frequencies, the output impedance is quite inductive and the configuration is prone to parasitic oscillations. For these reasons, common-emitter amplifiers are preferred for high-frequency matched impedance applications that are narrow-band.

A typical two stage configuration is depicted in Figure 2. Matching networks should be made of reactive elements to avoid adding additional noise sources to the circuit. In particular, "brute force" matching with series or shunt resistors should be avoided, as this degrades the noise performance of the amplifier substantially. The bias network uses negative feedback to stabilize the dc operating point of the transistors.

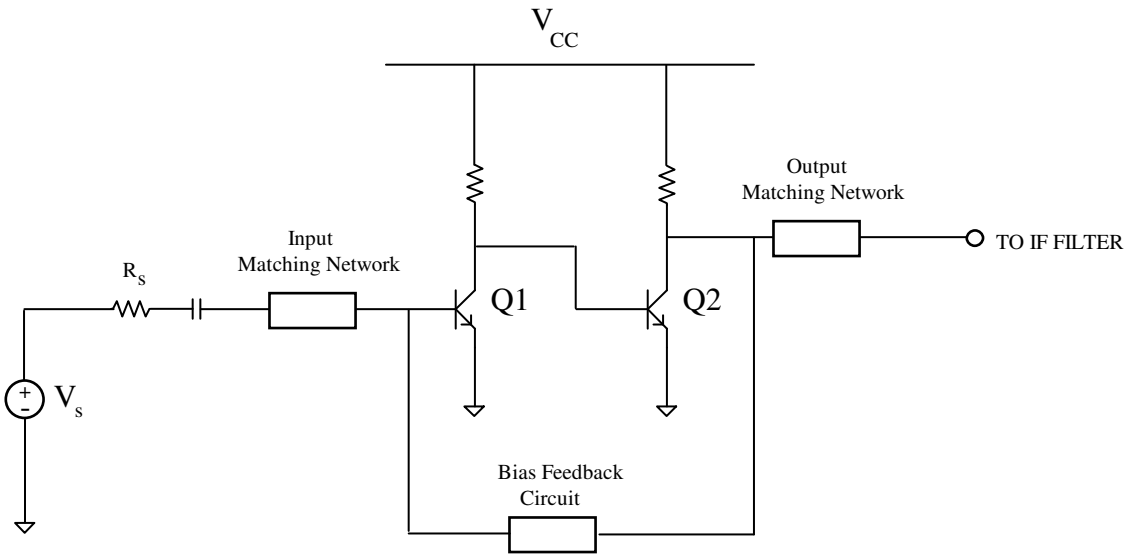

Figure 2: Two-stage low-noise amplifier

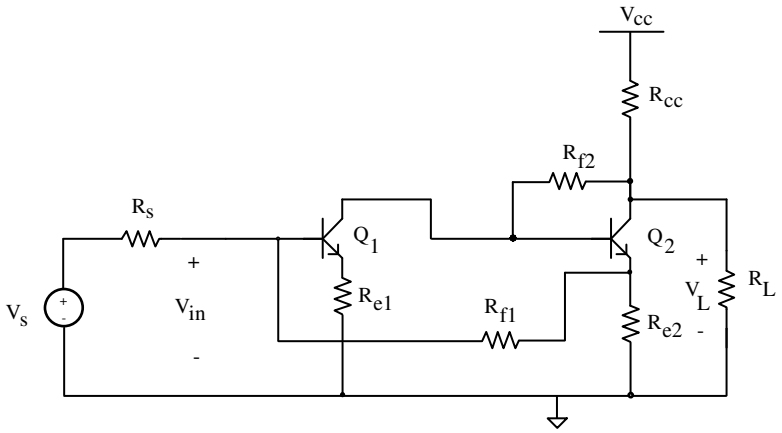

Figure 3: Wideband Matched-Impedance Amplifier

An alternative matching technique is to use feedback. An example of this circuit is shown in Figure 3. The advantage of this technique is that matching occurs over a wide range of frequencies. This is desirable for general purpose amplifiers. However, feedback amplifiers generally have poorer noise (especially at high frequencies) compared to non-feedback amplifiers. This dissertation will focus on topologies that do not use feedback.

2.2: Mixer Configurations

A wide variety of mixer configurations are possible. Fundamentally, all mixers rely on periodic switching of the signal for down conversion. This is shown schematically in Figure 4.

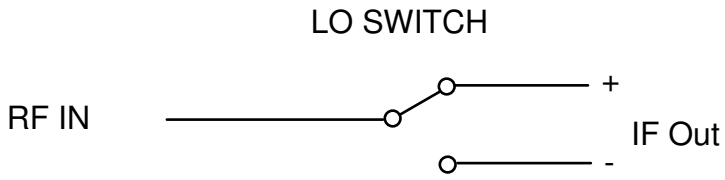

Figure 4: Fundamental Down Conversion Process

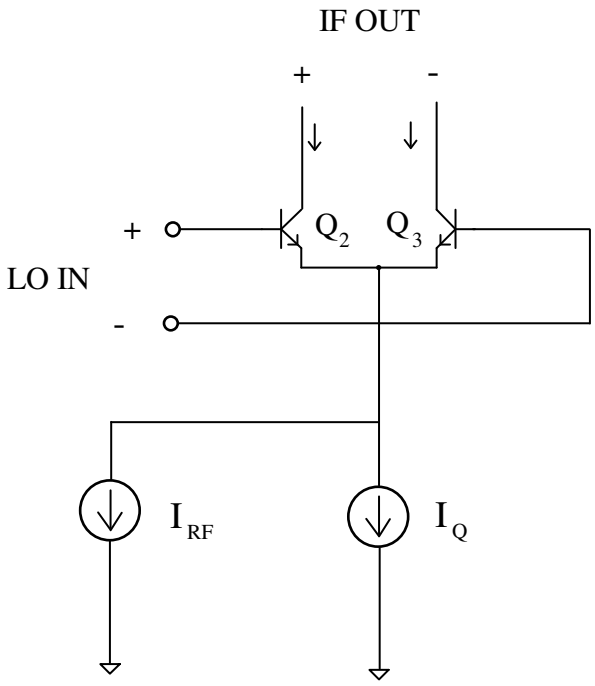

Figure 5: Emitter-Coupled Pair Mixer

In bipolar technology the switch is usually implemented using an emitter-coupled pair as shown in Figure 5. Note that an input signal in the form of a current is required. This implies that the switch should be driven with a high source impedance. Since the impedance looking back into the IF filter tends to be low, a voltage to current conversion stage is necessary. These stages must be matched at the input and have a high output impedance. Of the three basic circuit configurations, both the common-base and the common-emitter have the desired properties.

Figure 6 shows a common-base driver for the emitter-coupled pair mixer. Resistor R_m matches the circuit and linearizes the circuit, but also increases the noise of the circuit. In addition, the common-base stage lacks current gain and thus the current noise from the emitter-coupled pair mixer is referred back to the input without reduction. An alternative is to use an active matching network at the input. This will increase the current gain and reduce the noise, but the distortion will also increase.

The common-emitter configuration in Figure 7 has the advantage of better noise performance and higher gain than the common-base. At low frequencies the linearity is quite poor. However, in the GHz

range, the linearity of a well designed common-emitter amplifier may be quite good (see Chapter 3). Stable biasing is obtained by generating a reference V_{BE} using a diode.

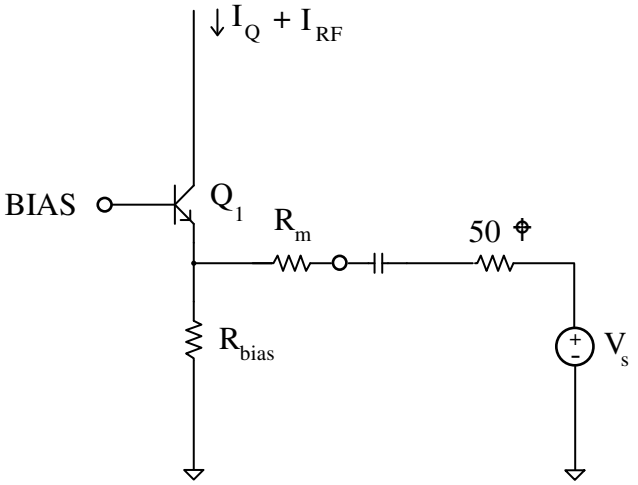

Figure 6: Common-Base Driver

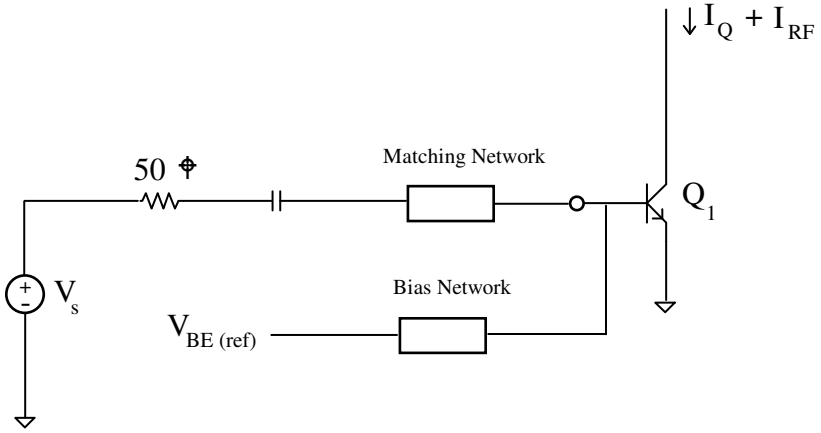

Figure 7: Common-Emitter Driver

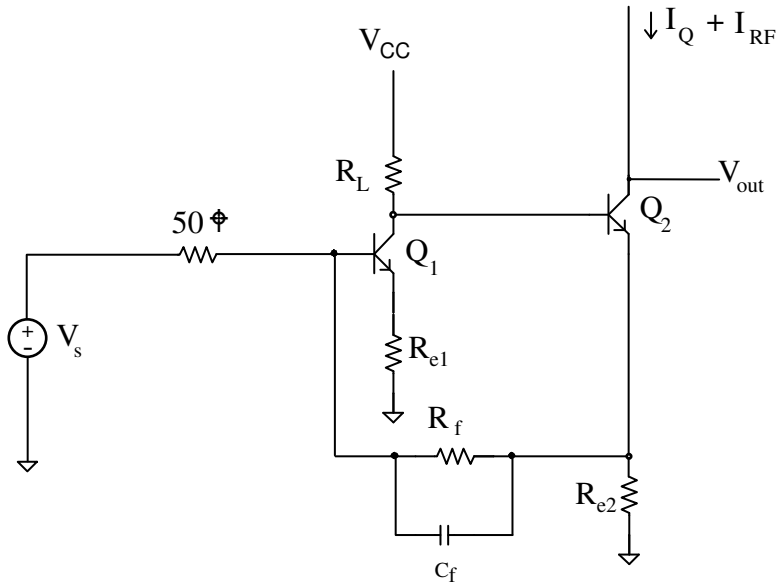

Figure 8: Current-Feedback Pair Driver

As with preamps, the driver stage of a mixer may use feedback to generate matching over a wide range of frequencies. The current-feedback pair configuration shown in Figure 8 gives a controlled low-impedance at the input and a high impedance at the output. The noise performance penalty is minimal. However, the two stages give somewhat higher gain than desired and consume additional power. Increasing the degeneration resistor, R_{e1}, to reduce the gain will degrade the noise performance.

While FET mixers may be built using circuits directly analogous to the bipolar circuits presented above, an alternative exists for FETs that does not exist for bipolar transistors. With bipolar transistors, if the collector-emitter potential is dropped below about 0.2V, the collector-base junction becomes forward biased, and the base is flooded with charge (saturation). It takes a substantial amount of time for the transistor to recover from this condition. However, FETs do not exhibit this behavior. Thus, a FET can be switched on and off by changing its drain-source potential. A simple circuit configuration that achieves this is shown in Figure 9. The gate of J_2 is controlled by the LO, and this in turn controls the drain-source potential of J_1. This configuration is very advantageous since the drain region of J_1 and the source region of J_2 may be combined into a single region. No external contact to this region is necessary. This decreases

the parasitic capacitance associated with that node of the circuit. When these region areas are combined a new four terminal device known as a *dual-gate* FET is formed. Dual-gate FET mixers are frequently used in GaAs technology.

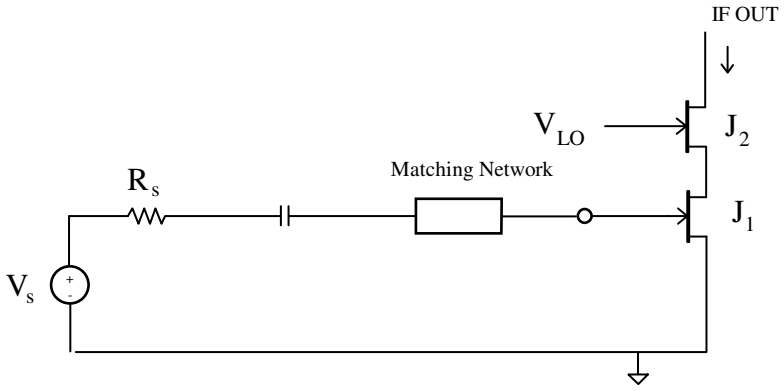

Figure 9: Complete dual-gate FET Mixer

2.3: Double-Balanced Mixers

All of the above mixers are either single-balanced or unbalanced. A single-balanced mixer allows either the RF or LO signal to pass to the output with little attenuation. A double-balanced mixer rejects both the RF and LO frequencies at the output. The fundamental configuration of a double-balance mixer is shown in Figure 10. The RF, LO, and IF ports all have balanced signals. The two switches operate in opposite polarity.

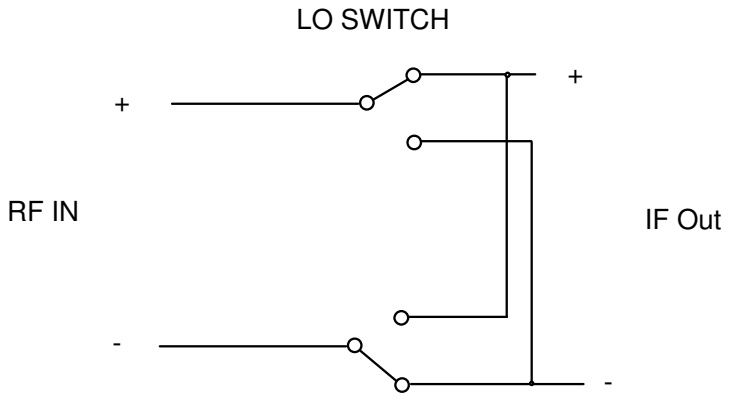

Figure 10: Fundamental configuration of a double-balanced mixer

Figure 11 shows an implementation of the double-balanced mixer using three emitter-coupled pairs. Two emitter-coupled pairs ($Q_3 - Q_6$) are used to do the switching and one (Q_1 - Q_2) is used for voltage to current conversion. The voltage to current driver is degenerated to improve its linearity. This mixer is often incorrectly referred to as a "Gilbert Cell Mixer". The Gilbert Cell adds pre-distortion techniques to achieve linear multiplication of the two input signal whereas the circuit in Figure 11 is non-linear with respect to the LO input. While analog multiplication reduces spurious output signals, the noise performance of a Gilbert Cell analog multiplier is poorer. Henceforth, the double-balanced emitter coupled pair mixer without pre-distortion will be referred to as the "Quad" mixer (since four transistors are used to perform the switching operation).

The inputs to the mixer in Figure 11 are not matched, and a matching network is required. Often "brute force" matching is used in the form of a resistor to ground. This is disadvantageous from the point of view of noise performance, but it is often the simplest way to match the RF and LO input ports.

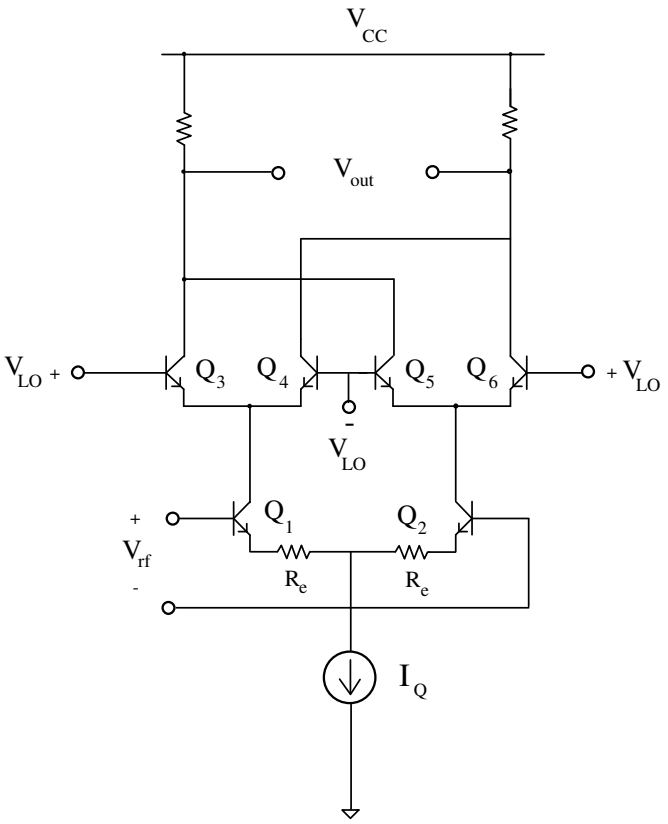

Figure 11: Double-Balanced ECP Mixer

2.4: Image-Rejection Mixers

While double-balanced mixers prevent RF and LO signals from reaching the output, spurious signals still exist. Even a mixer which performs ideal multiplication allows two different frequencies to be converted to the intermediate-frequency. For example, if the LO frequency is 1GHz, the input frequency is 900MHz, and the intermediate-frequency is 100MHz, then signals at 1.1GHz will also be converted down to the intermediate-frequency. This extra frequency that is converted down to the IF is known as the image frequency. In most mixer designs, the image frequency is filtered out with a sharp bandpass filter centered around the signal frequency. However, a combination of two mixers and two 90 degree phase shifters can be combined to form a mixer that rejects images. A block diagram of an image-rejection mixer is shown in Figure 12.

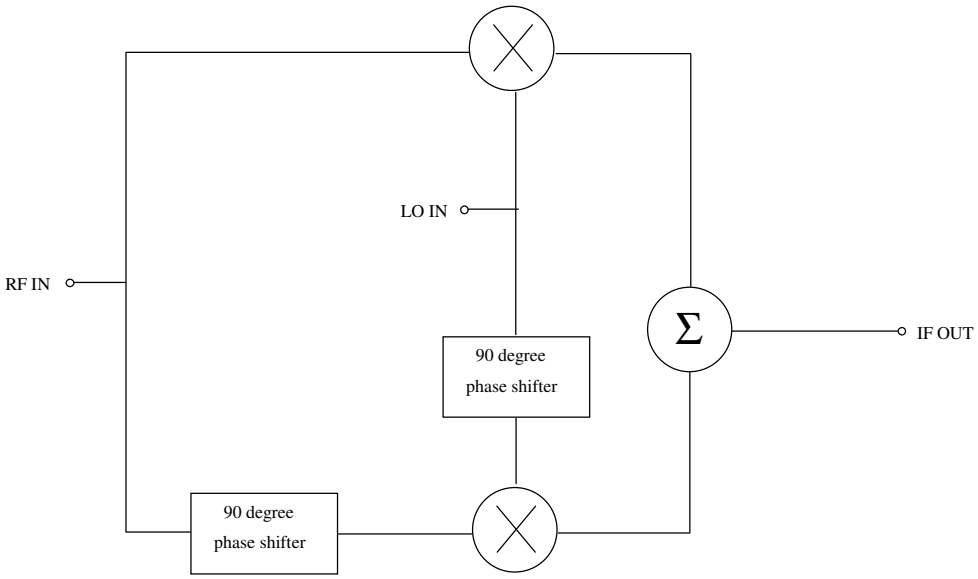

Figure 12: Image-Rejection Mixer

Chapter 3: Low-Noise Amplifiers

Random noise is generated by all resistors and active devices within a circuit. The dominant mechanisms are random thermal noise in resistors, and shot noise through p-n junctions.

Ideal reactive elements do not generate noise, though they may affect the overall noise performance in a circuit. Ideal feedback does not add noise; however, resistive feedback does add additional noise sources. For this reason, resistive feedback is to be avoided in low-noise amplifiers. Since feedback is commonly used to reduce distortion in amplifiers, designing without feedback requires that attention be paid to linearity issues. Careful design is required to obtain low noise and acceptable linearity. Resistive feedback is also commonly used to stabilize the gain and terminal impedances over wide bandwidths; however, for low noise it is necessary to use other techniques. Reactive impedance matching networks or reactive feedback may be used to obtain matching over narrow bandwidths. Generally, these techniques will not achieve a wideband match, and it is therefore necessary to have a specific frequency range in mind when designing low-noise amplifiers.

3.1: Noise Figure in Amplifiers

The most common measure of noise performance is the *noise figure* of an amplifier. The noise figure is defined as[i]:

$$F = \frac{(S/N)_{in}}{(S/N)_{out}} \tag{1}$$

S/N is the signal-to-noise ratio. The noise figure is thus a measure of the amount by which the signal-to-noise ratio is degraded. A noise figure of unity (or 0 dB) indicates a noiseless amplifier.

When two amplifiers are cascaded, the overall noise figure is given by:

$$F - 1 = F_1 - 1 + \frac{F_2 - 1}{G_1} \tag{2}$$

G_1 is the power gain of the first stage.

The noise figure of an amplifier is given in terms of its equivalent input voltage and current noise by:

$$F = 1 + \frac{\left| v_n + i_n \cdot Z_s \right|^2}{\left| v_s \right|^2} \tag{3}$$

where $$\left| v_s \right|^2 = 4 \cdot K \cdot T \cdot R_s \cdot \Delta f$$

Equation (3) is quite general, and includes the effect of correlation between voltage and current noise at the input.

3.2: Physical Noise Sources

Bipolar and FET transistors have similar small signal models at high frequencies. The small-signal model with noise sources included is shown in Figure 1. Ideal feedback does not affect the equivalent input noise generators[ii]; hence, feedback from C_{jc} does not affect the noise figure. However, the loading of C_{jc} at the input does affect the noise figure somewhat. A good first order approximation for noise calculations is to add the value of C_{jc} to C_{je}.

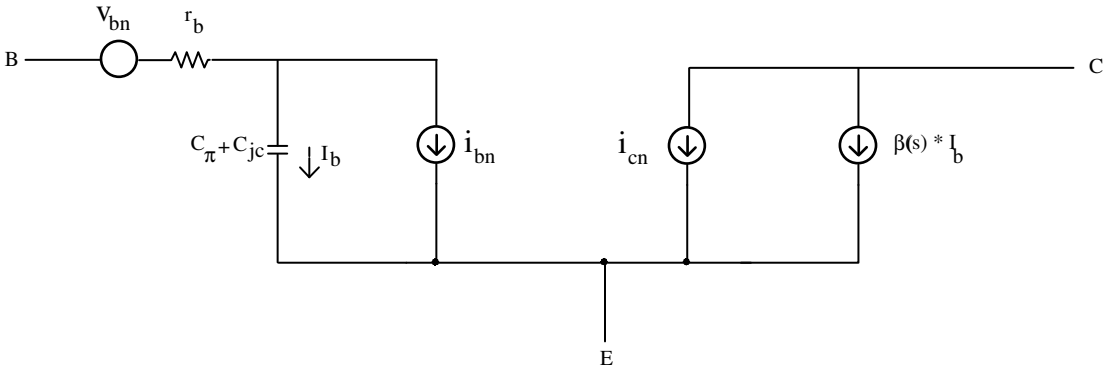

Figure 1: Transistor Model Including Noise Sources

The variances of the noise sources for bipolar transistors are given by[iii]:

$$v_{bn}^{\ 2} = 4 \cdot K \cdot T \cdot r_b \cdot \Delta f \tag{4a}$$

$$i_{cn}^{\ 2} = 4 \cdot K \cdot T \cdot \frac{g_m}{2} \cdot \Delta f \tag{4b}$$

$$i_{bn}^{\ 2} = 4 \cdot K \cdot T \cdot \frac{g_m}{2 \cdot \beta_o} \cdot \Delta f = \frac{i_{cn}^{\ 2}}{\beta_o} \tag{4c}$$

For FETs, the variances of the noise sources are:

$$v_{bn}{}^2 = 4 \cdot K \cdot T \cdot r_g \cdot \Delta f \tag{5a}$$

$$i_{cn}{}^2 = 4 \cdot K \cdot T \cdot \frac{2}{3} \cdot g_m \cdot \Delta f \tag{5b}$$

$$i_{bn} \approx 0 \tag{5c}$$

The equivalent input noise sources are expressed in terms of the three physical noise sources as:

$$v_n = v_{bn} + i_{cn}\left[\frac{1}{g_m} + \frac{r_b}{\beta(j \cdot \omega)}\right] + i_{bn} \cdot r_b \approx v_{bn} + \frac{i_{cn}}{g_m} \tag{6a}$$

$$i_n = i_{bn} + \frac{i_{cn}}{\beta(j \cdot \omega)} \tag{6b}$$

For bipolar transistors, all three noise sources play a significant role; however, for FETs, i_{cn} dominates. Flicker noise has been neglected in Equations 4-6 since it is rarely a factor at RF and microwave frequencies; however, below 100MHz GaAs MESFETs exhibit significant flicker noise.

3.3: Noise Figure in a Single Stage Amplifier

Equations 3 and 6 may be combined to determine the noise figure of a single stage amplifier in terms of physical noise sources and source impedance. The noise figure is:

$$F = 1 + \frac{v_{bn}{}^2 + i_{cn}{}^2 \cdot \left|\frac{1}{g_m} + \frac{Z_s + r_b}{\beta(j \cdot \omega)}\right|^2 + i_{bn}{}^2 \cdot |Z_s + r_b|^2}{v_s{}^2} \tag{7a}$$

If the complex source impedance is written $Z_s = R_s + j \cdot X_S$, and terms that are on the order of $1/\beta_o{}^2$ are neglected, then the noise figure is given by:

$$F \approx 1 + \frac{v_{bn}{}^2 + i_{bn}{}^2 \cdot \left[(R_s + r_b)^2 + X_S{}^2\right] + i_{cn}{}^2 \cdot \left[\left(\frac{1}{g_m} - \frac{X_S}{|\beta(j \cdot \omega)|}\right)^2 + \left[\frac{R_S + r_b}{|\beta(j \cdot \omega)|}\right]^2\right]}{v_S{}^2} \tag{7b}$$

The relation: $i_{bn}{}^2 = i_{cn}{}^2 / \beta_o$ is true for FETs (as well as BJTs) if one interprets $\beta_o = I_D / I_G \to \infty$ for FETs. Therefore, Equation 7b may be written:

$$F \approx 1 + \frac{v_{bn}{}^2 + i_{cn}{}^2 \cdot \left[\left(\frac{1}{g_m} - \frac{X_S}{|\beta(j\cdot\omega)|} \right)^2 + \left[\frac{R_S + r_b}{|\beta(j\cdot\omega)|} \right]^2 + \left[\frac{(R_s + r_b)^2 + X_S{}^2}{\beta_o} \right] \right]}{v_S{}^2} \tag{7c}$$

By differentiating Equation 7c , the optimum value for source impedance may be derived. Using the relationship $|\beta(j\cdot\omega)| = g_m / (\omega \cdot C_{in})$, the optimum source resistance is given by:

$$R_{s-opt} = \sqrt{r_b{}^2 + X_s{}^2 + \left[\frac{v_{bn}{}^2}{i_{cn}{}^2} + \frac{1 - 2\cdot\omega\cdot C_{in}\cdot X_s}{g_m{}^2} \right] \cdot \left[\frac{1}{\beta_o} + \frac{1}{|\beta(j\cdot\omega)|^2} \right]^{-1}} \tag{8}$$

The optimum source reactance is:

$$X_{s-opt} = \frac{|\beta(j\cdot\omega)|}{g_m} \cdot \frac{1}{1 + \frac{|\beta(j\cdot\omega)|^2}{\beta_o}} = \frac{1}{\omega\cdot C_{in}} \cdot \frac{1}{1 + \frac{|\beta(j\cdot\omega)|^2}{\beta_o}} \tag{9}$$

In the case that $|\beta(j\cdot\omega)| << \sqrt{\beta_o}$, Equation 9 indicates that source reactance is such that it cancels the input reactance. For FETs the optimal source reactance is always equal and opposite to the input reactance.

Often it is convenient to realize the source reactance, X_S, with an inductor. The optimal value of this inductance is then given by:

$$L_{s-opt} = \frac{1}{\omega^2 \cdot C_{in} + \frac{g_m{}^2}{C_{in}\cdot\beta_o}} \tag{10}$$

3.4: Noise Figure For Bipolar Transistors:

Using Equation 7c and Equations 4a-c, the noise figure of a single-stage BJT amplifier becomes:

$$F = 1 + \frac{r_b}{R_s} + \frac{g_m\left[(R_s + r_b)^2 + {X_S}^2\right]}{2 \cdot \beta_o \cdot R_s} + \frac{1}{2 \cdot g_m \cdot R_s} \cdot \left[\left(1 - \omega \cdot C_{in} \cdot X_S\right)^2 + \left[\omega \cdot C_{in} \cdot (R_S + r_b)\right]^2\right] \quad (11)$$

The optimum source resistance and transconductance are given by:

$$R_{s-opt} = \sqrt{{r_b}^2 + {X_S}^2 + \left[2 \cdot \frac{r_b}{g_m} + \frac{1 - 2 \cdot \omega \cdot C_{in} \cdot X_s}{{g_m}^2}\right] \cdot \left[\frac{1}{\beta_o} + \frac{1}{\left|\beta(j \cdot \omega)\right|^2}\right]^{-1}} \quad (12)$$

$$g_{m-opt} = \sqrt{\frac{1}{(R_s + r_b)^2 + {X_S}^2} \cdot \frac{(1 - \omega \cdot C_{je} \cdot X_s)^2 + \left[\omega \cdot C_{je} \cdot (R_s + r_b)\right]^2}{(\omega \cdot \tau_f)^2 + \frac{1}{\beta_o}}} \quad (13)$$

To obtain the optimum noise performance, Equations 12 and 13 must be solved simultaneously. Since an analytic solution does not exist, iteration or some other numerical technique must be applied. An analytic solution exists for $\beta_o \to \infty$. In that case:

$$X_{s-opt} \to \frac{1}{\omega \cdot C_{in}} \quad (14a)$$

$$F(X_{s-opt}) \to 1 + \frac{r_b}{R_s} + \frac{\left[\omega \cdot C_{in} \cdot (R_S + r_b)\right]^2}{2 \cdot g_m \cdot R_s} \quad (14b)$$

$$R_{s-opt} \to r_b \cdot \sqrt{1 + \frac{2}{g_m \cdot r_b} \cdot \left|\beta(j \cdot \omega)\right|^2} \quad (14c)$$

$$g_{m-opt} \to \frac{C_{je}}{\tau_f} \quad (14d)$$

$$F_{opt} \to 1 + 4 \cdot (\omega \cdot r_b \cdot C_{je}) \cdot (\omega \cdot \tau_f) \cdot \left[1 + \sqrt{1 + \frac{1}{2 \cdot (\omega \cdot r_b \cdot C_{je}) \cdot (\omega \cdot \tau_f)}}\right] \quad (14e)$$

When $\left|\beta(j \cdot \omega)\right|^2 << \beta_o \Leftrightarrow f >> \frac{f_T}{\sqrt{\beta_o}}$ the limiting values given by Equations 14a-e are close to the exact solution of Equations 12 and 13. Equations 14a-d make a good starting "guess" for numerical optimization of the noise performance.

3.5: Low-Noise Amplifier Realization

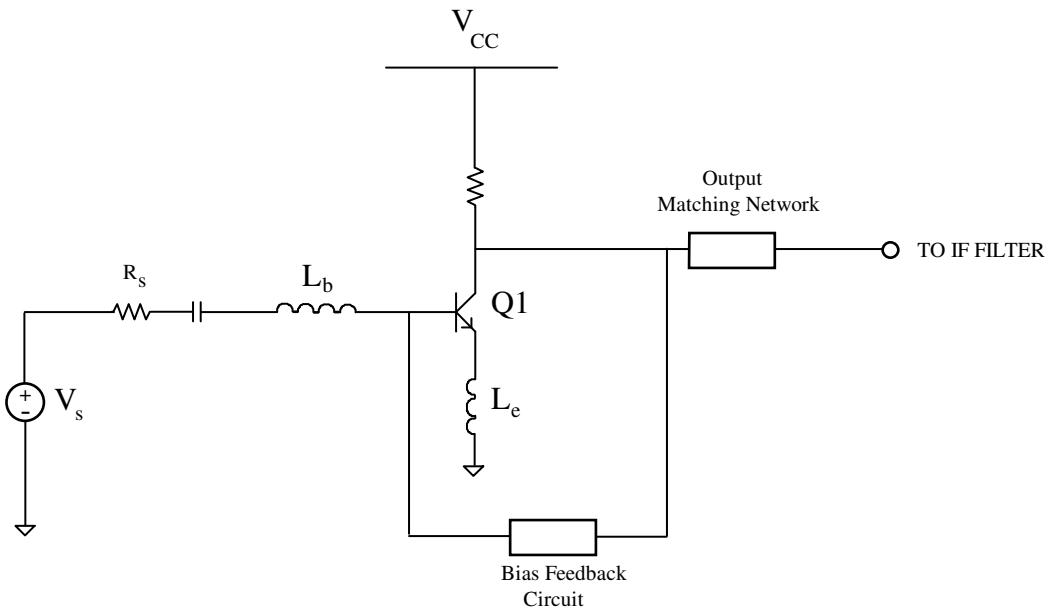

Figure 2: Single-Stage Common-Emitter Amplifier

A low-noise common-emitter amplifier is shown in Figure 2. Input matching is achieved through the use of package bond-wire inductances. Output matching may be achieved either through an external matching network or with capacitive shunt feedback.

If the collector-base junction capacitance is neglected, then the input impedance is given by:

$$Z_{in}(s) = r_b + \beta(s) \cdot \left[L_e \cdot s + \frac{1}{g_m} \right] \approx r_b + L_e \cdot \omega_T + (L_b + L_e) \cdot s + \frac{1}{C_\pi \cdot s}$$

Thus L_e gives a resistive component to the input impedance without adding noise. This allows for low-noise design, while maintaining good matching at the input. The value of emitter bond-wire inductance required for matching is given by:

$$L_e = (R_s - r_b) \cdot \tau_t \tag{15}$$

where:

$$\tau_t = \tau_f + \frac{C_{je}}{g_m} = \frac{1}{\omega_T}$$

For noise analysis purposes, the base and emitter bond-wire inductances contribute to the source reactance. Using Equation 11, the noise figure of this amplifier is:

$$F = 1 + \frac{r_b}{R_s} + \frac{g_m}{2 \cdot \beta_o \cdot R_s}\left[(R_s + r_b)^2 + \omega^2 \cdot L^2\right] + \frac{1}{2 \cdot g_m \cdot R_S}\left[(1 - \omega^2 \cdot L \cdot C_\pi)^2 + \omega^2 \cdot {C_\pi}^2 \cdot (R_S + r_b)^2\right] \quad (16)$$

$$L = L_b + L_e$$

The optimum total inductance is given by Equation 10. While Equation 12 and 13 may be used for design optimization, quite often it is easier to minimize the noise figure through direct use of an optimization package. In addition, it is often more convenient to keep the source resistance constant and allow the device area to vary. The effect of device area on current is manifested through r_b and C_{je}. Consider a process with minimum size devices having parameters: $r_b = r_{bo}$ and $C_{je} = C_{jeo}$. Then a device of area A relative to the minimum size device has:

$$r_b = \frac{r_{bo}}{A}$$

$$C_\pi = g_m \cdot \tau_f + C_{jeo} \cdot A$$

Equation 16 is then minimized with respect to A and I_c. To get a starting value for the optimization, consider the case where $\beta_o \to \infty$. Equation 14a-d can be transformed to yield:

$$A_{opt} \approx \frac{r_{bo}}{R_s} \cdot \sqrt{1 + \frac{1}{2 \cdot \omega^2 \cdot r_{bo} \cdot C_{jeo} \cdot \tau_f}} \quad (17)$$

$$I_{c-opt} \approx \frac{C_{jeo} \cdot A}{\tau_f} \cdot V_T \quad (18)$$

The first order effect of finite β_o may be taken into account via the approximation:

$$I_{c-opt} \approx \frac{C_{jeo} \cdot A}{\tau_f} \cdot V_T \cdot \frac{1}{\sqrt{1 + \frac{1}{\beta_o \cdot (\omega_o \tau_f)}}} \quad (19)$$

Equations 17 and 19 usually give values quite close to the actual optimums. Since the noise figure is not very sensitive to these parameters, it may be sufficient to use the values obtained from Equations 17 and 19 for an actual design.

3.6: Distortion in Single-Stage Amplifiers At High Frequencies:

Volterra Series techniques will be applied to the common-emitter/common-base stage to determine distortion characteristics. In particular, the third-order intermodulation distortion intercept is accurately predicted using Volterra techniques. Consider the amplifier configuration shown in Figure 3.

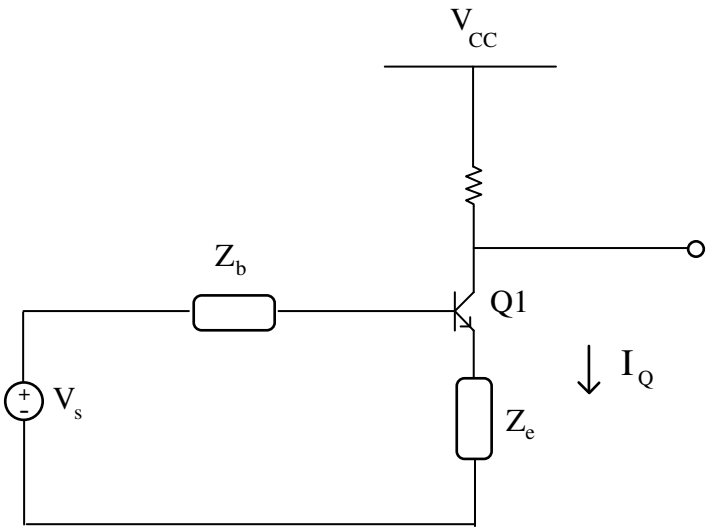

Figure 3: Common Emitter/Common-Base Amplifier Configuration

In a Volterra Series, the collector current is expressed in terms of the source voltage as:

$$i_c = a_1(\omega_1) \circ v_s + a_2(\omega_1, \omega_2) \circ v_s^{\,2} + a_3(\omega_1, \omega_2, \omega_3) \circ v_s^{\,3}$$

where the operator $\circ$ indicates that the amplitude and phase of all sinusoids in $v_s^{\,n}$ are to be modified by the magnitude and phase of $a_n(\omega_1, \omega_2, ..., \omega_n)$.

If the collector-base junction capacitance is neglected, then Volterra Series analysis gives:

$$a_1(\omega_1) = \frac{1}{Z_e(j \cdot \omega_1) + \frac{V_T}{I_Q} + Z_{be}(j \cdot \omega_1) \cdot j \cdot \omega_1 \cdot \left[\tau_f + \frac{C_{je} \cdot V_T}{I_Q} \right]} \tag{20a}$$

$$a_2(\omega_1,\omega_2)=\frac{a_1(\omega_1)\cdot a_1(\omega_2)\cdot a_1(\omega_1+\omega_2)\cdot V_T\cdot\left[1+Z_{be}\left[j\cdot(\omega_1+\omega_2)\right]\cdot j\cdot(\omega_1+\omega_2)\cdot C_{je}\right]}{2\cdot {I_Q}^2} \tag{20b}$$

$$a_3(\omega_1,\omega_2,\omega_3)=a_1(\omega_o)\cdot\left[3\cdot I_Q\cdot\overline{a_1\cdot a_2}-a_1(\omega_1)\cdot a_1(\omega_2)\cdot a_1(\omega_3)\right]\cdot\frac{V_T\cdot\left[1+Z_{be}(j\cdot\omega_o)\cdot j\cdot\omega_o\cdot C_{je}\right]}{3\cdot {I_Q}^3} \tag{20c}$$

where:
$$Z_{be}(j\cdot\omega)=Z_b(j\cdot\omega)+Z_e(j\cdot\omega)$$

$$\omega_o=\omega_1+\omega_2+\omega_3$$

$$\overline{a_1\cdot a_2}=\frac{a_1(\omega_1)\cdot a_2(\omega_2,\omega_3)+a_1(\omega_2)\cdot a_2(\omega_3,\omega_1)+a_1(\omega_3)\cdot a_2(\omega_1,\omega_2)}{3}$$

Distortion is measured in terms of the ratio of the spurious signal generated and the desired signal at the output. Spurious signals generated at the output are proportional to:

$$a_3(\omega_1,\omega_2,\omega_3)\cdot v_{s1}\cdot v_{s2}\cdot v_{s3},$$

where v_{si} is the input amplitude of the i'th input signal. The desired output signal is given by $i_o=a_1(j\cdot\omega_s)\cdot v_s$. Therefore:

$$Distortion_3\propto\frac{a_3(\omega_1,\omega_2,\omega_3)}{a_1(\omega_s)}\cdot\frac{v_{s1}\cdot v_{s2}\cdot v_{s3}}{v_s}$$

Consider the case where $\omega_3=\omega_s$ and $v_{s3}=v_s$. That is, one of the three input signals producing the distortion also produces the desired output signal.

$$Distortion_3\propto\frac{a_3(\omega_1,\omega_2,\omega_s)}{a_1(\omega_s)}\cdot v_{s1}\cdot v_{s2}$$

In this case the distortion is proportional to the signal strength of the two undesired signals.

Now consider the case where all three signals generate outputs that are desired. The output signal levels for the three desired (non-spurious) signals are:

$$i_{o1}=a_1(\omega_1)\cdot v_{s1}$$

$$i_{o2}=a_1(\omega_2)\cdot v_{s2}$$

$$i_{o3}=a_1(\omega_3)\cdot v_{s3}$$

The conventional way to measure intermodulation distortion is with equal output amplitudes:

$$i_{o1}=i_{o2}=i_{o3}=i_o$$

In this case:

$$Distortion_3 \propto \frac{a_3(\omega_1,\omega_2,\omega_3)}{a_1(\omega_1)\cdot a_1(\omega_2)\cdot a_1(\omega_3)}\cdot i_o{}^2$$

Using Equation 20a-c, it is found that:

$$\frac{a_3(\omega_1,\omega_2,\omega_3)}{a_1(\omega_1)\cdot a_1(\omega_2)\cdot a_1(\omega_3)} = \frac{\kappa(j\cdot\omega_o)}{3\cdot I_Q{}^2}\cdot\left[\frac{\kappa(j\cdot\omega_1+j\cdot\omega_2)+\kappa(j\cdot\omega_2+j\cdot\omega_3)+\kappa(j\cdot\omega_3+j\cdot\omega_1)}{2}-1\right]$$

where

$$\kappa(j\cdot\omega)\equiv\frac{1+j\cdot\omega\cdot C_{je}\cdot Z_{be}(j\cdot\omega)}{Z_e(j\cdot\omega)+\frac{V_T}{I_Q}+Z_{be}(j\cdot\omega)\cdot j\cdot\omega\cdot\left[\tau_f+\frac{C_{je}\cdot V_T}{I_Q}\right]}\cdot\frac{V_T}{I_Q}$$

Third order intermodulation distortion is defined as the distortion generated by the cubic non-linearity with two input signals. Of these signals, often the most important one is the one with output frequency given by $\omega_o = 2\cdot\omega_1-\omega_2$. For $\Delta\omega\equiv\omega_1-\omega_2 << \omega_1$, the distortion's output frequency is near the two signal frequencies.

For a constant output level for two input frequencies, the third-order difference intermodulation-distortion is given by:

$$DIM_3(\omega_1,\omega_2)=\frac{3}{4}\cdot\left|\frac{a_3(\omega_1,\omega_1,-\omega_2)}{a_1{}^2(\omega_1)\cdot a_1(-\omega_2)}\right|\cdot i_o{}^2$$

$$DIM_3(\omega_1,\omega_2)=\frac{1}{4}\cdot\left|\kappa(j\cdot\omega_o)\right|\cdot\left|1-\kappa(j\cdot\omega_1-j\cdot\omega_2)-\frac{1}{2}\cdot\kappa(2\cdot j\cdot\omega_1)\right|\cdot\left[\frac{i_o}{I_Q}\right]^2 \qquad (21)$$

The usual situation of interest is when $\omega_2\approx\omega_1-\Delta\omega,\Delta\omega << \omega_1$. The distortion frequency is $\omega_o=\omega_1+\Delta\omega$, which often falls in the signal bandwidth, and cannot be filtered out.

The distortion for this case is given by:

$$DIM_3(\omega_1,\omega_2)\approx\frac{1}{4}\cdot\left|\kappa(j\cdot\omega_o)\right|\cdot\left|1-\kappa(j\cdot\Delta\omega)-\frac{1}{2}\cdot\kappa(2\cdot j\cdot\omega_1)\right|\cdot\left[\frac{i_o}{I_Q}\right]^2 \qquad (22)$$

Using the triangle inequality, an upper bound on the distortion can be placed:

$$DIM_3(\omega_1,\omega_2) \leq \frac{1}{4}\cdot\left|\kappa(j\cdot\omega_o)\right|\cdot\left[\left|\frac{\kappa(2\cdot j\cdot\omega_1)}{2}\right|+\left|1-\kappa(j\cdot\Delta\omega)\right|\right]\cdot\left[\frac{i_o}{I_Q}\right]^2 \tag{23}$$

Now :

$$1-\kappa(j\cdot\omega)=\frac{\frac{I_Q}{V_T}Z_e(j\cdot\omega)+j\cdot\omega\cdot C_b\cdot Z_{be}(j\cdot\omega)}{1+\frac{I_Q}{V_T}Z_e(j\cdot\omega)+j\cdot\omega\cdot C_\pi\cdot Z_{be}(j\cdot\omega)}$$

where:

$$C_b=\frac{I_Q}{V_T}\cdot\tau_f$$

For $\left|1-\kappa(j\cdot\Delta\omega)\right| << \left|\kappa(2\cdot j\cdot\omega_1)\right|$ the distortion is given by:

$$DIM_3(\omega_1,\omega_2)\approx\frac{1}{8}\cdot\left|\kappa(j\cdot\omega_o)\right|\cdot\left|\kappa(2\cdot j\cdot\omega_1)\right|\cdot\left[\frac{i_o}{I_Q}\right]^2 \tag{24}$$

For $\left|1-\kappa(j\cdot\Delta\omega)\right| >> \left|\kappa(2\cdot j\cdot\omega_1)\right|$ the distortion is given by:

$$DIM_3(\omega_1,\omega_2)\approx\frac{1}{4}\cdot\left|\kappa(j\cdot\omega_o)\right|\cdot\left|1-\kappa(j\cdot\Delta\omega)\right|\cdot\left[\frac{i_o}{I_Q}\right]^2 \tag{25}$$

Consider the common-emitter amplifier in Figure 2. For this amplifier:

$$\kappa(s)=\frac{V_T}{I_Q}\cdot\frac{1+s\cdot C_{je}\cdot\left[(L_b+L_e)\cdot s+R_s+r_b\right]}{\frac{V_T}{I_Q}+L_e\cdot s+s\cdot(\tau+\frac{C_{je}\cdot V_T}{I_Q})\cdot\left[(L_b+L_e)\cdot s+R_s+r_b\right]} \tag{26a}$$

$$1-\kappa(j\cdot\Delta\omega)=\frac{j\cdot\Delta\omega\left[\frac{I_Q}{V_T}\cdot L_e+\cdot C_b\cdot(R_s+R_b)\right]-(\Delta\omega)^2\cdot(L_b+L_e)\cdot C_b}{1+j\cdot\Delta\omega\left[\frac{I_Q}{V_T}\cdot L_e+\cdot C_\pi\cdot(R_s+R_b)\right]-(\Delta\omega)^2\cdot(L_b+L_e)\cdot C_\pi} \tag{26b}$$

Note that for sufficiently small $\Delta\omega$, $\left|1-\kappa(j\cdot\Delta\omega)\right| << \left|\kappa(2\cdot j\cdot\omega_1)\right|$ and Equation 24 applies. For increasing $\Delta\omega$, $\left|1-\kappa(j\cdot\Delta\omega)\right|$ will increase. When $\left|1-\kappa(j\cdot\Delta\omega)\right| > \left|\kappa(2\cdot j\cdot\omega_1)\right|$ the distortion will begin to increase substantially. Hence, it is necessary to have sharp filtering at the input so that out-of-band

signals (which may have a wide frequency spread) do not intermodulate to produce distortion that is in-band.

The expression for $\kappa(s)$ is a two-pole, two-zero transfer function, and may be characterized by the resonance frequency and Q for the poles and zeros.

$$\omega_z = \frac{1}{\sqrt{(L_b + L_e) \cdot C_{je}}} \tag{27a}$$

$$\omega_p = \frac{1}{\sqrt{(L_b + L_e) \cdot C_{\pi}}} \tag{27b}$$

$$Q_z = \frac{1}{R_s + r_b} \sqrt{\frac{L_b + L_e}{C_{je}}} \tag{27c}$$

$$Q_p = \frac{1}{R_s + r_b} \sqrt{\frac{L_b + L_e}{C_{\pi}}} \cdot \frac{1}{1 + \frac{L_e \cdot \omega_T}{R_s + r_b}} \tag{27d}$$

In general $\omega_p < \omega_z$ and $Q_p < Q_z$ and $\kappa(j \cdot \omega)$ reaches a minimum near ω_z.

For small $\Delta\omega$, $DIM3 \propto \left|\kappa(j \cdot \omega_o)\right| \cdot \left|\kappa(2 \cdot j \cdot \omega_0)\right|$ and the minimum distortion occurs near:

$$\omega_{md} \approx \frac{\omega_z}{\sqrt{2}} = \frac{1}{\sqrt{2 \cdot (L_b + L_e) \cdot C_{je}}} \tag{28a}$$

For large $\Delta\omega$, the intermodulation distortion can be written $DIM_3(\omega_1, \omega_2) \propto \frac{1}{4} \cdot \left|\kappa(j \cdot \omega_o)\right| \cdot \left|f(\Delta\omega)\right|$, where f is some function. Assuming $\Delta\omega$ is held constant, the frequency of minimum distortion is given by:

$$\omega_{md} \approx \omega_z = \frac{1}{\sqrt{(L_b + L_e) \cdot C_{je}}} \tag{28b}$$

For both small and large $\Delta\omega$, the minimum distortion occurs between 70-100% of ω_z.

For a low-noise design $g_m \cdot \tau_f \approx C_{je}$ (see Equation 14d). Therefore $C_{\pi} \approx 2 \cdot C_{je}$. From Equation 10, the minimum optimum inductance is given by:

$$L_{opt} \approx \frac{1}{\omega^2 \cdot C_{\pi}} \approx \frac{1}{2 \cdot \omega^2 \cdot C_{je}}$$

If the impedance is matched at the input and $r_b << R_S$ then from Equation 15, $L_e \approx R_s \cdot \tau_f$. Thus for a low-noise design:

$$\omega_z \approx \sqrt{2} \cdot \omega$$

That is, the zero frequency occurs a factor of $\sqrt{2}$ above the frequency that noise was optimized for. For small $\Delta\omega$ Equation 28a implies that:

$$\omega_{md} \approx \omega$$

That is, the minimum distortion occurs near the frequency used for noise optimization. This is major advantage of the common-emitter amplifier at high frequencies. It is the only configuration that obtains low distortion and low noise simultaneously.

3.7: Design Example

Consider the circuit shown in figure 2. Suppose that the minimum size transistor available in a given process has the following parameters: $r_b = 400$, $C_{je} = 33 \cdot fF$, $\tau_f = 12ps$, $\beta_o = 100$. The design frequency is $f_o = 1\text{GHz}$. Applying Equations 17 and 19 gives the result:

$$A_{opt} \approx 71$$

$$I_{c-opt} \approx 3.1\text{mA}$$

Then Equation 10 gives:

$$L_{opt} = 5.3\text{nH}$$

$$N_{opt} = 1.20\text{dB}$$

Direct numerical optimization of Equation 10 yields:

$$I_{c-opt} = 2.9\text{mA}$$

$$A = 67$$

$$L_{opt} = 5.7\text{nH}$$

This represents a variation of only 7%. Further, the calculated noise figures for these two designs differ by only 0.002dB. Equation 15 gives the emitter bond-wire inductance for impedance matching to be:

$$L_e = 1.6\text{nH}$$

then: $$L_b = 3.7\text{nH}$$

Figure 4 shows the intermodulation distortion vs. frequency with the frequency separation kept fixed at 10MHz, and the output modulation (i_c / I_Q) at 100% . Note that the actual distortion for 100% modulation will not be equal to that given in Figure 4 since there are higher order terms in the Volterra Series. However, 100% modulation is a convenient number for reference. For example the distortion for 10% modulation will be 40dB below the levels shown in Figure 4. Notice that the minimum distortion occurs near the 1GHz design frequency.

Figure 5 shows the intermodulation distortion vs. frequency separation with ω_1 kept constant at 1 GHz. The distortion increases significantly for frequency separations greater than 100MHz.

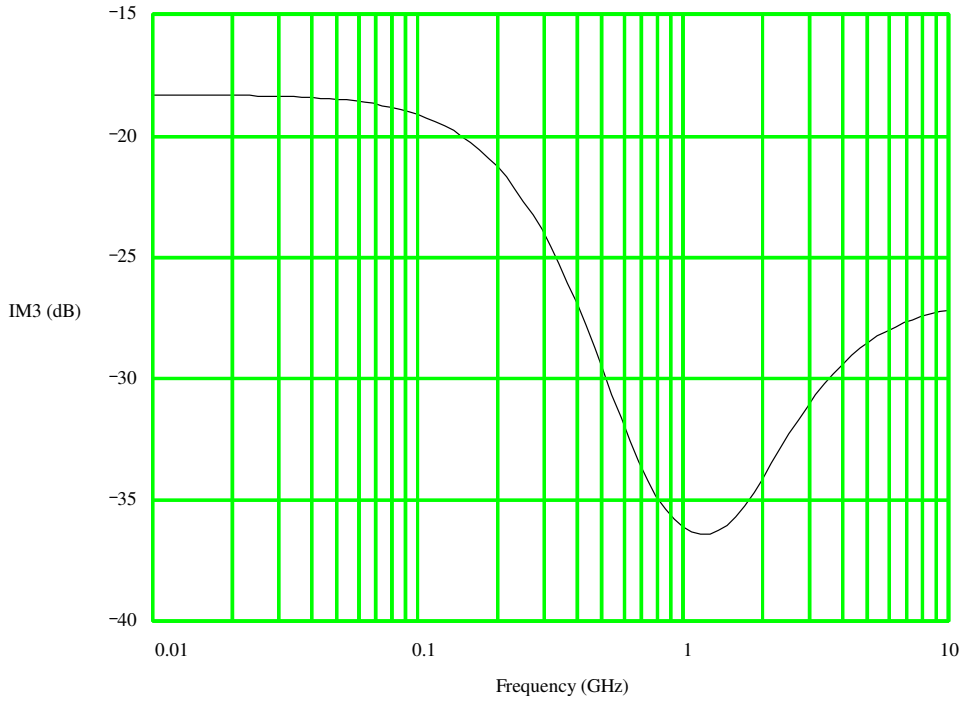

Figure 4: Distortion vs. Frequency for $\Delta\omega = 10\text{MHz} i_c / I_Q = 1$

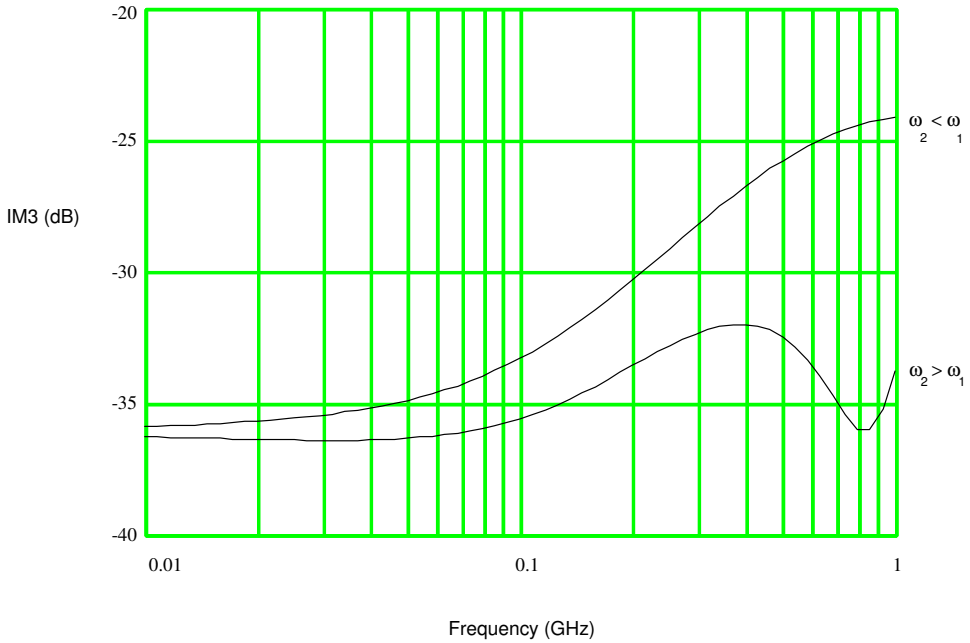

Figure 5: Distortion vs. $\Delta\omega$ for $\omega_1 = 1\text{GHz}$

Chapter 4: Monolithic BJT Mixer Design

Figures 1 and 2 are complete schematics for a monolithic BJT mixer. In Figure 1, a common-base driver is used. In Figure 2, a common-emitter driver is used. In Chapter 2, Figure 11, a double-balanced mixer using an emitter-coupled pair driver is shown.

Often the linearity and noise performance of a mixer are constrained by the driver design. The driver design also has the most significant effect on the mixer conversion gain. Thus, a logical first step in a mixer design is the selection of the driver topology. In this chapter the most common driver topologies are analyzed for gain, noise, and distortion performance.

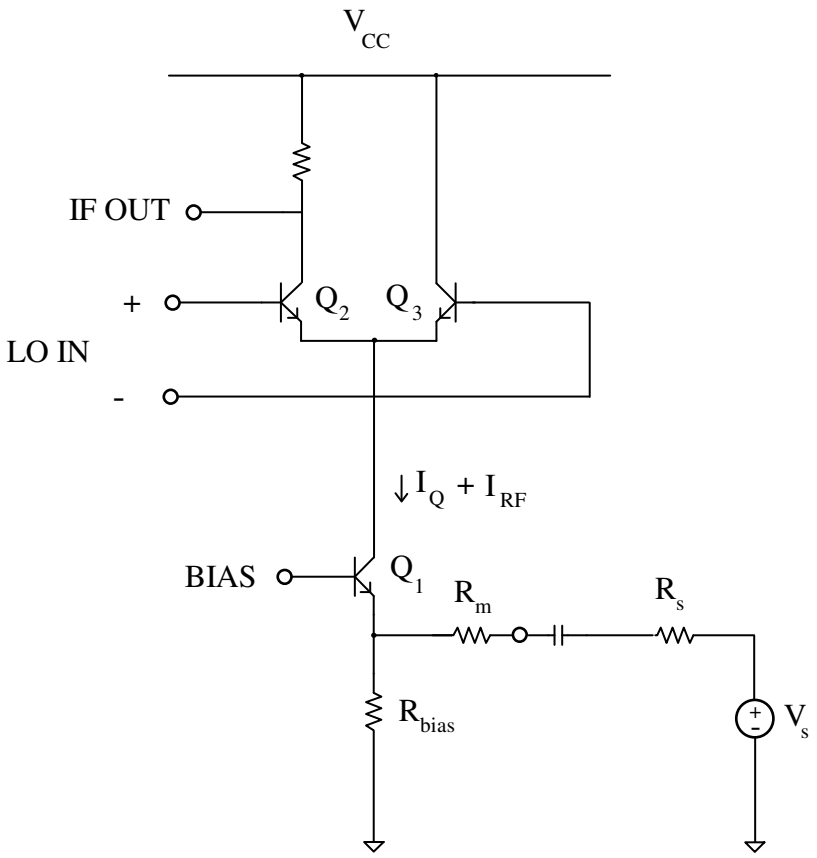

Figure 1: Emitter-Coupled Pair Mixer with Common-Base Drive

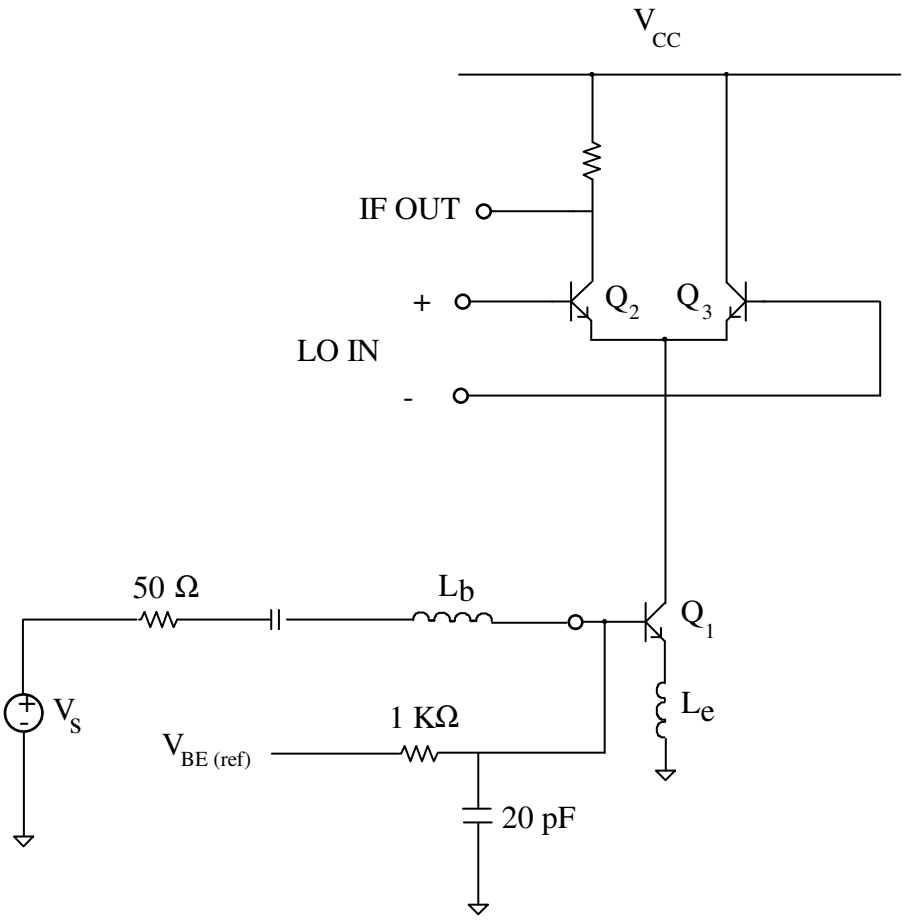

Figure 2: Emitter-Coupled Pair Mixer with Common-Emitter Drive

4.1: Common-Emitter Driver

Common-emitter drivers have the advantage of providing low noise and high gain. Also, at high frequencies, the linearity performance of the common-emitter is quite good.

The linearity of the common-emitter driver is identical to the common-emitter amplifier analyzed in Chapter 3.

The current gain of a common-emitter amplifier is given by:

$$a_i = \frac{\beta_o}{1 + \beta_o \cdot s \cdot \tau_f}$$

If the collector-base junction capacitance is neglected, then the input impedance is:

$$Z_{in}(s) = r_b + \beta(s) \cdot \left[L_e \cdot s + \frac{1}{g_m} \right] \approx r_b + L_e \cdot \omega_T + (L_b + L_e) \cdot s + \frac{1}{C_\pi \cdot s}$$

As in Chapter 3, an input match is obtained when the emitter inductance is:

$$L_e = (R_s - r_b) \cdot \tau_t$$

and the total inductance is given by:

$$L_e + L_b = \frac{1}{\omega_o{}^2 \cdot \tau_t}$$

4.2: Common-Base Driver

Common-base drivers are advantageous when wideband operation is required. Common-base stages provide a nearly constant input impedance and gain.

The input impedance of the common-base stage in Figure 1 is:

$$Z_{in}(s) = R_m + \frac{\frac{1}{g_m} + r_b \cdot s \cdot \tau_f}{1 + s \cdot \tau_f} \tag{1}$$

The current gain is given by:

$$a_i = \frac{1}{1 + s \cdot \tau_f} \tag{2}$$

Note that if $g_m \cdot r_b = 1$, the input impedance is a constant resistance that is independent of frequency. For smaller devices (which have a larger r_b) the input impedance will have an inductive component with $L = r_b \cdot \tau_f$. Broadband impedance matching is achieved when $R_m + 1/g_m = R_s$.

The distortion of the common-base amplifier is obtained by applying Equation 21 from Chapter 3 with $Z_{be} = R_s + R_m + r_b$ and $Z_e = R_s + R_m$. Therefore:

$$DIM_3(\omega_1, \omega_2) = \frac{1}{4} \cdot \left| \kappa(j \cdot \omega_o) \right| \cdot \left| 1 - \kappa(j \cdot \omega_1 - j \cdot \omega_2) - \frac{1}{2} \cdot \kappa(2 \cdot j \cdot \omega_1) \right| \cdot \left[\frac{i_c}{I_Q} \right]^2 \tag{3}$$

$$\kappa(j \cdot \omega) \equiv \frac{1 + j \cdot \omega \cdot C_{je} \cdot (R_s + R_m + r_b)}{1 + (R_s + R_m) \cdot \frac{I_Q}{V_T} + (R_s + R_m + r_b) \cdot j \cdot \omega \cdot C_\pi}$$

If $\omega << \omega_T$ and $(R_s + R_m) \cdot I_Q / V_T > 1$ then $\left|\kappa(j \cdot \omega)\right| << 1$ and the distortion can be approximated by:

$$DIM_3(\omega_o) \approx \frac{1}{4} \cdot \sqrt{\frac{1}{\left[1 + (R_s + R_m) \cdot I_Q / V_T\right]^2} + \left[\frac{\omega_o \cdot C_{je} \cdot V_T}{I_Q} \cdot\right]^2 \cdot \left[1 + \frac{r_b}{R_s + R_m}\right]^2} \cdot \left[\frac{i_c}{I_Q}\right]^2 \tag{4}$$

The first of the two terms in Equation 4 is due to the exponential relationship of voltage and current in the bipolar device. The latter term represents a distortion mechanism which gives distortion that increases linearly with frequency. At low frequencies the distortion in the common-base stage is quite low, as the nonlinear transconductance tends to be canceled by the nonlinear input impedance. At high frequencies the distortion rises, because the input impedance is linearized by C_{je} while the transconductance remains nonlinear. The distortion is 3dB above its low frequency value when:

$$\omega = \frac{1}{(R_s + R_m + r_b) \cdot C_{je}} \tag{5}$$

The distortion in the common-base is independent of $\Delta\omega$, the separation of the two input frequencies.

Distortion in the common base rises monotonically with increasing frequency. At low frequencies the distortion is quite superior to an undegenerated common-emitter configuration. However, distortion in the common-emitter stage tends to decrease with frequency (see Chap. 3, Figure 4) while distortion in the common-base increases.

It is interesting to observe the frequency at which the two configurations have equal distortion. For this calculation, bond wires are neglected. Therefore:

$$\kappa(s) = \frac{1 + s \cdot C_{je} \cdot R_{be}}{1 + \frac{I_Q \cdot R_e}{V_T} + s \cdot C_\pi \cdot R_{be}}$$

κ is the parameter used in Chapter 3. For the common-base, $R_{be} \to \infty$ (if the emitter is fed from an ideal current source) and if $\omega << \omega_T$ then:

$$\kappa_{cb}(j \cdot \omega) \approx j \cdot \omega \cdot C_{je} \cdot \frac{V_T}{I_Q}$$

and

$$IM_{3-cb} \approx \frac{1}{4} \cdot \left[\frac{i_c}{I_Q} \right]^2 \cdot \frac{\omega \cdot C_{je} \cdot V_T}{I_Q} \tag{6}$$

For the common-emitter without degeneration:

$$\kappa(s) = \frac{1 + s \cdot C_{je} \cdot (R_s + r_b)}{1 + s \cdot C_\pi \cdot (R_s + r_b)}$$

At high frequencies this can be approximated by:

$$\kappa(s) \approx \frac{C_{je}}{C_\pi}$$

And using Equation 21 from Chapter 3:

$$IM_{3-ce} \approx \frac{1}{8} \cdot \left[\frac{i_c}{I_Q} \right]^2 \cdot \left[\frac{C_{je}}{C_\pi} \right]^2 \tag{7}$$

The two stages have equal distortion for:

$$\omega = \omega_T \cdot \frac{C_{je}}{2 \cdot C_\pi} \tag{8}$$

For typical low-noise designs $C_\pi \approx 2 \cdot C_{je}$ and the distortions are equal for:

$$\omega \approx \frac{\omega_T}{4} \approx \frac{1}{8 \cdot \tau_f}$$

That is, the distortion of the common-base and common-emitter are about equal at 25% of the actual device's ω_T or 12.5% of the typical device's peak ω_T. For a modern silicon bipolar process with $\tau_f = 11pS$, the distortions of the two stages are equal at 1.8GHz.

In common-emitter stages, the bond-wire inductance will reduce the distortion significantly below that predicted by Equation 7 for frequencies near $1/\sqrt{(L_b + L_e) \cdot C_\pi}$. However, in common-base stages the bond-wire inductance has little effect on the distortion. Therefore, bond-wires may allow the common-emitter stage to exhibit lower distortion than the common base for an octave or two below the frequency given by Equation 8.

It should also be noted that the distortion of the two stages was compared for constant output current levels. Since a common-emitter stage has current gain, its input intercept will be substantially lower than its output intercept. A common-base stage has unity current-gain, thus its input intercept (when

expressed as a current) is identical to its output intercept. However, since the common-base has no current gain, a high-gain preamp is necessary for adequate overall front-end gain. If a common-emitter driver is used, a lower-gain preamp (or no preamp at all) is desirable in order to maintain an adequate third order intercept point for the front-end.

The noise figure of a common-base driver is given by:

$$F = 1 + \frac{{v_{bn}}^2 + {v_{mn}}^2 + {i_{cn}}^2 \cdot \left| \frac{1}{g_m} + \frac{Z_s + r_b + R_m}{\beta(j \cdot \omega)} \right|^2 + {i_{bn}}^2 \cdot |Z_s + r_b + R_m|^2}{{v_s}^2} \tag{9}$$

Equation 9 is almost identical to Equation 7a of Chapter 3. The reason for this is that the equivalent input noise generators are identical for all three of the basic transistor configurations (common-emitter, common-base, and common-collector).[iv] There is an additional term due to the noise of the emitter series resistor used for matching. The equations in Chapter 3 hold for the common-base so long as r_b is replaced by $r_b + R_m$.

However, distortion and matching considerations are different for the common-base than for the common-emitter. For low distortion in the common-base it is necessary that $g_m \cdot (R_s + R_m) >> 1$ and $\omega_o \cdot C_{je} \cdot V_T / I_Q << 1$. Matching requires that $R_m + 1/g_m = R_s$. Together these conditions mandate that $R_m \approx R_s$, and C_{je} must be small. These requirements are in direct opposition to the requirements for low noise.

A compromise must be made when choosing between a large device (which offers minimum noise) and a minimum size device (which offers minimum distortion). A reasonable choice is a device size that makes the two terms in Equation 4 approximately equal. That is:

$$C_{je} \approx \frac{1}{2 \cdot \omega_o \cdot R_s} \tag{10}$$

For this value of C_{je} the distortion is approximately:

$$DIM_3(\omega_o) \approx \frac{1}{4 \cdot \sqrt{2}} \cdot \frac{V_T}{I_Q \cdot R_s} \cdot \left[\frac{i_c}{I_Q} \right]^2 \tag{11}$$

Distortion is reduced by increasing the bias current.

4.3: Design Example For Common Base Driver

Suppose that the minimum size transistor available in a given process has the following parameters:

$$r_b = 400\,,\ C_{je} = 33\text{fF}\,,\ \tau_f = 12\text{ps}\,,\ \beta_o = 100\,.$$

The design frequency is $f_o = 1GHz$. Applying Equation 10:

$$C_{je} \approx 796\text{fF}$$

The device area relative to a minimum size device is then:

$$A = 24$$

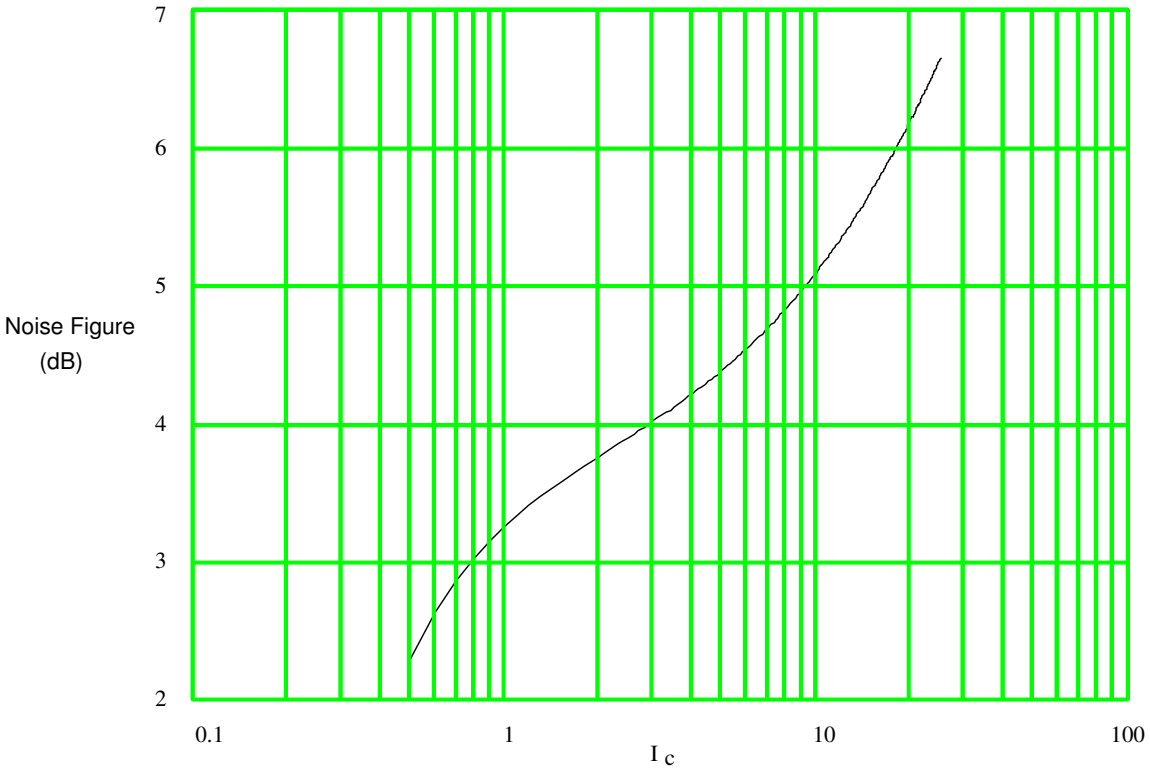

Figure 3: Noise Figure vs. Bias Current for a Common-base stage

The noise figure vs. bias current is plotted in Figure 3. Note that the noise figure, while still fairly good, is not as low as the common-emitter stage discussed in Chapter 3. This is not surprising, since the common-emitter stage was optimized for noise performance. The noise figure in the common-base increases monotonically with increasing bias current.

The third order intercept point vs. bias current is plotted in Figure 4. Note that the intercept point increases rapidly for increasing bias current. Thus, there is a tradeoff between linearity, power, and noise. The bias current should be chosen to be the minimum value that gives adequate linearity. The effect of the driver's intercept point on the system depends on the preamp gain. As the preamp gain is increased, a higher mixer bias current is required for an adequate system intercept point. Therefore, the preamp gain should not be set too high. System gain and noise considerations generally set the minimum gain of the preamps. Typically the preamp will have 15-20 dB of gain.

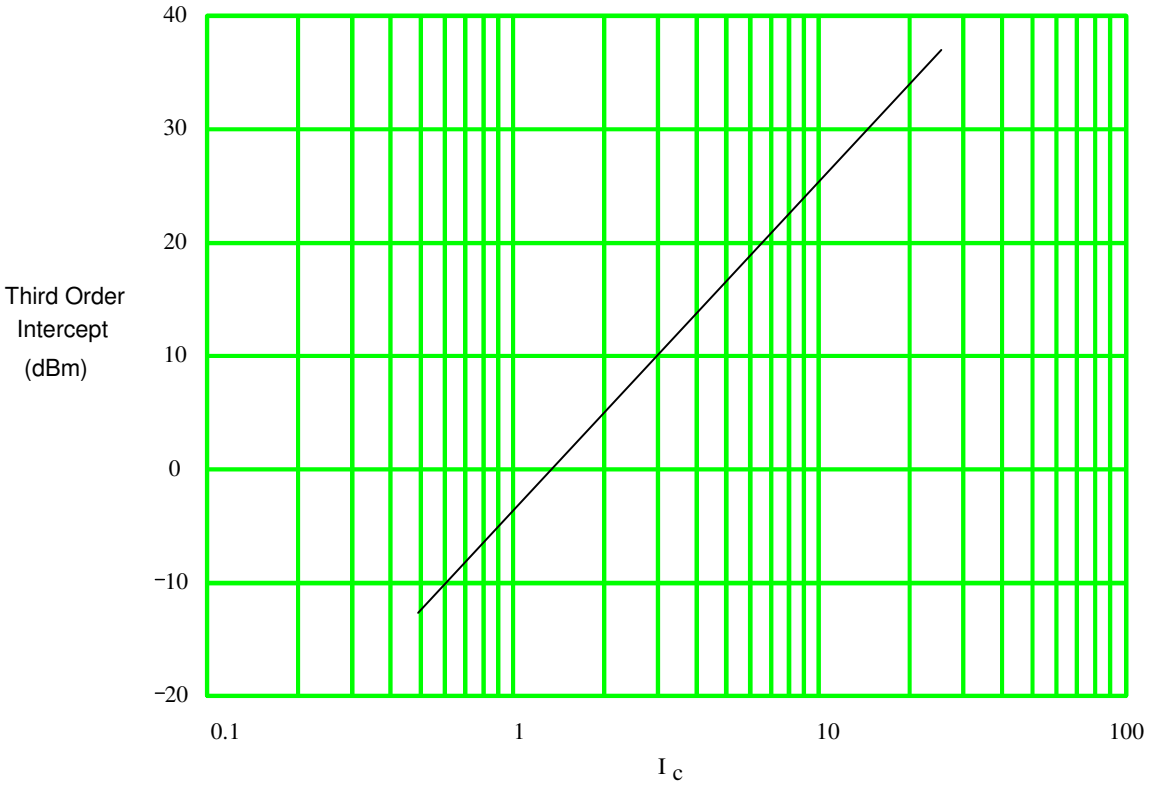

Figure 4: Third Order Intercept vs. Bias Current for a Common-base stage

4.4: Emitter-Coupled Pair Driver

An emitter-coupled pair driver is shown in Figure 5. Emitter-coupled pairs are commonly used to drive double-balanced mixers (such as the one shown in Chapter 2, Figure 11). Emitter-coupled pairs easily convert unbalanced signals to balanced signals or vice-versa. Unfortunately, the emitter-coupled pair has a

greater number of noise sources compared to a single ended amplifier; hence, it tends to have poorer noise performance. To make matters worse, it is difficult to match the emitter-coupled pair's high input impedance to a typical source impedance. It is common practice to use a shunt resistor at the input to obtain a match. Unfortunately, such a "brute-force" approach further degrades noise performance.

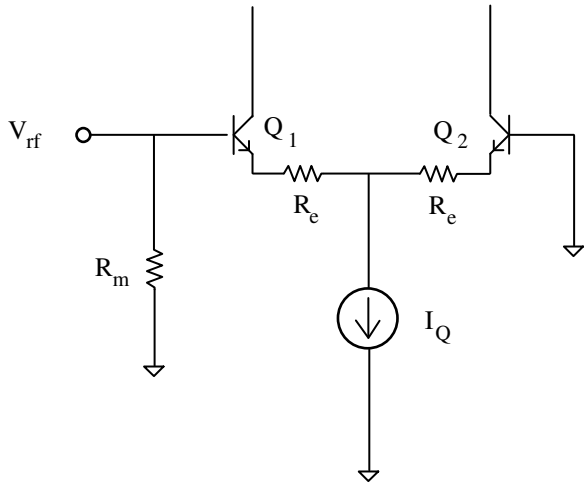

Figure 5: Emitter-Coupled Pair Driver

To quantify the effects of "brute-force" matching, suppose that the amplifier without the shunt resistor has equivalent input voltage and current noise sources v_n and i_n. Assuming that $X_s = 0$, the noise figure without matching resistor is:

$$F = 1 + \frac{\left|v_n + i_n \cdot R_s\right|^2}{\left|v_s\right|^2} \tag{12}$$

Assuming that $R_m = R_s$, the noise figure with matching resistor is:

$$F = 2 + \frac{\left|2 \cdot v_n + i_n \cdot R_s\right|^2}{\left|v_s\right|^2} \tag{13}$$

Where:

$$v_n \approx v_{bn1} + v_{bn2} + \frac{i_{cn1} + i_{cn2}}{g_m} + v_{en1} + v_{en2}$$

$$i_n = i_{bn1} + \frac{i_{cn1}}{\beta(j \cdot \omega)}$$

$$v_{en}{}^2 = 4 \cdot K \cdot T \cdot R_e \cdot \Delta f$$

That is, the effect of the voltage noise has doubled, and even if the amplifier itself is noiseless, the optimum noise figure is 3dB. In general, matching with a shunt resistor degrades optimum noise performance by 3dB, and may degrade noise performance by as much as 6 dB, if voltage noise dominates. To make matters worse, the equivalent input voltage noise in an emitter-coupled pair is twice as much as the equivalent common-emitter amplifier. The noise figure of the emitter-coupled driver shown in Figure 5 (assuming $R_m = R_s$) is given by:

$$F \approx 2 + 8 \cdot \frac{r_b + R_e}{R_s} + 4 \cdot \frac{1}{g_m \cdot R_s} + \frac{g_m \cdot R_s}{2} \cdot \left[\frac{1}{\beta_o} + \frac{1}{\left|\beta(j \cdot \omega)\right|^2} \right] \tag{14}$$

The Volterra coefficients for the emitter-coupled pair are:

$$a_1(\omega_1) = \frac{1}{2} \cdot \frac{1}{R_e + \frac{1}{g_m} + j \cdot \omega_1 \cdot \left[\tau_t \cdot (r_b + R_e) + r_b \cdot C_{je} \cdot R_e\right] + (j \cdot \omega_1)^2 \cdot \tau_t \cdot r_b \cdot R_e \cdot C_{je}}$$

$$a_2(\omega_1, \omega_2) = \frac{V_T}{2 \cdot I_Q{}^2} \cdot a_1(\omega_1) \cdot a_1(\omega_2) \cdot \frac{g_m \cdot j \cdot (\omega_1 + \omega_2) \cdot C_{je}}{g_m + j \cdot (\omega_1 + \omega_2) \cdot C_\pi}$$

$$a_3(\omega_1, \omega_2, \omega_3) = \frac{2 \cdot V_T}{3 \cdot I_Q{}^3} \cdot a_1(\omega_o) \cdot (1 + j \cdot \omega_o \cdot r_b \cdot C_{je}) \cdot (1 + j \cdot \omega_o \cdot R_e \cdot C_{je}) \cdot \left[a_1(\omega_1) \cdot a_1(\omega_2) \cdot a_1(\omega_3) - 3 \cdot I_Q \cdot \overline{a_1 \cdot a_2}\right]$$

where:

$$\omega_o = \omega_1 + \omega_2 + \omega_3$$

$$\overline{a_1 \cdot a_2} = \frac{a_1(\omega_1) \cdot a_2(\omega_2, \omega_3) + a_1(\omega_2) \cdot a_2(\omega_3, \omega_1) + a_1(\omega_3) \cdot a_2(\omega_1, \omega_2)}{3}$$

The third order difference intermodulation distortion is then:

$$DIM_3(\omega_1, \omega_2) \approx \frac{1}{4} \cdot \left[\frac{i_{od}}{I_Q}\right]^2 \cdot \left|\kappa(j \cdot \omega_o)\right| \tag{15}$$

$$\kappa(s) = \frac{(1 + r_b \cdot C_{je} \cdot s) \cdot (1 + R_e \cdot C_{je} \cdot s)}{1 + g_m \cdot R_e + s \cdot \left[(r_b + R_e) \cdot C_\pi + g_m \cdot R_e \cdot r_b \cdot C_{je} \right] + s^2 \cdot R_e \cdot C_\pi \cdot r_b \cdot C_{je}}$$

So long as $r_b << R_e$ and $\omega_o \cdot R_e \cdot C_{je} << 1$, the distortion in the emitter-coupled pair is approximately independent of the device size chosen.

4.5: Design Example For Emitter-Coupled Pair Driver

Consider an emitter-coupled pair driver that uses the same process as the common-base example. In Figure 6 the distortion is plotted vs. device area for four different values of R_e. The total bias current is 6.3mA. Since R_e represents local feedback, its effect on distortion is a function of the *loop gain*. For this feedback configuration, the loop gain is given by:

$$T = g_m \cdot R_e$$

Notice that for device sizes between 10x and 100x, the distortion is relatively independent of area.

There appear to be two ways to achieve low distortion: use a small device, or use substantial degeneration. While both approaches degrade noise performance, the latter appears to be a more viable solution.

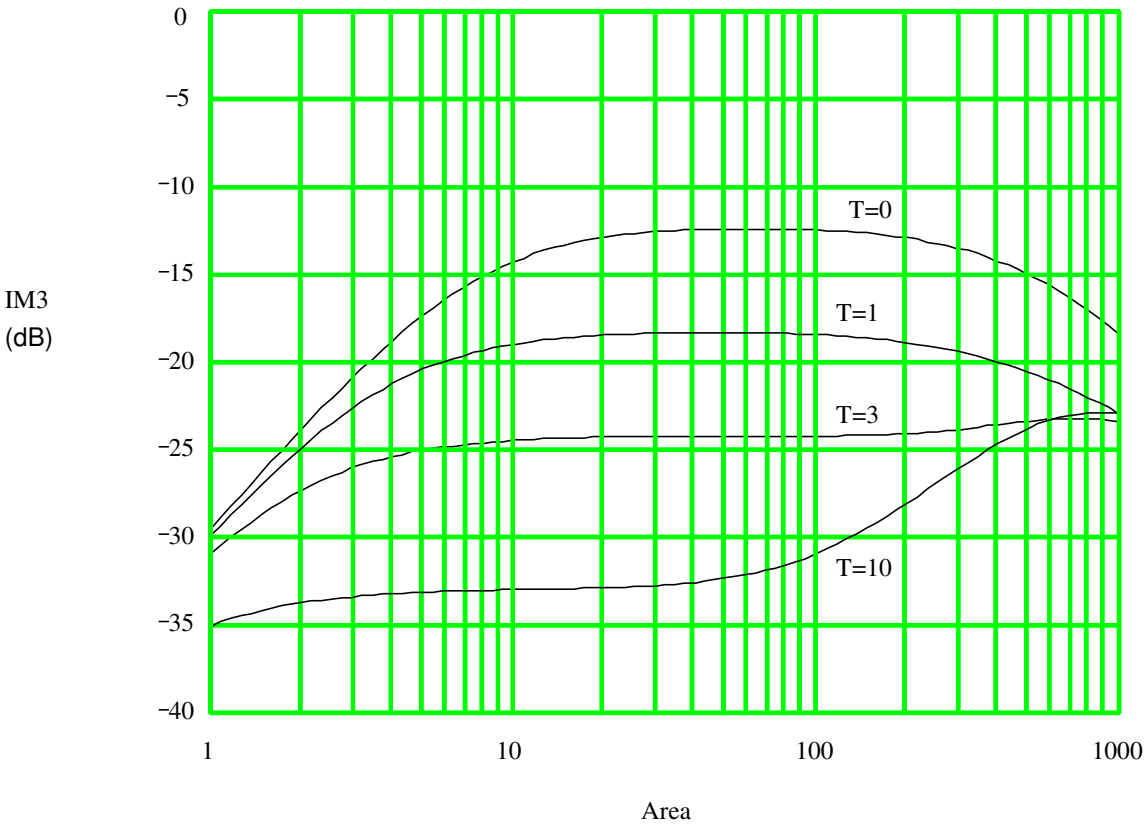

Figure 6: Distortion Vs. Device Area for an Emitter-Coupled Pair

To clarify this point, the noise figure is plotted against area in Figure 7. For small areas the noise figure is very poor. This is a result of the voltage noise multiplication of the matching resistor and the inherently higher voltage noise of the emitter-coupled pair. The optimum device area is around 150-200x, and is approximately independent of T. The optimum noise figure is between 5-10 dB depending on the amount of degeneration. A degeneration factor near 3 seems to be a good compromise, since a larger value of degeneration does not improve the distortion much, but increases the noise figure substantially.

It is interesting to compare the performance of the emitter-coupled pair stage and the common-base stage. Assuming equal total current of 6.3mA, the common-base stage has a noise figure of 4.5dB (see Figure 3) and the distortion is down 40dB for 100% modulation (see Figure 4). Using an emitter-coupled pair of area 100x (relative to the minimum size device) and degeneration factor 3, the noise figure is about 7.0dB (Figure 7), and the distortion is down only 24dB (Figure 6). Thus the dynamic range of the emitter-coupled pair is 10.5dB less than the common-base.

Clearly the emitter-coupled pair provides inferior performance to both the common-base and common-emitter amplifiers. The noise performance is the worst of the three stages. The linearity at best equals the common-base (when heavy degeneration is used). When the degeneration is reduced because of noise considerations, the linearity is much worse than the common-base. Nonetheless, the emitter-coupled pair is widely used for double-balanced mixers since it makes use of external BALUNS unnecessary.

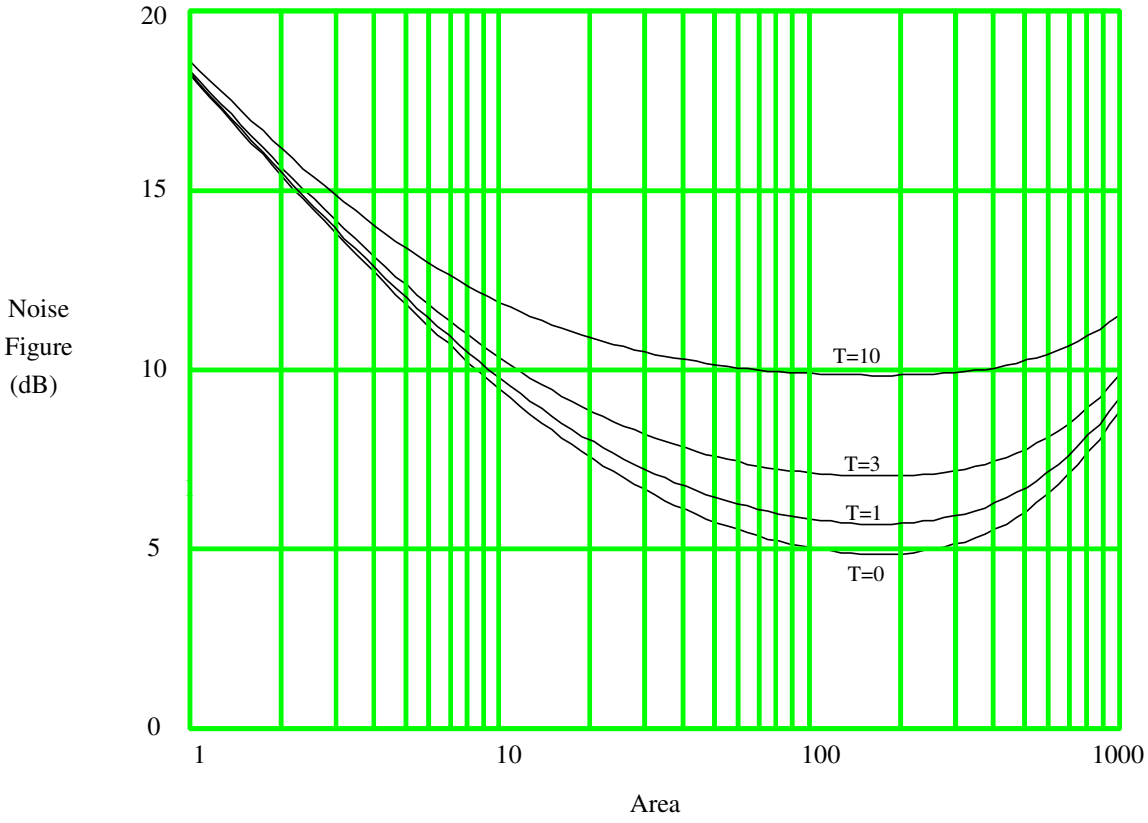

Figure 7: Noise Figure vs. Device Area for an Emitter-Coupled Pair ($I_Q = 6.3\text{mA}$)

Chapter 5: Noise Analysis of Nonlinear Circuits:

Active mixers are widely used for down conversion in UHF and microwave receivers. In contrast to passive mixers, active mixers provide gain as well as frequency conversion. A mixer is shown schematically in Figure 1. The mixer has an RF (radio-frequency) and LO (local-oscillator) input ports and an IF (intermediate frequency) output port. Ideally the mixer should produce only a scaled version of the product of the two input signals. However, real mixers add spurious signals and random noise to the desired output signal.

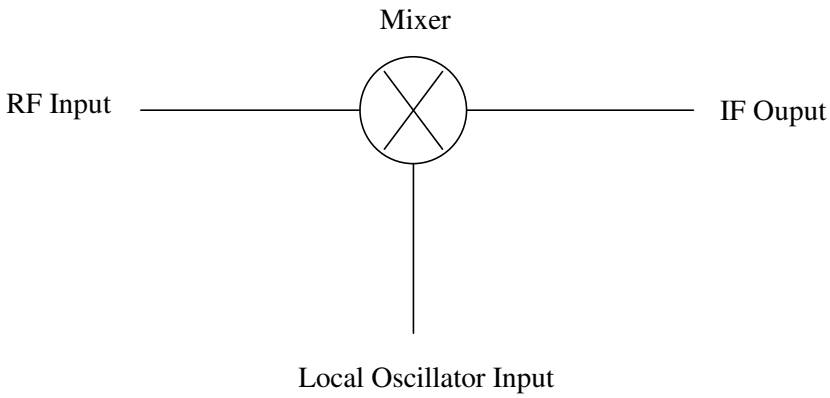

Figure 1: Basic Mixer Structure

It is desirable to be able to predict the noise performance of a given mixer design. Amplifier noise analysis techniques do not apply to mixers, because the presence of a large LO signal causes substantial change in the active devices' operating points over a period. Techniques that have been previously presented have the disadvantage that they are non-systematic, and numerically ill-conditioned.[v],[vi] Additionally, these methods fail for shot noise in the absence of a high-Q tuned circuit.

In this chapter a method is presented that is numerically efficient and well conditioned, systematic, and accurate. A significant advantage of this technique is that one simulation yields information on the mixer performance for all RF and IF input frequencies. Previously presented analysis techniques required a separate simulation for each RF input and IF output frequency of interest.[vii]

5.1: State Equations for Mixers:

It is a basic result of circuit theory that any circuit made up of elements that are either current controlled or voltage controlled can be described by a system of state equations of the form:[viii]

$$\frac{d\vec{I}}{dt} = \vec{F}\left(\vec{I},\vec{V}\right) \quad (1a)$$

$$S_{out} = C(\vec{I}) \quad (1b)$$

$\vec{I}$ is the vector of *state variables*, $\vec{V}$ is the vector of signal voltages applied to the circuit, and S_{out} is the output signal. State variables are made up of capacitor voltages (or charge) and inductor currents (or flux). In bipolar transistors, the state variable corresponding to the voltage across C_π may be replaced by the collector current through the algebraic transformation:

$$I_c = I_s \cdot (e^{\frac{V_\pi}{V_T}} - 1)$$

An alternative formulation known as *modified nodal analysis* uses node voltages and inductor currents. Then $\vec{I}$ is the vector of node voltages and inductor currents. The relationship between modified nodal analysis equations (MNA) and state variable equations is quite simple. Modified nodal analysis produces one redundant equation for each node that has no capacitive element attached to it. Despite the large matrix structure created, MNA is currently implemented in many CAD packages (e.g., SPICE) and such a formulation is desirable for integration into the computer code of such packages.

All mixers operate by use of a large LO signal that modulates the operating point of the active devices (or diodes for passive mixers) in the mixer. In the absence of RF overload, the LO is the only large signal applied to the mixer. Noise sources in the mixer can be thought of as small signals applied to an otherwise noiseless mixer circuit. Because of the large LO signal, linear noise analysis of mixers based on a fixed operating point is not possible. Analysis of mixers using available non-linear techniques is numerically ill-conditioned, since a small numerical error relative to the LO amplitude may be quite large

relative to other signals in the circuit. Hence, it is desirable to obtain a method that works independently on the large and small signals. Such a method is now presented.

Assuming a large LO signal and a small RF signal, the state equation for mixers can be written:

$$\frac{d\vec{I}(t)}{dt} = \vec{F}\left[\vec{I}(t), V_{LO}(t), v_{rf}(t)\right] \quad \text{(2a)}$$

$$S_{out}(t) = C\left[\vec{I}(t)\right] \qquad \text{(2b)}$$

Normally, the state of the mixer is determined primarily by the LO, with the RF signal causing only a small perturbation. Suppose $\vec{I}_Q(t)$ is the state vector in the absence of an RF signal (henceforth referred to as the quiescent state vector). That is, $\vec{I}_Q(t)$ is the solution to:

$$\frac{d\vec{I}_Q(t)}{dt} = \vec{F}\left[\vec{I}_Q(t), V_{LO}(t), 0\right] \qquad (3)$$

Then the state vector with the RF signal included is:

$$\vec{I}(t) = \vec{I}_Q(t) + \vec{i}(t)$$

$$\text{where:} \quad \frac{\mathrm{d}\vec{\mathrm{i}}(\mathrm{t})}{\mathrm{dt}} = \vec{F}\left[\vec{I}_Q(t) + \vec{i}(t), V_{LO}(t), v_{rf}(t)\right] - \vec{F}\left[\vec{I}_Q(t), V_{LO}(t), 0\right]$$

Using a first order Taylor Expansion of *F* about the quiescent state gives:

$$\frac{\mathrm{d}\vec{\mathrm{i}}(\mathrm{t})}{\mathrm{dt}} = \mathbf{G}(t) \circ \vec{i}(t) + \vec{h}_o(t) \cdot v_{rf}(t) \qquad \text{(4a)}$$

$$\text{where } G_{i,j} = \left.\frac{dF_i}{dI_j}\right|_{Q(t)}$$

$$\vec{h}_o(t) = \left.\frac{d\vec{F}}{dv_{rf}}\right|_{Q(t)}$$

The notation $\Big|_{Q(t)}$ is used to mean that the derivative is evaluated at the quiescent state.

A similar analysis starting with Equation 2b gives the small-signal output as:

$$s_{out}(t) = \vec{c}(t) \circ \vec{i}(t) \qquad (4b)$$

$$\text{where} \quad \vec{c}(t) = \left.\frac{dC}{d\vec{I}}\right|_{Q(t)}$$

and " ∘ " indicates matrix multiplication.

Second order Taylor expansion terms are generally negligible if the RF signal voltage (or noise voltages) is sufficiently small that nonlinearities of the circuit are not significantly excited. Because the RF signal voltages and internal noise voltages in the mixer are small, superposition applies, and each one can be analyzed separately.

Equations 4a&b are *linear time-varying equations.* The coefficients vary with time in a manner determined by the applied LO signal and the circuit configuration. If the LO signal is periodic (as is usually the case), the coefficients in Equations 4a&b become periodic and the system of equations is a *linear periodically time-varying* system or LPTV. As presented in this chapter, Equations 4a&b are derived from differentiation of the state equations of the system. However, these equations may be obtained directly from the circuit by replacing each element of the nonlinear circuit by its linear time-varying equivalent circuit.

Thus, the mixer circuit equations are solved in two steps:

Step 1: Solve the large-signal system of equations in Equation 3. The RF and noise sources are turned off (only the LO source is left on), and all of the state variables are solved as a function of time for one LO period.

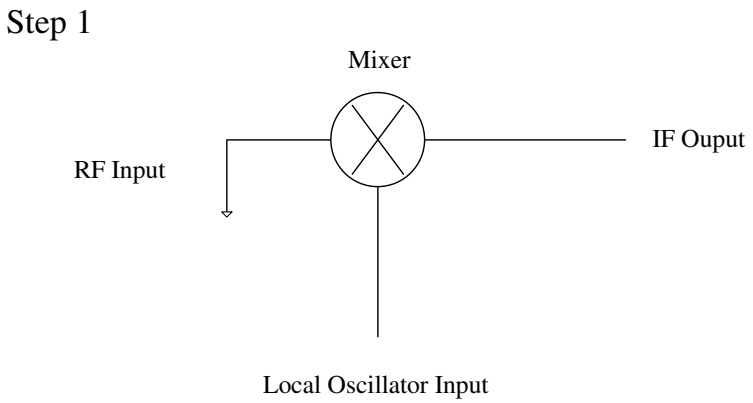

Figure 2: First step in mixer performance calculation

Step 2: Solve the small signal time-varying circuit equations (given by Equation 4, or from a linearized circuit model) for the RF signal and each noise source. Because of the linearity of Equation 4, superposition applies to each small-signal source.

The solution of step 1 is quite straight-forward. Many standard CAD packages can be used to obtain the steady state response to the LO input. The solution of step 2 is currently not implemented in any commercial CAD package. In the remainder of this chapter, two related techniques will be demonstrated for solving LPTV systems for both deterministic and stochastic input signals. The first technique is more efficient and well conditioned, while the latter is easily implemented using available CAD packages.

5.2: Equations for Linear-time Varying Systems:

For an LTV system the input-output relation is given by[ix]:

$$y(t) = \int_{-\infty}^{\infty} h(t,u) \cdot x(u) \quad du \qquad (5)$$

The input-output relation of Equation 5 is similar to the standard convolution used in a linear time-invariant system. However, the value of the impulse response is a function of both the *launch time* of the

impulse, u, and the *observation time*, t. In a time-invariant system, the impulse response is only a function of the difference between the observation time and the launch time.

$$h(t,u) = h_{lti}(t-u)$$

Under the above condition, Equation 5 reduces to the familiar convolution integral.

In an LTV system the impulse response may look quite different for different launch times. For mixers with periodic LO excitation, the impulse response is periodic in launch time, and thus can be seen as a function of the *launch phase* (the phase of the LO at launch time). In the frequency domain the relationship between the output and input spectrum is given by:

$$Y(\omega_{if}) = \int_{-\infty}^{\infty} H(\omega_{if}, \omega_{rf}) \cdot X(\omega_{rf}) \quad d\omega_{rf} \qquad (6)$$

X and Y are the Fourier Transforms of input and output signals, and H is given by:

$$H(\omega_{if}, \omega_{rf}) = \frac{1}{2 \cdot \pi} \cdot \int_{-\infty}^{\infty} \left[\int_{-\infty}^{\infty} h(t,u) e^{j \cdot \omega_{rf} \cdot u} du \right] \cdot e^{-j \cdot \omega_{if} \cdot t} dt$$

A derivation of Equation 6 is given in Appendix A.

From Equation 6 it is seen that for a general linear time-varying system, a single input frequency produces a continuous spectrum of output frequencies, not just a single output frequency as in the case of an LTI system.

For periodic LO excitations of frequency ω_o, the frequency domain equations, which are derived in Appendix B, become:

$$Y(\omega_{if}) = \sum_{n=-\infty}^{\infty} H_n(\omega_{if}) \cdot X(\omega_{if} + n \cdot \omega_o) \qquad (7)$$

where

$$H_n(\omega_{if}) = \int_{-\infty}^{\infty} \left[\frac{1}{T} \cdot \int_{0}^{T} g(v,u) e^{j \cdot n \cdot \omega_o \cdot u} du \right] e^{-j \cdot \omega_{if} \cdot v} dv \qquad (8)$$

$$g(v,u) = h(v+u,u)$$

In an LPTV system a given input frequency produces a *discrete* set of output frequencies, separated in magnitude by ω_o. The output spectrum is a linear superposition of shifted and filtered versions of the input spectrum. For each shift the frequency response of the system is given by $H_n(\omega)$, where n is the number of LO frequencies that the input spectrum is shifted.

Another point of view is that multiple input frequencies given by:

$$\left|\omega_{rf}\right| = n \cdot \omega_o \pm \omega_{if} \qquad (9)$$

are all down-converted to the IF output frequency through modulation against the n'th LO harmonic. This relationship is especially important in mixer noise analysis, since noise at a number of different input frequencies may contribute output noise at the intermediate frequency. Frequencies of particular interest are: $\omega_{rf} = \omega_{if}$ and $\omega_{rf} = \omega_o \pm \omega_{if}$ corresponding to n=0 and n=1. The latter two frequencies are the input-signal frequency and the *image* frequency. The existence of the image frequency is problematic in low noise mixer design since the noise from that frequency contributes to the output. Often the noise at the image frequency contributes equally to the noise at the RF signal frequency, degrading the noise figure by 3 dB. Input noise at the intermediate frequency can be a significant problem in *unbalanced* mixers; however, in balanced mixers the noise from the intermediate frequency is ideally canceled at the output.

For *stationary* noise the input-output relation is:

$$S_y(\omega_{if}) = \sum_{n=-\infty}^{\infty} \left|H_n(\omega_{if})\right|^2 S_x(\omega_{if} + n \cdot \omega_o) \qquad (10)$$

S_x is the input spectral density and S_y is the output spectral density.

If the input noise is white (constant spectral density), and if the output frequency is much lower than any time constants in the system, then the output spectral density can be approximated by:

$$S_{yo} \approx S_{xo} \cdot \sum_{n=-\infty}^{\infty} \left|H_n(0)\right|^2 = S_{xo} \cdot \frac{1}{T} \cdot \int_0^T \left[\int_{-\infty}^{\infty} g(v,u)dv \right] e^{j \cdot n \cdot \omega_o \cdot u} du$$

This approximation is often useful for downconversion mixers.

The impulse response function, $h(t,u)$, together with Equations 7 and 8, are sufficient to describe the small signal input-output behavior of the mixer for all possible excitations.

Since the impulse response of a mixer depends on the location of the input excitation, a separate calculation for each noise source is necessary. Often a number of noise sources can be lumped into a single source, thus reducing the number of impulse responses that must be calculated. Circuit symmetry can also be exploited to further reduce required calculation.

5.3: Obtaining the Impulse response of an LTV system

A theoretical approach that uses state equations to obtain the impulse response is presented in this section. This method, while efficient and theoretically sound, is currently not implemented in any commercially available CAD package.

Referring to Equation 4a&b, the value of the small-signal state vector and impulse response at observation times just after the launch time can be shown to be:

$$\vec{i}(u^+,u) = \vec{h}_o(t) \qquad (11a)$$

$$h(u^+,u) = \vec{c}(u) \circ \vec{h}_o(u) \qquad (11b)$$

The second argument of the function $\vec{i}$ corresponds to the launch time. For observation times t > u, the differential equation is:

$$\frac{\mathrm{d}\vec{\mathrm{i}}(\mathrm{t},\mathrm{u})}{\mathrm{dt}} = \mathbf{G}(t) \circ \vec{i}(t,u) \qquad (11c)$$

The impulse response is obtained from the linearized relation:

$$h(t,u) = \vec{c}(t) \circ \vec{i}(t,u) \quad (11d)$$

Equation 11a-d constitute a homogenous initial value problem. These equations can be solved by standard numerical ODE methods such as the trapezoidal method. The values of $\vec{c}(t)$, $\mathbf{G}(t)$, and $\vec{h}_o(t)$ are periodic, and depend on the large-signal ODE solution of Equation 3. The values of these functions are calculated over an LO period and then stored.

5.4: Fourier Transform Analysis

Once the impulse response is calculated for launch times that span the range of all LO phases, the response must be processed by a two-dimensional fast-Fourier transform to obtain the system function as given in Equation 8.

Ideally, the impulse response would be calculated for all launch times in [0,T] and for all observation times. For causal systems it is not necessary to consider observation time prior to the launch time. Since it is not possible to express a closed form solution of the impulse response for even simple mixer circuits, the impulse response values are calculated at finite intervals in both observation time and launch time. This discretization introduces *aliasing* errors. Further, it is necessary to assume that at observation time t=M+u, for some M, the impulse response decays to a negligible value. For accurate results M must be chosen to be much larger than the largest time constant in the circuit (under worst case conditions). If the interval between successive observation time points is chosen to be dV, and the interval between successive launch times is dU, then the total number of points required to describe the impulse response is:

$$N = \frac{M \cdot T_{LO}}{dU \cdot dV}$$

Clearly for a fixed value of N, there is a tradeoff between the conflicting requirements of large M, and small dU and dV. Choosing an M that is too small will cause "blurring" in the frequency domain due to convolution with a sinc function. The value of dV should be chosen to be much smaller then the inverse of the IF bandwidth, and dU should be chosen to be much smaller than the inverse of the RF bandwidth.

Choosing dU or dV too large will cause aliasing. It is best to choose M, dU, and dV to balance out the three errors, so that no single one dominates.

Often only low output frequencies are of interest. In such a case a low pass filter is placed at the output, and the sampling interval in the observation time, dV, may be made substantially larger. For simulation purposes high-Q IF filters should be avoided, since they cause the impulse response to *ring*, and thus require a very large value of M (much larger than the inverse of the IF bandwidth). A three-pole low-pass IF filter at three times the LO frequency yields a good tradeoff between accuracy and simulation time. M is usually chosen to be an LO period, and dV is chosen to be 1/32 of an LO period. The three-pole filter reduces spectral components sufficiently to prevent aliasing. Figure 3 illustrates the relationship between the grid chosen in the time domain and a corresponding grid obtained in the frequency domain after a two-dimensional FFT is performed.

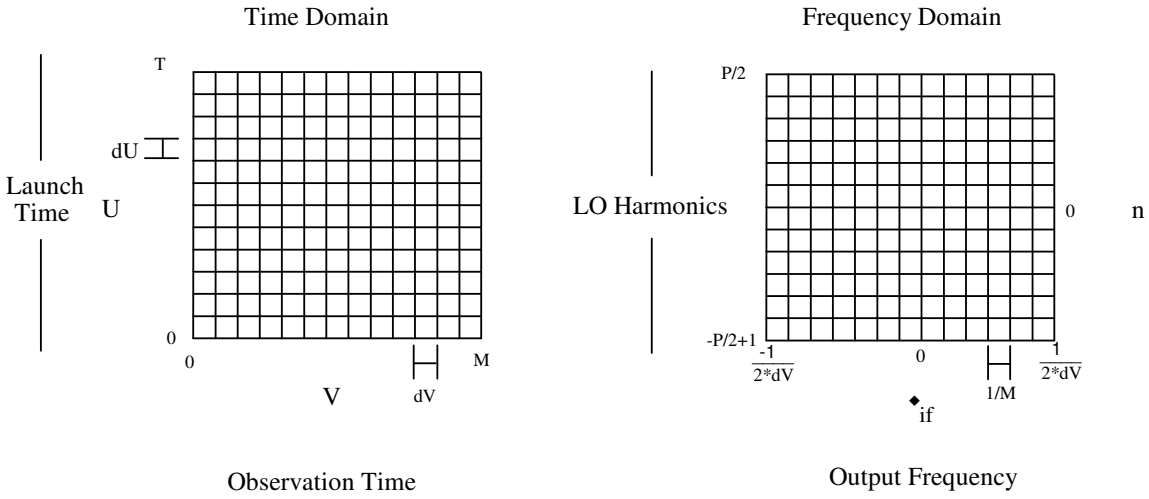

Figure 3: Grids in Time and Frequency Domain

The two dimensional FFT is obtained by calculating an FFT of the rows of h(t,u) and then an FFT of its columns. Care must be taken to observe the exponential signs and scaling factor for each direction of

the FFTs. The calculation complexity can be shown to be on the order of $N \cdot \log(N)$. Usually the time required for the FFT is small compared with the time required to obtain the impulse response.

The result of the FFT is a two-dimensional grid in the frequency domain. The axes are ω_{if} and n, where n is the number of LO frequencies by which the input spectrum has been shifted (see Equation 7). The output frequency is discretized with spacing of 1/M, and spans the range from $-1/(2 \cdot dV)$ to $1/(2 \cdot dV)$. The value of n spans -P/2+1 to P/2, where $P = T / dU$. The output spectral density is then obtained through a weighted sum of the columns:

$$S_y(\omega_{if}) = \sum_{n=-P/2+1}^{P/2} \left| H_n(\omega_{if}) \right|^2 S_x(\omega_{if} + n \cdot \omega_o) \qquad (12)$$

5.5: Summary of Steps Required to Calculate Output Noise in a Mixer

Step 1: Solve the large-signal deterministic problem:

$$\frac{d\vec{I}_Q(t)}{dt} = \vec{F}\left[\vec{I}_Q(t), V_{LO}(t), 0\right]$$

Step 2: Solve the homogenous time-varying initial value problem for $u = 0, dU, 2 \cdot dU, ..., T$, and

$$t = u, u + dV, u + 2 \cdot dV, ..., u + M$$

$$\frac{\mathrm{d}\vec{\mathrm{i}}(\mathrm{t},\mathrm{u})}{\mathrm{dt}} = \mathbf{G}(t) \circ \vec{i}(t,u) \text{ with } \vec{i}(u) = \vec{h}_o(u)$$

then:

$$h(t,u) = \vec{c}(t) \circ \vec{i}(t,u)$$

Step 3: Do a two-dimensional FFT on the impulse response:

$$H_n(\omega_{if}) = \frac{1}{T} \cdot \int_0^T \int_0^M g(v,u) e^{j \cdot n \cdot \omega_o \cdot u} e^{-j \cdot \omega_{if} \cdot v} dv du$$

$$g(v,u) = h(v+u,u)$$

Step 4: Evaluate the output noise spectrum:

$$S_y(\omega_{if}) = \sum_{n=-P/2+1}^{P/2} \left| H_n(\omega_{if}) \right|^2 S_x(\omega_{if} + n \cdot \omega_o)$$

$$P = T / dU$$

5.6: Conversion Gain and Input Referred Noise Spectral Density

The conversion gain and noise figure are also available. Recall:

$$Y(\omega_{if}) = \sum_{n=-\infty}^{\infty} H_n(\omega_{if}) \cdot X(\omega_{if} + n \cdot \omega_o) \qquad (7)$$

Therefore for first harmonic down conversion (or up conversion) the gain is simply:

$$a_{ic} = \frac{Y(\omega_{if})}{X(\omega_{rf})} = H_{\pm 1}(\omega_{if}) \qquad (13)$$

The +/- is chosen depending on the relative relationship of the RF and LO frequency. If the RF frequency is above the LO frequency than +1 is used, whereas if the RF frequency is below the LO frequency than -1 is used. For low IF frequencies, there is negligible difference between the H_1 and H_{-1}.

The input referred noise is then:

$$S_{eq}(\omega_{if}) = \frac{S_x(\omega_{if})}{\left| H_{\pm 1}(\omega_{if}) \right|^2} \qquad (14)$$

5.7: Simplified Low Frequency Theory

First consider the case where the intermediate-frequency is sufficiently low so that $\omega_{if} \cdot \tau_{\max} << 1$.

Where $\tau_{\max}$ is the longest time constant in the circuit. In this case, Equation 8 simplifies to:

$$H_n(\omega_{if}) \approx H_n(0) = \frac{1}{T} \cdot \int_0^T \left[\int_0^\infty h(v,u)dv \right] \cdot e^{j \cdot n \cdot \omega_o \cdot u} du$$

The conversion gain is:

$$H_1(\omega_{if}) \approx \frac{1}{T} \cdot \int_0^T \left[\int_0^\infty h(v,u)dv \right] \cdot e^{j \cdot \omega_o \cdot u} du$$

If the noise source is white, with spectral density S_{xo}, then Parseval's theorem can be used to express the output spectral density as:

$$S_{yo} = \frac{S_{xo}}{T} \cdot \int_0^T \left[\int_0^\infty h(v,u)dv \right]^2 du$$

In the case where $\omega_o \cdot \tau_{\max} << 1$, further simplifications are possible. Because the LO period is much longer than the impulse settling time, the input-output relation can be approximated by:

$$y(u) = h(u) \cdot x(u) \qquad (15)$$

The distinction between launch time and observation time is no longer necessary, as the only time when anything is observed is the launch time. This is a valid approximation when the impulse response duration is much less than the time it takes for the mixer circuit to significantly change its state. In other words, for this approximation to be valid, none of the large-signal state variables may change significantly over the decay time of the impulse response. The impulse response, $h(u)$, may be thought of as the gain from the RF port (or point of the noise source) to the IF output port. The gain is a function of the LO phase. In the frequency domain the input-output relationship and the output noise spectral density are:

$$Y(\omega_{if}) = \sum_{n=-\infty}^{\infty} H_n \cdot X(\omega_{if} + n \cdot \omega_o) \qquad (16)$$

$$S_y(\omega_{if}) = \sum_{n=-\infty}^{\infty} |H_n|^2 \cdot S_x(\omega_{if} + n \cdot \omega_o) \qquad (17)$$

where,

$$H_n = \frac{1}{T} \cdot \int_0^T h(t) e^{j \cdot n \cdot \omega_o \cdot t} dt \qquad (18)$$

If the input noise spectrum is white then the output noise spectrum is white, and its density is given by:

$$S_{yo} = S_{xo} \cdot \frac{1}{T} \cdot \int_0^T h^2(t) dt$$

The H_n's are the Fourier coefficients of the gain vs. time and are independent of the IF frequency. The gain vs. time is obtainable using small-signal analysis. The operating point at each launch time is held fixed. In the absence of charge storage elements, the analysis is drastically simplified. However, it is still necessary to solve a large-signal problem. Strictly speaking, this method is accurate only when the LO and output periods are much longer than the longest time constant in the circuit. However, the qualitative characteristics of a mixer at high frequencies often resemble those at low frequencies. Therefore, much information can be obtained by a simple low frequency analysis.

5.8: Results

Currently, no CAD package is available to implement steps 2-4 of the above method, although a modification in SPICE that currently works for the most rudimentary transistor models has demonstrated the feasibility of a full implementation. In the interim, a technique that uses the standard SPICE to produce results is used. This technique is presented below.

A single long transient run is performed. The LO signal is applied as well as a periodic pulse signal at either the RF port or at a location where significant noise sources exist. The period of the pulse is slightly longer than an LO period, so that the LO phase changes by dU for each launch:

$$T_{pulse} = T_{LO} + dU$$

The simulation is run for a total of P pulse periods:

$$t_{simulation} = P \cdot T_{pulse} = P \cdot T_{LO} + P \cdot dU = (P+1) \cdot T_{LO}$$

P is chosen to be sufficiently large so as to avoid aliasing problems, as discussed in the section on Fourier transform analysis. Typically a value in the range of 64 to 256 is adequate. Before the pulse launching begins, several LO cycles must be passed through in order to let the mixer settle into steady state. It is assumed that the impulse response of the circuit settles to a negligible value within a single pulse period. If this is not the case, a longer pulse period must be chosen, with a corresponding increase in simulation time. The response of each simulation period corresponds (approximately) to the impulse response of the mixer at evenly stepped LO phases.

I n order to minimize the number of data points in the observation time, a three-pole maximally flat IF filter at three times the LO frequency is used. With this filter it is necessary to sample 32 data points per pulse period for 0.1% accuracy. Additionally, the impulse response of this filter settles to within 0.1% of the impulse height within an LO period, indicating suitability for the above technique. The response roll-off caused by this filter is easily corrected for, and the only limitation of this filtering technique is that data is not available for output frequencies above 16 times the LO frequency. However, one is usually only interested in output frequencies either much lower than the LO frequency (for down conversion) or near the LO frequency (for up conversion). In either of these two cases of interest, the IF filter adds no appreciable error. For simulations, high-Q IF filters should be avoided, since they give long transient tails that consume large amounts of simulation time.

For verification purposes an emitter-coupled mixer with common-base drive, shown in Figure 4, was designed and fabricated. Transistor Q_1 is chosen to be large in order to minimize its noise contribution. The common base configuration was chosen for the input stage because of its superior linearity. Transistors Q_2 and Q_3 were made somewhat smaller than Q_1 in order to minimize distortion.[x] The mixer was designed to operate at an RF frequency of 1GHz, although it will function for RF frequencies up to 5 GHz. In this circuit configuration, most of the noise is contributed from the non-linear portion of the circuit.

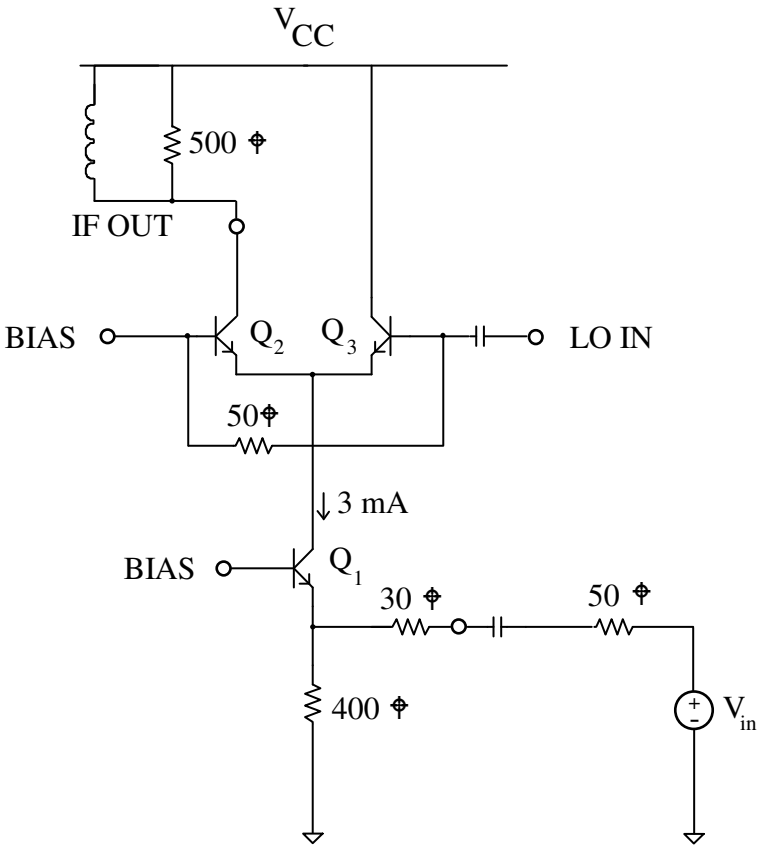

Figure 4 : Schematic of Single-Balanced Mixer Configuration

The approach taken for analyzing the circuit in Figure 4 is to lump all noise sources that inject noise at the emitter of Q_2 and Q_3 into a single equivalent current noise source. This noise includes all of the noise from transistor Q_1 and associated biasing, as well as the noise from the source. Noise sources that are incident at the base of Q_2 are lumped into a single noise source, and likewise for noise sources at the base of Q_3. The noise sources include the 50Ω matching resistor and the noise from the base resistance of Q_2 and Q_3. A bandpass filter is used between the LO and the input port, so it does not contribute significantly to the output noise. Calculation of these noise sources follows the standard linear methods as implemented in SPICE. Care must be taken to consider the actual impedances presented looking out from the LO and RF ports. In addition to the above three noise sources, the shot noise of Q_2 and Q_3 must be considered separately. Because of the low operating currents and LO source impedance, the base shot noise of

transistors Q_2 and Q_3 contributes negligibly. The collector shot noise of transistors Q_2 and Q_3 are analyzed separately. In simulations of shot noise, the initial impulse is scaled by the value of the instantaneous bias current through the device.

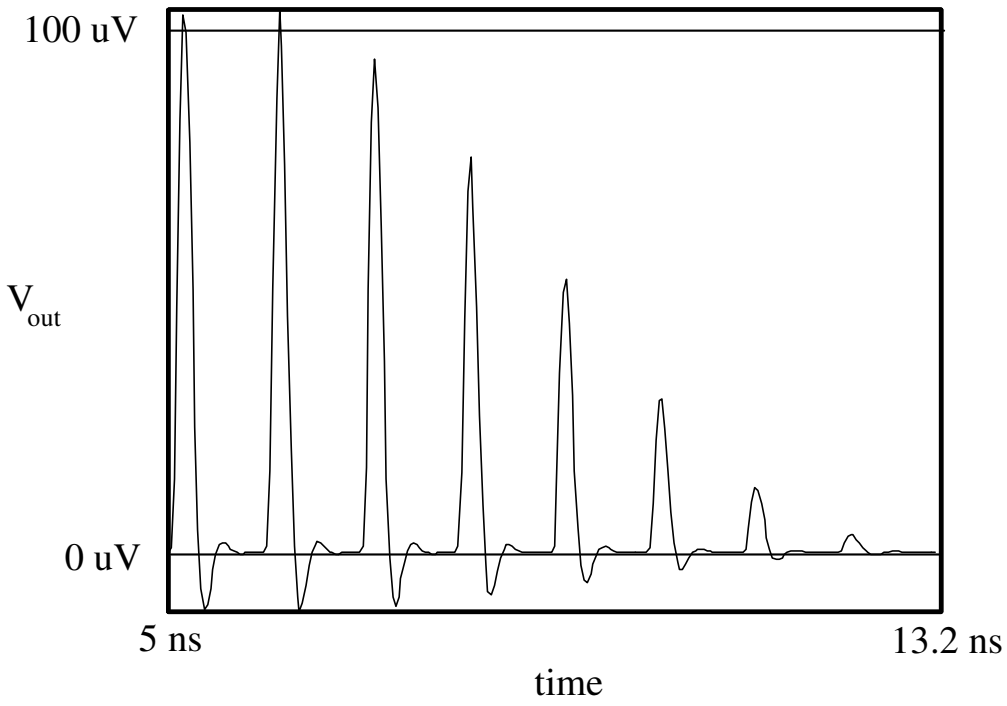

Figure 5: Impulse Response of Single-Balanced Mixer for the RF port (8 of 64 launch phases)

In Figure 5 the impulse response of the mixer to impulses injected at the RF port is depicted for the first 8 of 64 LO phases. The shape of the impulse response is essentially that of the IF filter which is a three-pole maximally flat design. The LO frequency is 1 GHz. Figure 6 depicts the impulse response for all launch phases in a three-dimensional plot. Note that a null exists for a large portion of launch phases. This corresponds to the time when transistor Q_2 is off.

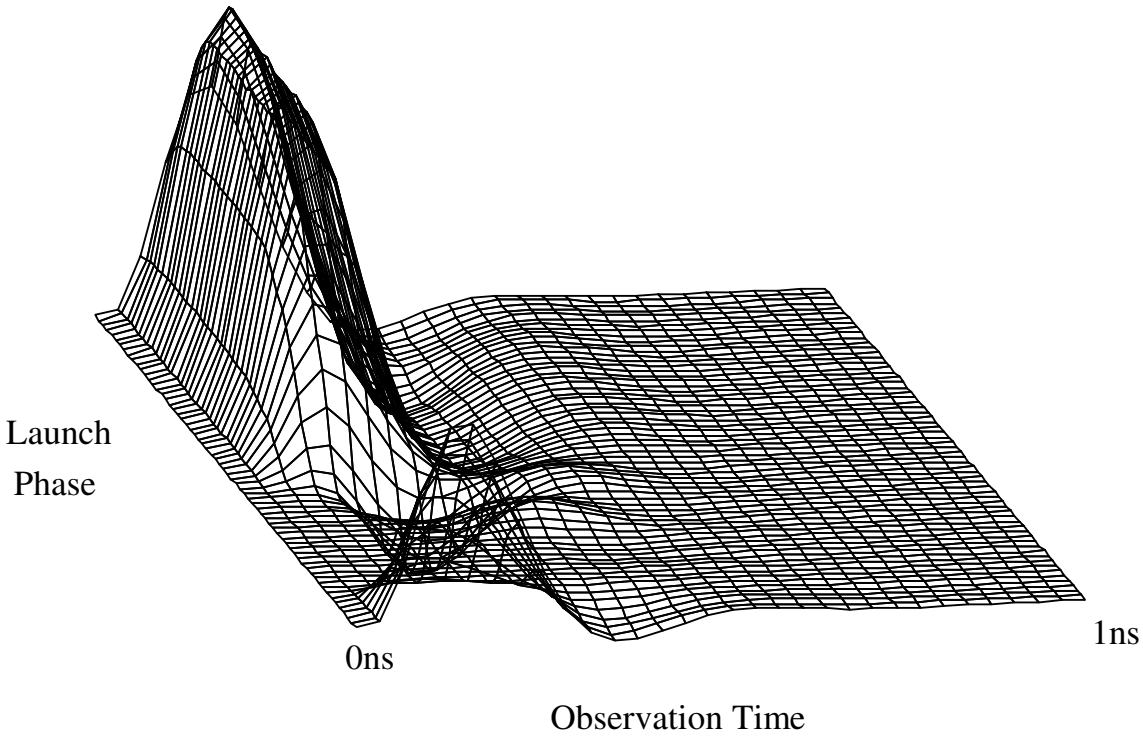

Figure 6: Two Dimensional Impulse Response of a Mixer from RF Port

Figure 7 is the two-dimensional FFT of the impulse response shown in Figure 6. The effect of the three pole low-pass IF filter has been compensated for, so that the intrinsic performance of the mixer at very high IF frequencies may be observed. Recall that the axes are IF output frequency and n, the number of LO harmonics that the input spectrum is shifted by. The plot depicts only positive values of n since it can be easily shown from Equation 8 that the system function has symmetry about the origin. While values of n from 0 to 31 are available, only those from 0 to 15 are plotted, since down conversion from harmonics higher than the 15th is negligible. This suggests that aliasing is not a problem with the chosen point spacing. Note spectral shift by an even number of harmonics of the LO is very weak. This is not surprising since the symmetrical nature of this circuit tends to cancel out even LO harmonics.

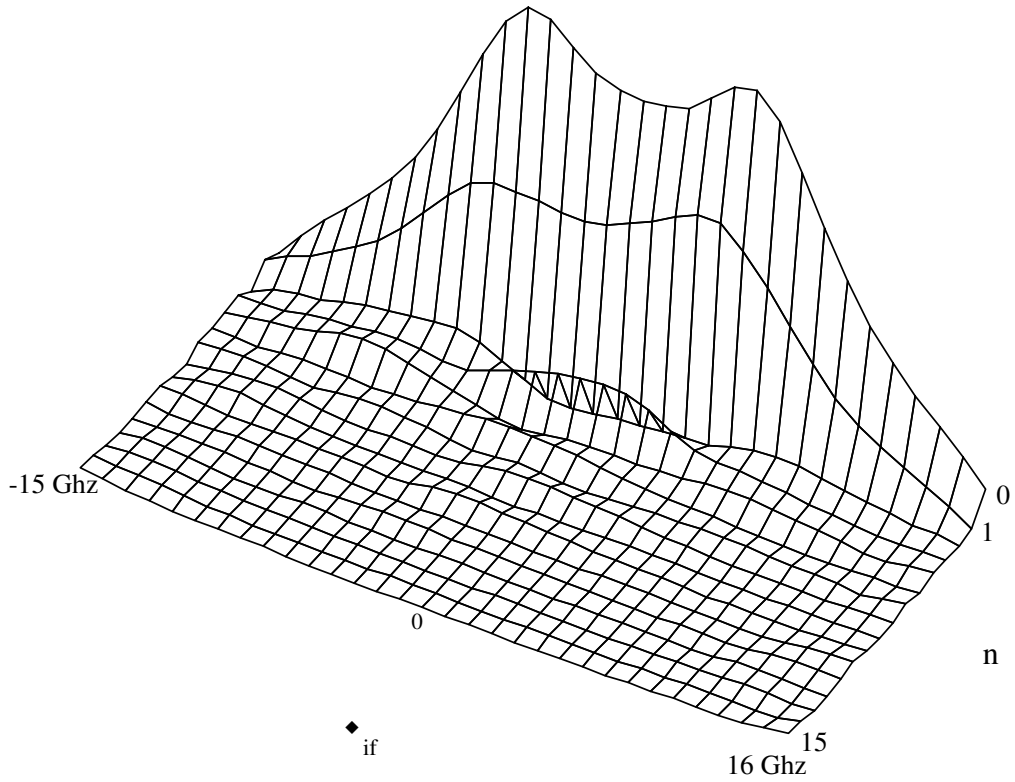

Figure 7: Frequency Response of Mixer from RF Port

Figure 8 contains a cross section of Figure 7, with the IF frequency restricted to be much less than 1 GHz. This is of interest for down-conversion. This particular plot then is of the down-conversion gain vs. input frequency (since for low IF frequencies the input frequency and spectral shift are nearly equal). Again notice the small value of the down-conversion from even harmonics. The value of the down-conversion gain for n=1 corresponds to the signal current conversion gain of the mixer (in this case -10 dB).

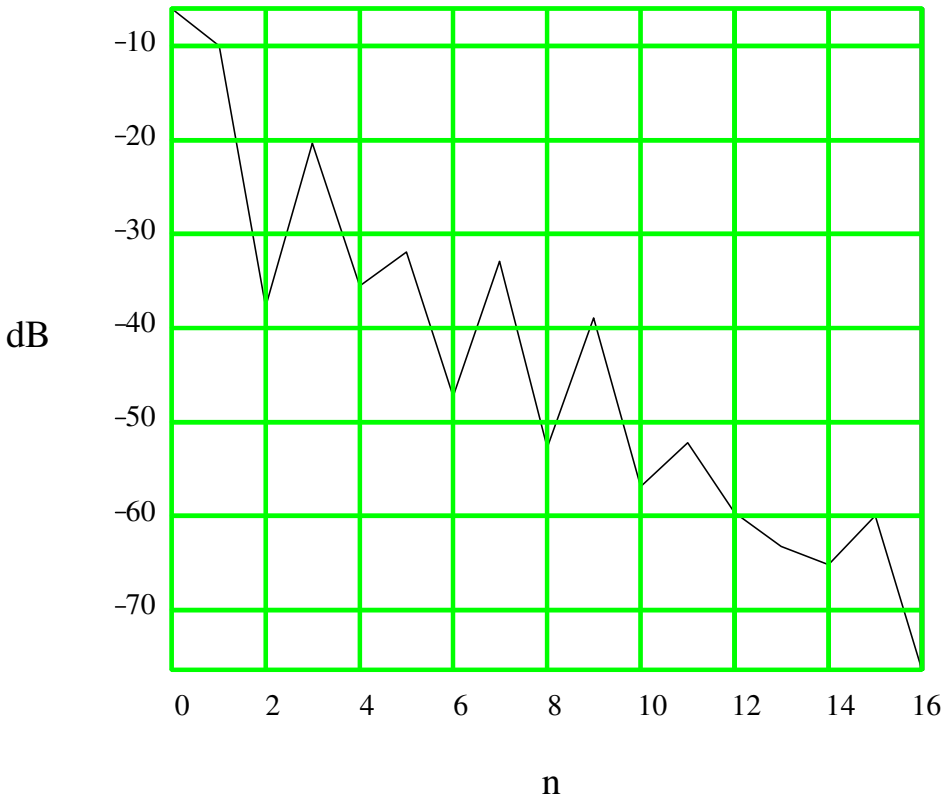

Figure 8: Down Conversion Gain Vs. LO Harmonic from RF Port

I t is clear from Figure 8 that this mixer is not balanced, since it passes signals at the IF frequency to the output. The IF bandwidth of this circuit (in the absence of an IF filter) is close to the f_T of the device (10 GHz) for direct pass through. The IF bandwidth is reduced for larger values of n (the spectral shift). Because of the generally wide IF bandwidth, one can conclude that the noise and signal behavior of this mixer are essentially equivalent for down-conversion from 1 GHz and up-conversion to 1 GHz. However, significant IF bandwidth limitations can occur due to parasitics at the collector of Q_2, making conversion design somewhat more difficult.

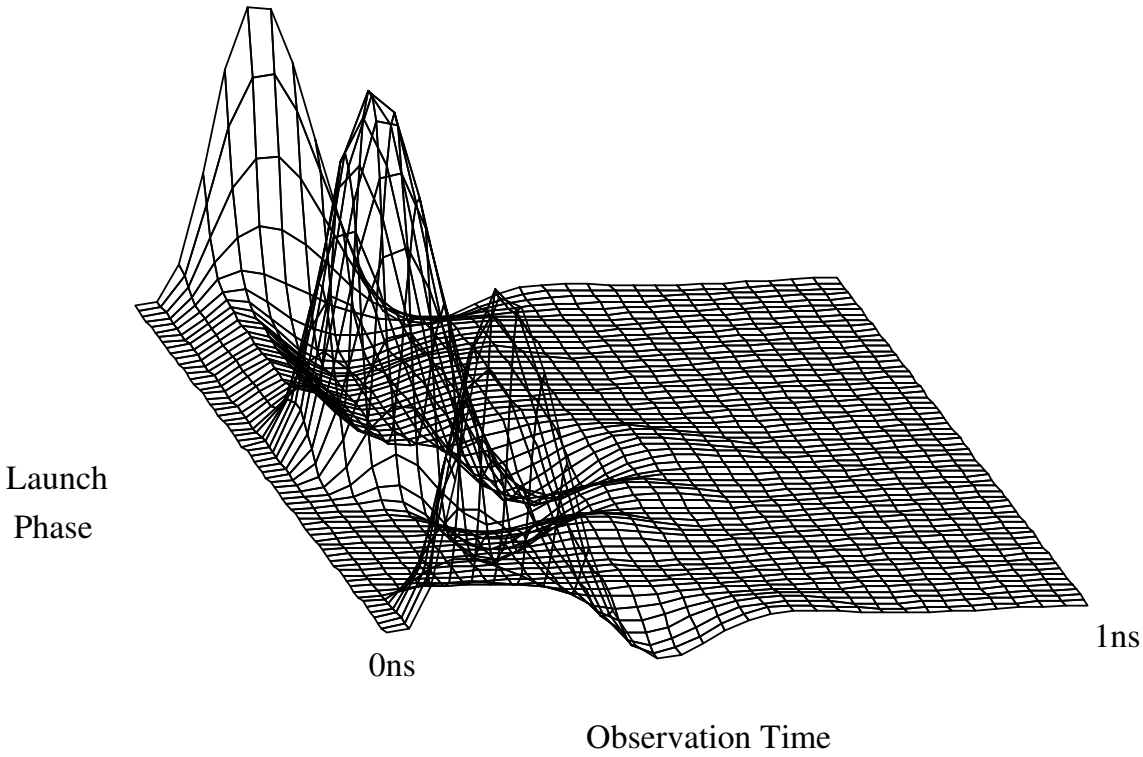

Figure 9: Impulse Response of Mixer from LO Port

Besides noise coming into the RF port, there are noise sources incident at the LO port (such as base-ohmic resistance noise of Q_2 and Q_3). The response to an impulse launched at the LO port is depicted in Figure 9. As with the impulse response from the RF port, the basic shape of the impulse response is due to the three-pole IF filter. Note that the impulse response has large peaks for launch phases near 0 and 180 degrees. These correspond to launch times where both transistors Q_2 and Q_3 are active.

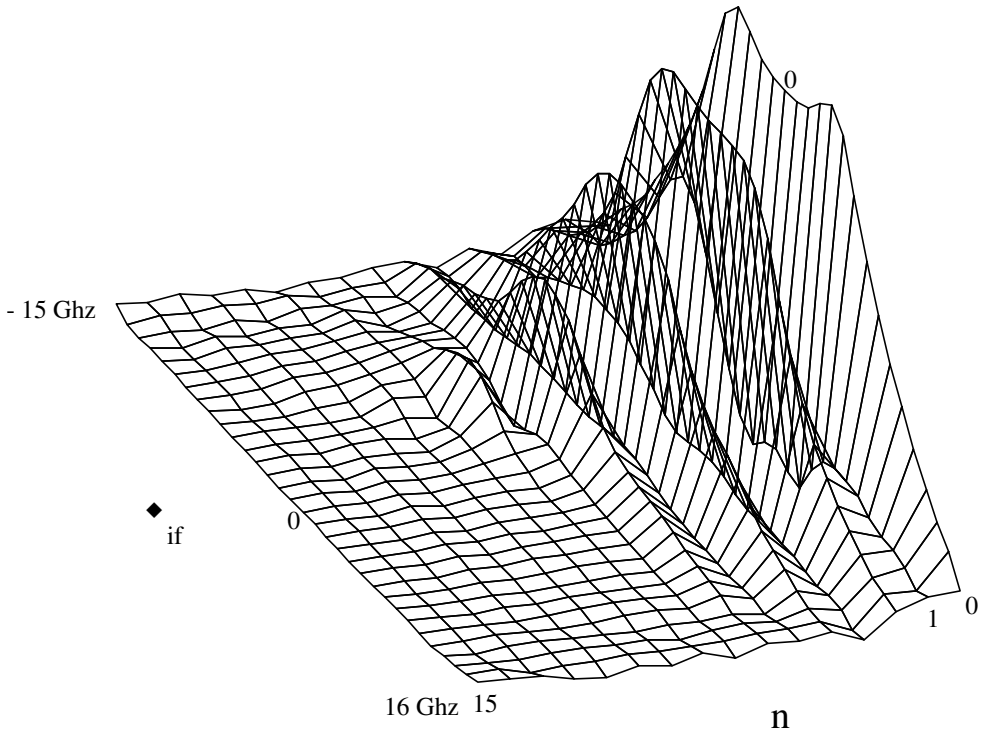

Figure 10: Frequency Response of Mixer from LO Port

Figure 10 is the system function as given in Equation 8, and is the FFT of Figure 9. Notice here the absence of odd LO harmonic spectral shifting (as opposed to the lack of even harmonic shifting for signals injected at the RF port). This is due to the symmetrical nature of the circuit.

Figure 11 depicts the down-conversion gain from the LO port, that is, the value of the system function, $H(\omega_{if}, \omega_{rf})$, for $\omega_{if} << \omega_o$. The plot has been normalized by dividing out the transconductance of the emitter-coupled pair formed by Q_2 and Q_3. Notice that the odd harmonic down-conversion is very weak. In particular, conversion from the first LO harmonic is down more than 50 dB. This is an important feature of the circuit since it implies that noise at the LO port near the LO frequency is reduced in magnitude by 50 dB before passing through to the output. However, due to the single balanced nature of the circuit, noise at the IF frequency does pass through to the output with only about 20 dB of

attenuation. Note that the gain of the emitter-coupled pair must be added to these attenuation factors to get the actual input-output gain.

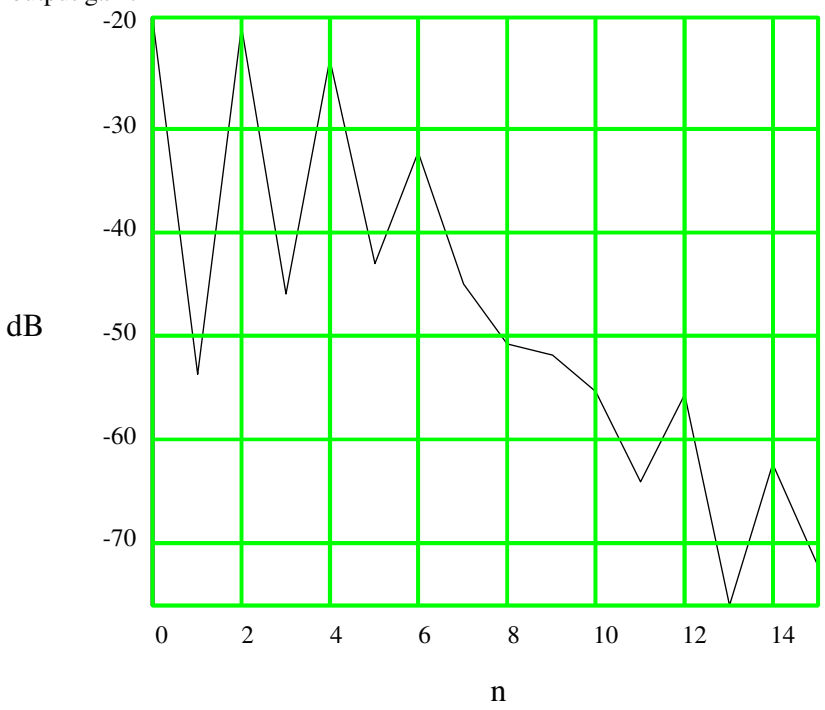

Figure 11: Down Conversion Gain Vs. LO Harmonic from LO port

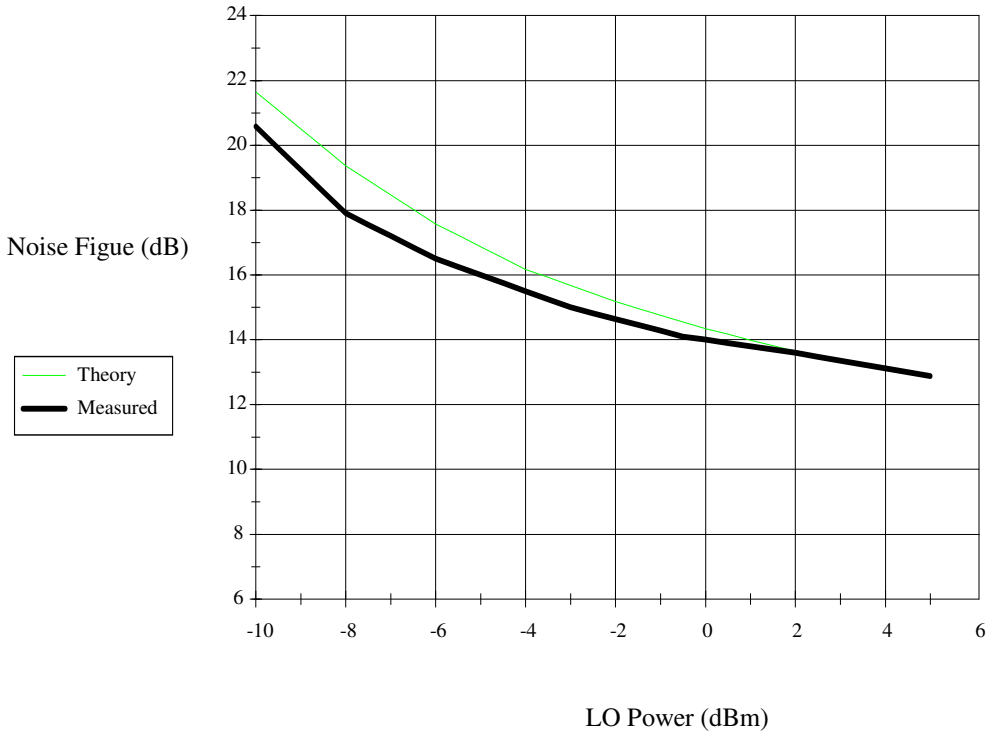

Figure 12: Predicted and Measured Noise Figure vs. LO Power for Mixer

An additional simulation was run for shot noise sources. Special care must be taken with shot noise as is discussed in the next section. Detailed results of shot noise simulations are not presented here.

Figure 12 depicts the predicted and measured noise figure vs. LO power and the two curves are in good agreement.

5.9: Non-Stationary Noise:

Because of the time-varying nature of mixers, the statistics of the output noise are not constant, but vary periodically. Such noise is not strictly stationary, but is *cyclo-stationary.*[xi] Additionally, shot noise, which is modulated by the collector current, is also non-stationary. This lack of stationarity may cause problems in the analysis of mixer noise, since cyclo-stationary noise spectra at frequencies separated by the LO frequency and its harmonics are correlated. Therefore, simple superposition of noise power from different frequencies (as assumed in Equation 10) does not give a correct answer. Fortunately, there are two ways to avoid this problem.

First, there is a theorem that is easily proven. Cyclo-stationary noise that is passed through a filter with bandwidth less than the frequency of the noise statistics becomes stationary. Usually the output noise is passed through an IF filter with bandwidth much narrower than the LO frequency, and hence the output noise is stationary. This is true for both up and down conversion.

Second, cyclo-stationary noise sources such as shot noise may be seen as modulated stationary noise sources. The modulation must then be considered to be part of the mixer system that acts on this noise, and thus must be included as a factor in the impulse response. The impulse response to the hypothetical stationary noise source is given by:

$$g(t,u) = h(t,u) \cdot \sqrt{\frac{I_C(u)}{I_Q}}$$

Where $I_C(u)$ is the large signal collector current of the transistor being considered, and I_Q is the average collector current over time. The input spectral density of the hypothetical stationary noise source is given by:

$$S(\omega) = 2 \cdot q \cdot I_Q$$

5.10: Conclusion

A new technique for predicting noise performance in active mixers has been presented. A single simulation gives information not only on the mixer's noise performance over a wide range of output frequencies but also on the up and down conversion gain. The theory for a numerically efficient and well-conditioned technique was shown. A technique that uses available CAD tools was also presented, and the results of that technique are shown to be accurate for the mixer circuit configuration tested.

Appendix 5A: Derivation of Frequency Domain input/output Relation

Start with the time-domain input output relation:

$$y(t) = \int_{-\infty}^{\infty} h(t,u) \cdot x(u) du \qquad \text{(A1)}$$

and the Fourier Transform relations:

$$x(u) \equiv \frac{1}{2 \cdot \pi} \cdot \int_{-\infty}^{\infty} X(\omega_S) e^{j \cdot \omega_S \cdot u} d\omega_s \qquad \text{(A2)}$$

$$X(\omega_{if}) \equiv \int_{-\infty}^{\infty} x(t) e^{-j \cdot \omega_{if} \cdot t} dt \qquad \text{(A3)}$$

Substituting Equation A1 into Equation A3 yields:

$$Y(\omega_{if}) = \int_{-\infty}^{\infty} \left[\int_{-\infty}^{\infty} h(t,u) \cdot x(u) du \right] e^{-j \cdot \omega_{if} \cdot t} dt \qquad \text{(A4)}$$

Then using Equation A2 gives:

$$Y(\omega_{if}) = \frac{1}{2\pi} \cdot \int_{-\infty}^{\infty} \int_{-\infty}^{\infty} \int_{-\infty}^{\infty} h(t,u) e^{j \cdot \omega_s \cdot u} e^{-j \cdot \omega_{if} \cdot t} X(\omega_s) du dt d\omega_s$$

Let:

$$H(\omega_{if},\omega_s) \equiv \frac{1}{2\pi}\cdot\int_{-\infty}^{\infty}\int_{-\infty}^{\infty} h(t,u)e^{j\cdot\omega_s\cdot u}e^{-j\cdot\omega_{if}\cdot t}\,dudt \qquad \text{(A5)}$$

then it follows that:

$$Y(\omega_{if}) = \int_{-\infty}^{\infty} H(\omega_{if},\omega_s)\cdot X(\omega_s)d\omega_s \qquad \text{(A6)}$$

Appendix 5B: Derivation of input/output Relationships for an LPTV System

Using Formula (A5) from Appendix A with the definition: $g(t,u) \equiv h(t+u,u)$ and $v \equiv t+u$ gives:

$$H(\omega_{if},\omega_s) \equiv \frac{1}{2\pi}\cdot\int_{-\infty}^{\infty}\int_{-\infty}^{\infty} g(v,u)e^{j\cdot(\omega_s-\omega_{if})\cdot u}e^{-j\cdot\omega_{if}\cdot v}\,dudv \qquad \text{(B1)}$$

For an LPTV system, $g(v,u)$ is periodic in the launch time, u. Therefore, g may be expressed as a Fourier Series:

$$g(v,u) = \sum_{n=-\infty}^{\infty} g_n(v)\cdot e^{-j\cdot n\cdot\omega_o\cdot u} \qquad \text{(B2)}$$

where:

$$g_n(v) = \frac{1}{T}\cdot\int_0^T g(v,u)e^{j\cdot n\cdot\omega_o\cdot u}\,du \qquad \text{(B3)}$$

Substituting Equation (B2) into (B1) gives:

$$H(\omega_{if},\omega_s) \equiv \int_{-\infty}^{\infty}\sum_{n=-\infty}^{\infty} g_n(v)\cdot\left[\frac{1}{2\pi}\int_{-\infty}^{\infty} e^{j\cdot(\omega_s-\omega_{if}-n\cdot\omega_o)\cdot u}\,du\right]e^{-j\cdot\omega_{if}\cdot v}\,dv \qquad \text{(B4)}$$

which simplifies to:

$$H(\omega_{if},\omega_s) \equiv \int_{-\infty}^{\infty}\sum_{n=-\infty}^{\infty} g_n(v)\cdot\delta(\omega_s-\omega_{if}-n\cdot\omega_o)e^{-j\cdot\omega_{if}\cdot v}\,dv \qquad \text{(B5)}$$

A new system function for LPTV is defined as:

$$H_n(\omega_{if}) \equiv \int_{-\infty}^{\infty} g_n(v)e^{-j\cdot\omega_{if}\cdot v}\,dv \qquad \text{(B6)}$$

Then $$H(\omega_{if},\omega_s) \equiv \sum_{n=-\infty}^{\infty} H_n(\omega_{if}) \cdot \delta(\omega_s - \omega_{if} - n \cdot \omega_o)$$

and then using Equation A6, the output spectrum is:

$$Y(\omega_{if}) = \sum_{n=-\infty}^{\infty} \int_{-\infty}^{\infty} H_n(\omega_{if}) \cdot \delta(\omega_s - \omega_{if} - n \cdot \omega_o) \cdot X(\omega_s) d\omega_s$$

This simplifies to:

$$Y(\omega_{if}) = \sum_{n=-\infty}^{\infty} H_n(\omega_{if}) \cdot X(\omega_{if} + n \cdot \omega_o)$$

combining Equations B3 and B7 gives:

$$H_n(\omega_{if}) = \int_{-\infty}^{\infty} \left[\frac{1}{T} \cdot \int_0^T g(v,u) e^{j \cdot n \cdot \omega_o \cdot u} du \right] e^{-j \cdot \omega_{if} \cdot v} dv$$

Chapter 6: Large-Signal Behavior in Emitter Coupled Pair Mixers

As seen in Chapter 2, the emitter-coupled pair mixer is used to form a current switching mixer. Drivers that convert voltage-to-current are discussed in Chapter 4. In this chapter, the large-signal behavior of the current switching portion of the mixer is analyzed. Since this circuit performs a highly non-linear function, a closed form solution is not possible. However essential relationships can be derived through a combination of analysis and simulation.

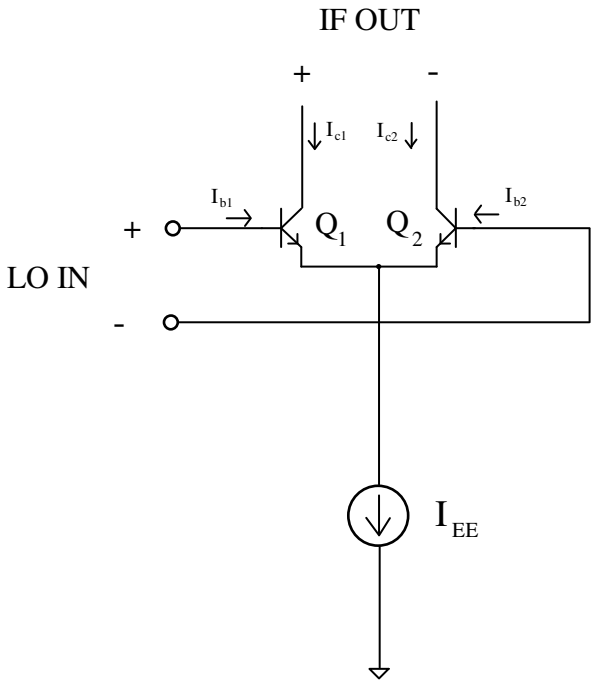

Figure 1: Emitter-Coupled Pair Mixer

The analysis of the emitter coupled pair begins by assuming that the dc component of the base currents may be neglected. In that case, the base currents are given by:

$$I_{b1} = (C_{b1} + C_{je}) \cdot \frac{dV_{be1}}{dt} = \tau_f \cdot \frac{dI_{c1}}{dt} + C_{je} \cdot \frac{dV_{be1}}{dt} \qquad (1a)$$

$$I_{b2} = (C_{b2} + C_{je}) \cdot \frac{dV_{be2}}{dt} = \tau_f \cdot \frac{dI_{c2}}{dt} + C_{je} \cdot \frac{dV_{be2}}{dt} \qquad (1b)$$

where V_{be} is the internal base-emitter voltage. The internal base-emitter voltage does not include the portion of the base-emitter voltage drop due to parasitic emitter and base resistances. The total base-emitter voltage (including the drop across r_b and r_e) is referred to as the external or extrinsic base-emitter voltage.

The collector currents are given by:

$$I_{c1} = I_s \cdot e^{V_{be1}/V_T} \qquad (2a)$$

$$I_{c2} = I_s \cdot e^{V_{be2}/V_T} \qquad (2b)$$

Equations (1) and (2) may be combined to give a more convenient expression for the base currents since:

$$\frac{dV_{be}}{dt} = \frac{V_T}{I_c} \cdot \frac{dI_c}{dt}$$

Therefore:

$$I_{b1} = \left[\tau_f + \frac{C_{je} \cdot V_T}{I_{c1}} \right] \cdot \frac{dI_{c1}}{dt} \qquad (3a)$$

$$I_{b2} = \left[\tau_f + \frac{C_{je} \cdot V_T}{I_{c2}} \right] \cdot \frac{dI_{c2}}{dt} \qquad (3b)$$

Now KCL gives:

$$I_{b1} + I_{b2} = I_{EE} - I_{c1} - I_{c2} \qquad (4)$$

KVL gives

$$V_{LO}(t) - I_{b1} \cdot r_b - V_T \cdot \ln\left[\frac{I_{c1}}{I_s}\right] + V_T \cdot \ln\left[\frac{I_{c2}}{I_s}\right] + I_{b2} \cdot r_b = 0 \qquad (5)$$

combining Equation 4 and 5 gives:

$$I_{b1} = \frac{1}{2} \cdot \left[I_{EE} - I_{c1} - I_{c2} + \frac{V_{LO}(t) + V_T \cdot \ln(\frac{I_{c2}}{I_{c1}})}{r_b} \right] \qquad (6a)$$

$$I_{b2} = \frac{1}{2} \cdot \left[I_{EE} - I_{c1} - I_{c2} - \frac{V_{LO}(t) + V_T \cdot \ln(\frac{I_{c2}}{I_{c1}})}{r_b} \right] \qquad (6b)$$

Now combining Equation 3 and 6 yields the state equations:

$$\frac{dI_{c1}}{dt} = \frac{1}{2} \cdot \frac{I_{EE} - I_{c1} - I_{c2} + \frac{V_{LO}(t) + V_T \cdot \ln(\frac{I_{c2}}{I_{c1}})}{r_b}}{\tau_f + \frac{C_{je} \cdot V_T}{I_{c1}}} \qquad (7a)$$

$$\frac{dI_{c2}}{dt} = \frac{1}{2} \cdot \frac{I_{EE} - I_{c1} - I_{c2} - \left[\frac{V_{LO}(t) + V_T \cdot \ln(\frac{I_{c2}}{I_{c1}})}{r_b} \right]}{\tau_f + \frac{C_{je} \cdot V_T}{I_{c2}}} \qquad (7b)$$

The following normalization helps simplify Equations 7a,b:

$$t' = \omega_o \cdot t$$

$$I_{EE} = I_Q + i_s$$

$$i_s' = \frac{i_s}{I_Q}$$

$$I_c' = \frac{I_c}{I_Q}$$

$$b = \frac{V_{LOA}}{V_T}$$

$$V_{LO}(t) = V_{LOA} \cdot \sin(\omega_o \cdot t) = b \cdot V_T \cdot \sin(t')$$

$$i_s = i_{sa} \cdot \sin(\omega_{rf} \cdot t)$$

Then:

$$\frac{dI_{c1}'}{dt'} = \frac{1}{2} \cdot \left[\frac{1 + i_s' - I_{c1}' - I_{c2}'}{\omega_o \cdot \tau_f + \frac{\omega_o C_{je} \cdot V_T}{I_Q} \frac{1}{I_{c1}'}} + \frac{b \cdot \sin(t') + \ln(\frac{I_{c2}'}{I_{c1}'})}{\frac{I_Q \cdot r_b}{V_T} \cdot \left[\omega_o \cdot \tau_f + \frac{\omega_o C_{je} \cdot V_T}{I_Q} \frac{1}{I_{c1}'} \right]} \right] \qquad (8a)$$

$$\frac{dI_{c2}'}{dt'} = \frac{1}{2} \cdot \left[\frac{1 + i_s' - I_{c1}' - I_{c2}'}{\omega_o \cdot \tau_f + \frac{\omega_o C_{je} \cdot V_T}{I_Q} \frac{1}{I_{c2}'}} - \frac{b \cdot \sin(t') + \ln(\frac{I_{c2}'}{I_{c1}'})}{\frac{I_Q \cdot r_b}{V_T} \cdot \left[\omega_o \cdot \tau_f + \frac{\omega_o C_{je} \cdot V_T}{I_Q} \frac{1}{I_{c2}'} \right]} \right] \quad (8b)$$

While Equations 8a&b cannot be solved analytically, the solution depends on a few normalized parameters.[xii] The solution for the collector current is of the form:

$$I_{c1,2}(t) = f_{1,2}(\omega_o \cdot \tau_f, \frac{I_{EE} \cdot r_b}{V_T}, \frac{\omega_o C_{je} \cdot V_T}{I_{EE}}, \frac{V_{LOA}}{V_T}, \frac{i_s}{I_Q}) \quad (9)$$

In order to understand the large-signal behavior of the emitter-coupled pair mixer, it is easiest to first consider a few special cases. First the low frequency behavior is analyzed. Then the behavior is analyzed at high frequencies with either low current density (where large devices are used and parasitic resistances are negligible) or high current density (where parasitic capacitances are swamped by C_b).

6.1: Behavior of Mixer at Low Frequencies

If charge storage effects are neglected, then a closed form solution is obtainable. The differential equations given by 8a&b reduce to the algebraic equations:

$$I_{c1} - I_{c2} = I_{EE} \cdot \tanh\left[\frac{V_{LO}}{2 \cdot V_T} \right] \quad (10)$$

$$I_{c1} + I_{c2} = I_{EE}$$

6.2:Conversion Gain at Low Frequencies

Conversion gain is defined as the ratio of the output signal's amplitude at the IF frequency to the input signal's amplitude at the RF frequency. As is shown in Chapter 5:

$$a_{ic} \equiv \frac{Y(\omega_{if})}{X(\omega_{rf})} = H_{\pm 1}(\omega_{if})$$

Assuming that $V_{LO}(t) = V_{LOA} \cdot \sin(\omega_o \cdot t) = b \cdot V_T \cdot \sin(t')$ and $i_s = i_{sa} \cdot \sin(\omega_{rf} \cdot t)$, the differential collector current is given by:

$$I_{cd} \equiv I_{c1} - I_{c2} = \left[I_Q + i_{sa} \cdot \sin(\omega_{rf} \cdot t)\right] \cdot \tanh\left[\frac{V_{LOA}}{2 \cdot V_T} \cdot \sin(\omega_o \cdot t)\right]$$

Recalling Equation 18 from Chapter 5,

$$H_n = \frac{1}{T_o} \cdot \int_0^{T_o} h(t) e^{j \cdot n \cdot \omega_o \cdot t} dt$$

here:

$$h(t) = \tanh\left[\frac{V_{LOA}}{2 \cdot V_T} \cdot \sin(\omega_o \cdot t)\right]$$

The conversion gain is then:

$$a_{ic} = \left|H_1(\omega_{if})\right| = \left|\frac{1}{T_o} \cdot \int_0^{T_o} \tanh\left[\frac{V_{LOA}}{2 \cdot V_T} \cdot \sin(\omega_o \cdot t)\right] e^{j \cdot \omega_o \cdot t} dt\right|$$

This conversion gain is independent of the LO frequency, and can be simplified to:

$$a_{ic}(b) = \left|H_1(\omega_{if})\right| = \frac{1}{2 \cdot \pi} \cdot \int_0^{\pi} \tanh\left[\frac{b}{2} \cdot \sin(t)\right] \cdot \sin(t) dt \quad (11)$$

where:

$$b \equiv \frac{V_{LOA}}{V_T}$$

The conversion gain vs. LO power is plotted in Figure 2. The X-axis is LO power into a 50 ohm load (a power level of 0 dBm into a 50 ohm load corresponds to 316mV peak amplitude). Notice that for LO powers greater than -5 dBm (about 178mV amplitude) the conversion gain is nearly constant at about -4

dB. The conversion gain is limited to the theoretical 3.93dB loss of an ideal switch. As the LO power drops below -10dBm (100mV), the conversion gain drops drastically.

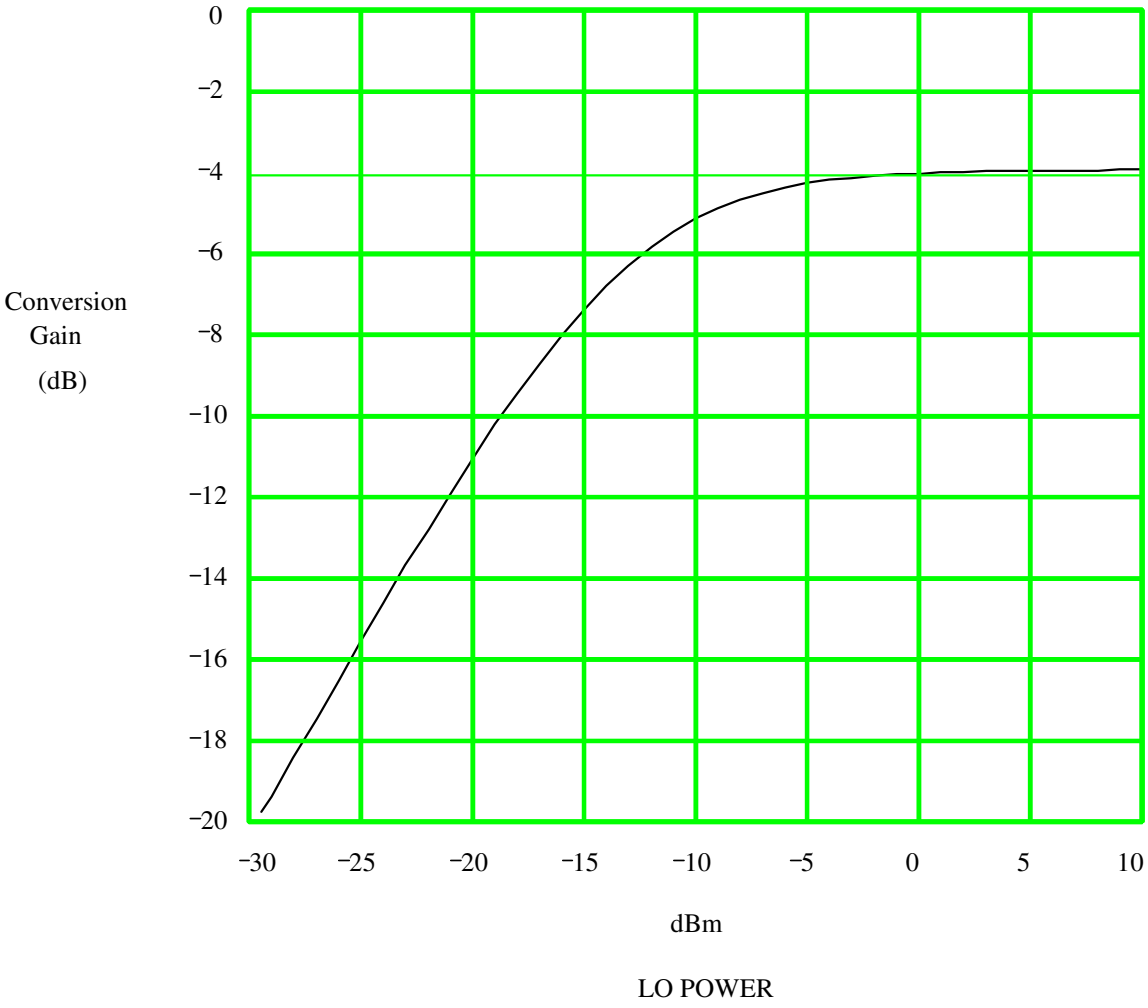

Figure 2: Conversion Gain vs. LO power for the ECP mixer

6.3: Behavior for high current density

First, consider the case where $\frac{\omega_o C_{je} \cdot V_T}{I_{EE}} << 1$. This situation occurs when a device is run at a high current density (near its peak f_T) or low frequencies. The state equations simplify to:

$$\frac{dI_{c1,2}'}{dt'} = \frac{1}{2} \cdot \left[\frac{1 + i_s' - I_{c1}' - I_{c2}'}{\omega_o \cdot \tau_f} \pm \frac{b \cdot \sin(t') + \ln(\frac{I_{c2}'}{I_{c1}'})}{\omega_o \cdot \tau_f \cdot \frac{r_b \cdot I_Q}{V_T}} \right] \quad (12)$$

The equations may be separated into differential and common mode equations (as is commonly done for the analysis of the ECP amplifier). The common mode and differential mode quantities are defined as:

$$I_{cc}' \equiv \frac{1}{2}(I_{c1}' + I_{c2}')$$

$$I_{cd}' \equiv I_{c1}' - I_{c2}'$$

Then the state equations in terms of these new variables are given by:

$$\frac{dI_{cc}'}{dt'} = \frac{1 + i_s' - 2 \cdot I_{cc}'}{2 \cdot \omega_o \cdot \tau_f} \quad (13a)$$

$$\frac{dI_{cd}'}{dt'} = \frac{b \cdot \sin(t') + 2 \cdot \tanh^{-1}(\frac{I_{cd}'}{2 \cdot I_{cc}'})}{\omega_o \cdot \tau_f \cdot \frac{r_b \cdot I_Q}{V_T}} \quad (13b)$$

Equation 13a is linear, and is easily solvable with standard ODE techniques. If

$$i_s(t) = i_{sa} \cdot \sin(\omega_s \cdot t)$$

$$I_{cc}(t) = \frac{I_{EE}}{2} \cdot \left[1 + \frac{i_{sa}}{I_Q} \frac{\sin(\omega_s \cdot t + \phi)}{\sqrt{1 + (\omega_s \cdot \tau_f)^2}} \right] \quad (14)$$

where:

$$\phi = \tan^{-1}(\omega_s \cdot \tau)$$

The common mode response has a single pole at $\omega = \frac{1}{\tau_f} = \omega_T$. Thus we can conclude that the bandwidth of an ECP mixer does not exceed the f_T of the devices.

From Equation 13b, the solutions for the differential mode current is of the form:

$$I_{cd}(t') = g(\omega_o \tau_f \cdot \frac{r_b \cdot I_Q}{V_T}, \frac{V_{LOA}}{V_T}, \omega_o \tau_f, \frac{i_{sa}}{I_q}) \qquad (15)$$

Although the parameter $\omega_o \tau_f$ is not explicitly seen in Equation 13b, there is a dependency on this parameter since the solution of Equation 13b depends on $I_{cc}'(t)$. The Equation for $I_{cc}'(t)$ then has explicit dependence on $\omega_o \tau_f$.

Usually $i_{sa} << I_Q$ and then $I_{cc}(t) \approx \frac{I_Q}{2}$ and the state of the mixer is then determined by only two parameters:

$$\frac{\omega_o \tau_f \cdot r_b \cdot I_Q}{V_T} = \omega_o \cdot r_b \cdot C_b$$

and $$\frac{V_{LOA}}{V_T}$$

Simulations indicate that the characteristic shape of the collector current vs. time depends primarily on the ratio of the two parameters:

$$\frac{\omega_o \tau_f \cdot r_b \cdot I_Q}{V_{LOA}}$$

This parameter can be written:

$$\frac{I_Q}{V_{LOA} / r_b} \cdot \omega_o \tau_f$$

The first of these two factors is inversely related to the amount of current flowing into the base of the transistors. The second parameter is related to the fraction of an LO cycle that the carriers spend traversing the base. The ratio of these two factors determines the speed of the switch relative to an LO period.

The behavior of the mixer at high current densities is primarily determined by this single parameter. When $\omega_o \tau_f \cdot r_b \cdot I_Q / V_{LOA} << 1$ the collector current waveform is essentially the same as it is in the absence of charge storage. That is:

$$I_{cd}(t) \approx I_Q \cdot \tanh\left[\frac{V_{LOA} \cdot \sin(t)}{2 \cdot V_T}\right]$$

As $\omega_o \tau_f \cdot r_b \cdot I_Q / V_{LOA}$ approaches unity, the collector current waveform changes. Figures 3a,b,c depict the collector current waveform vs. time for $\omega_o \tau_f \cdot r_b \cdot I_Q / V_{LOA} = 0.125, 0.5, 1$. For each of these curves, $V_{LOA} = 500mV$. The current waveform in Figure 3a is very similar to the waveform at low frequencies. The transition time between maximum current and zero current has been lengthened slightly. The collector current approximates a square wave. In Figure 3b, the transition time has been lengthened substantially, though there is still a "flat top" to the current waveform. In Figure 3c, the collector current is nearly sinusoidal. The circuit no longer "squares up" the LO. Thus, significant changes in the behavior of the circuit can be expected as $\omega_o \tau_f \cdot r_b \cdot I_Q / V_{LOA}$ approaches unity.

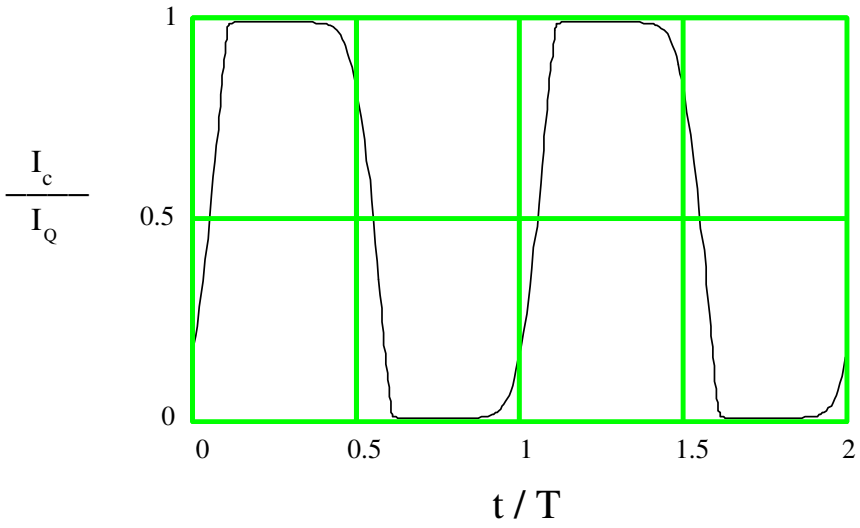

Figure 3a: Collector Current vs. Time for $\omega_o \tau_f \cdot r_b \cdot I_Q / V_{LOA} = 0.125$

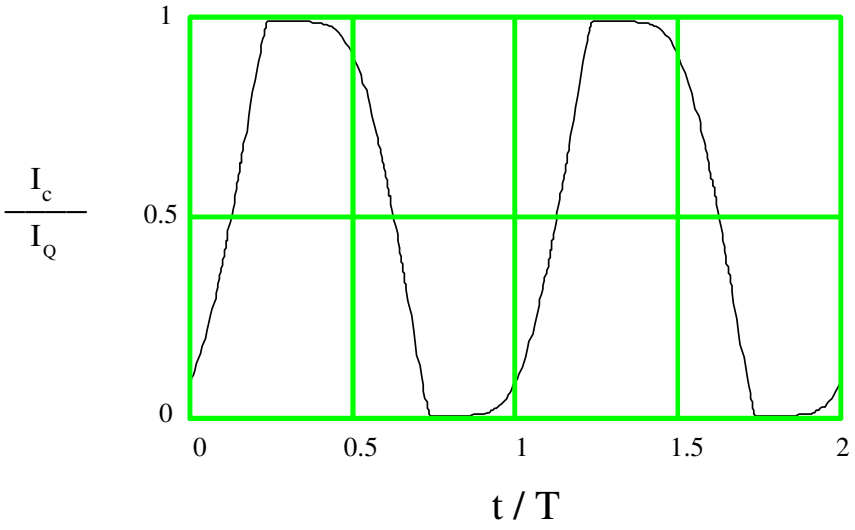

Figure 3b: Collector Current vs. Time for $\omega_o \tau_f \cdot r_b \cdot I_Q / V_{LOA} = 0.5$

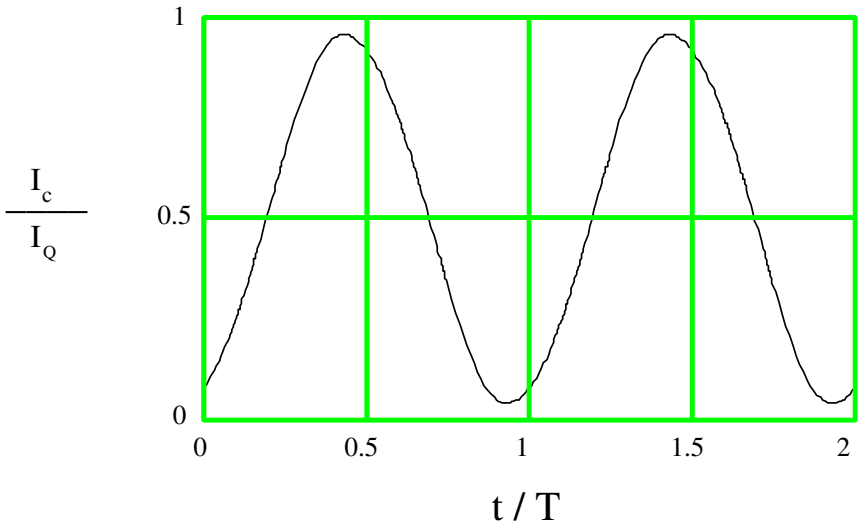

Figure 3c: Collector Current vs. Time for $\omega_o \tau_f \cdot r_b \cdot I_Q / V_{LOA} = 1$

The behavior of the emitter-coupled pair mixer when operated at high current densities is primarily governed by the transition time. The transition time is controlled by two parameters: $\omega_o \tau_f \cdot r_b \cdot I_Q / V_T$ and V_{LOA} / V_T. The transition time increases with the first parameter and decreases with the second. When the ratio of the two is held constant, the transition time is constant. That is, the transition time is primarily dependent on $\omega_o \tau_f \cdot r_b \cdot I_Q / V_{LOA}$. As $\omega_o \tau_f \cdot r_b \cdot I_Q / V_{LOA}$ approaches unity, the transition time

becomes a significant fraction of a half-cycle. For $\omega_o \tau_f \cdot r_b \cdot I_Q / V_{LOA} = 1$, the transition time exceeds a half-cycle, and the collector current waveform appears sinusoidal. This represents a significant change in behavior of the mixer since both of the devices remain active at all times when $\omega_o \tau_f \cdot r_b \cdot I_Q / V_{LOA} > 1$ whereas each device is off for at least some fraction of a period when $\omega_o \tau_f \cdot r_b \cdot I_Q / V_{LOA} < 1$. Having both devices active at all times has significant implications for conversion gain and noise performance.

6.4: Conversion Gain for High Current Density:

Figure 4 shows the conversion gain vs. $\omega_o \cdot \tau_f \cdot r_b \cdot I_Q / V_{LOA}$ for $V_{LOA} = 100\text{mV}, 178\text{mV}, 1\text{V}$ and $C_{je} = 0$. These values correspond to LO powers of -10dBm,-5dBm and +10dBm into 50 ohms, at room temperature. At high current densities, the conversion gain increases monotonically for increasing LO power (until a device saturates).

The conversion gain remains close to its low frequency value until $\omega_o \cdot \tau_f \cdot r_b \cdot I_Q / V_{LOA} \approx 1$.

Thus the RF bandwidth is limited to:

$$\omega_o \cdot \approx \frac{1}{\tau_f} \cdot \frac{V_{LOA}}{r_b \cdot I_Q} = \omega_T \cdot \frac{V_{LOA}}{r_b \cdot I_Q}$$

Recall that the bandwidth is also limited to ω_T because of the common-mode response (See Equation 13b). Thus, r_b will not limit the bandwidth so long as:

$$V_{LOA} > r_b \cdot I_Q$$

Hence, there is a minimum LO power necessary to drive the mixer at high frequencies without degradation of conversion gain.

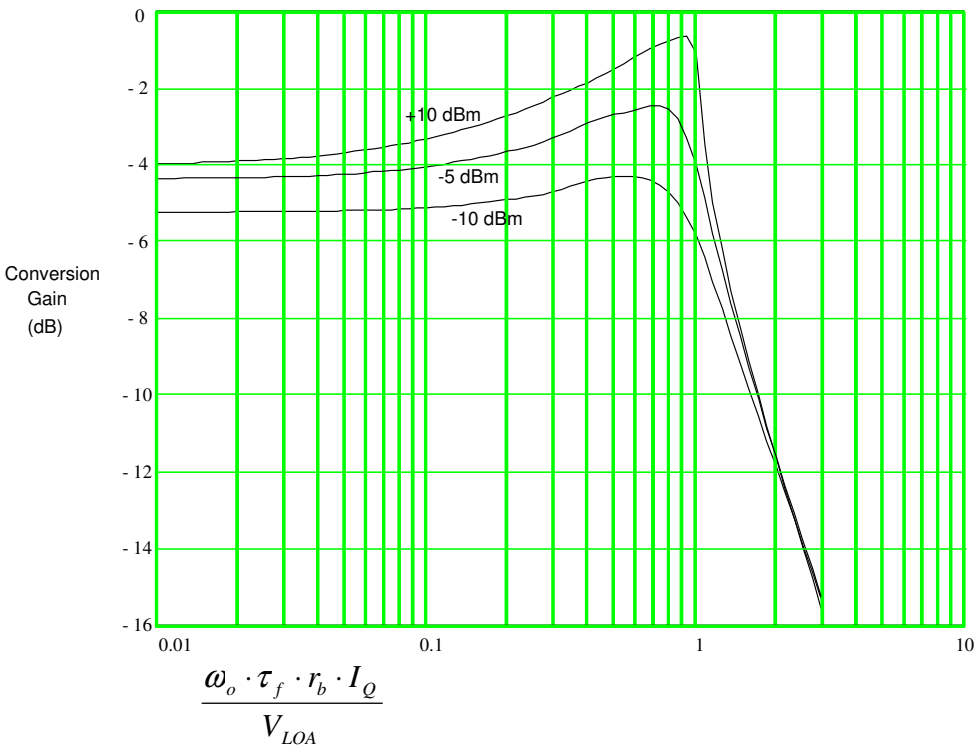

Figure 4: Conversion Gain vs. $\omega_o \cdot \tau_f \cdot r_b \cdot I_Q / V_{LOA}, C_{je} = 0$

The analysis at high current densities is limited by the fact that τ_f is assumed constant. At current densities beyond that which gives the maximum f_T for the device, the analysis is not accurate.

6.5: Behavior for Low Current Density

Now consider the case where $\omega_o \cdot \tau_f \cdot r_b \cdot I_Q / V_{LOA} << 1$ but $\frac{\omega_o C_{je} \cdot V_T}{I_Q} \to 1$. This occurs when a large device is operated at a low current density. Since r_b is negligible under this assumption, the base-emitter capacitors now form a ring with the LO source. Thus, the number of state equations is reduced from two to one. The state equation is:

$$\frac{dI_{c1}'}{dt'} = \frac{1 + i_s' - I_{c1}' \cdot \left[1 + e^{-b \cdot \sin(t')}\right]}{2 \cdot \left[\omega_o \cdot \tau_f + \frac{\omega_o \cdot C_{je} \cdot V_T}{I_Q} \cdot \frac{1}{I_{c1}'}\right]} \qquad (16)$$

$$I_{c2}' = I_{c1}' \cdot e^{-b \cdot \sin(t')}$$

The solution is of the form:

$$I_{c1,2}(t') = g(\frac{\omega_o \cdot C_{je} \cdot V_T}{I_Q}, \frac{V_{LOA}}{V_T}, \omega_o \tau_f, \frac{i_s}{I_Q}) \qquad (17)$$

Simulations show that the dependency on $\omega_o \tau_f$ is minimal so long as $\omega_o \tau_f << 1$. Also if $i_s << I_Q$ then the collector current waveform is only perturbed slightly by i_s. Thus the behavior of the circuit is determined primarily by two parameters:

$$\omega_o \cdot C_{je} \cdot V_T / I_Q = \omega_o \cdot C_{je} \cdot \frac{1}{"g_m"}$$

and V_{LOA} / V_T.

As with the high current density case, the basic behavior of the collector current is governed by the product of these parameters: $\omega_o \cdot C_{je} \cdot V_{LOA} / I_Q$ Figure 5a,b,c depict the normalized collector current waveform for $\omega_o \cdot C_{je} \cdot V_{LOA} / I_Q = 0.125, 0.5, 1$.

In Figure 5a, note that the normally square top of the current waveform has been tilted downward. This is due to the charging and discharging of the C_{je} of the **off** device. Since C_{je} is roughly constant, $I_{cje} \approx C_{je} \cdot dV_{be} / dt$. The base-emitter voltage of the "on" device does not vary substantially. Therefore almost all of the LO variation is seen across the base-emitter of the **off** device.

Thus :

$$I_{b-off} \approx C_{je} \cdot dV_{LO} / dt = -\omega_o \cdot C_{je} \cdot V_{LOA} \cdot \cos(\omega_o \cdot t)$$

$$I_{c-on} \approx I_Q \left[1 + \frac{\omega_o \cdot C_{je} \cdot V_{LOA}}{I_Q} \cdot \cos(\omega_o \cdot t) \right] \qquad (18)$$

As $\omega_o \cdot C_{je} \cdot V_{LOA} / I_Q$ is increased to 0.5 (Figure 5b), the tilt becomes more dramatic. At $\omega_o \cdot C_{je} \cdot V_{LOA} / I_Q = 1$ (Figure 5c) the tilt becomes sufficiently large that the "on" device nearly shuts off before the half-cycle of the LO is complete. This is a significant transition point in the large-signal behavior of the ECP mixer. Operation of the ECP mixer beyond $\omega_o \cdot C_{je} \cdot V_{LOA} / I_Q = 1$ leads to very large base charging currents (in excess of I_Q).

Note that the transition time is not substantially affected by C_{je} for reasonably small values of

C_{je}. This is logical, since during transition time the active base charging capacitance, C_b, tends to dominate.

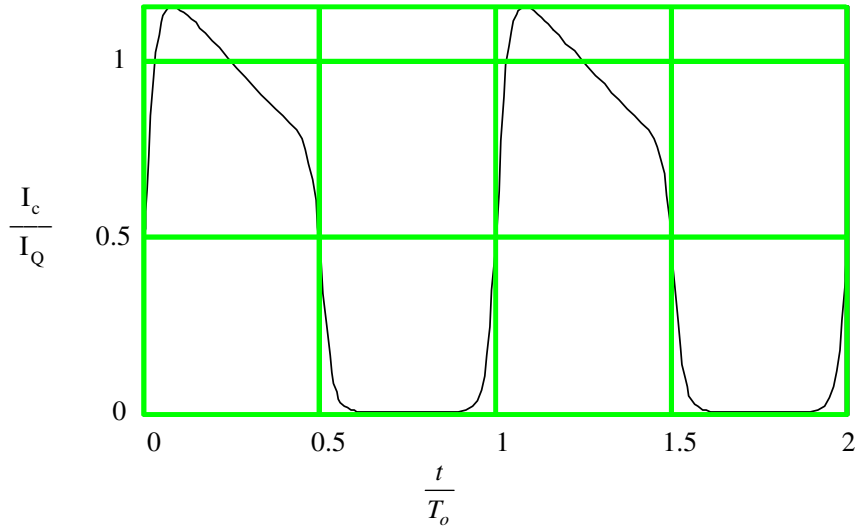

Figure 5a: $I_c(t) vs.time$ for $\omega_o \cdot C_{je} \cdot V_{LOA} / I_Q = 0.125$

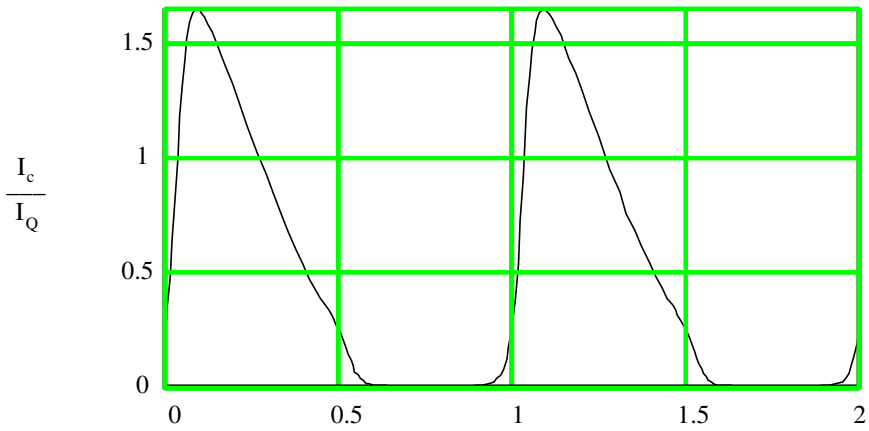

Figure 5b: $I_c(t)$ *vs .time* for $\omega_o \cdot C_{je} \cdot V_{LOA} / I_Q = 0.5$

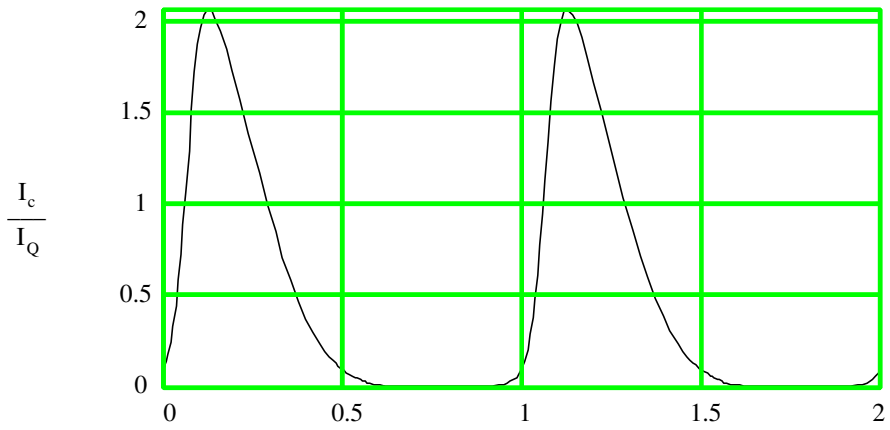

Figure 5c $I_c(t)$ *vs .time* for $\omega_o \cdot C_{je} \cdot V_{LOA} / I_Q = 1$

6.6: Conversion Gain for Low Current Density:

In Figure 6, the conversion gain is plotted vs. $\omega_o \cdot C_{je} \cdot V_T / I_Q$ for $V_{LOA} = 100\text{mV}, 178\text{mV}, 1\text{V}$ and $r_b = \tau_f = 0$. These LO voltages correspond to powers of -10dBm,-5dBm and +10dBm into 50 ohms. For all LO powers, the conversion gain is reasonably independent of frequency until $\omega_o \cdot C_{je} \cdot V_T / I_Q$ =0.5. This corresponds to $\omega = \omega_T / 2$. This is similar to the bandwidth limit of ω_T for the high current density situation. The factor of two is due to the parasitic C_{je} of the off device, which adds to C_{je} of the active device. The conversion gain is generally increasing for increasing LO power; however, this is not universally true.

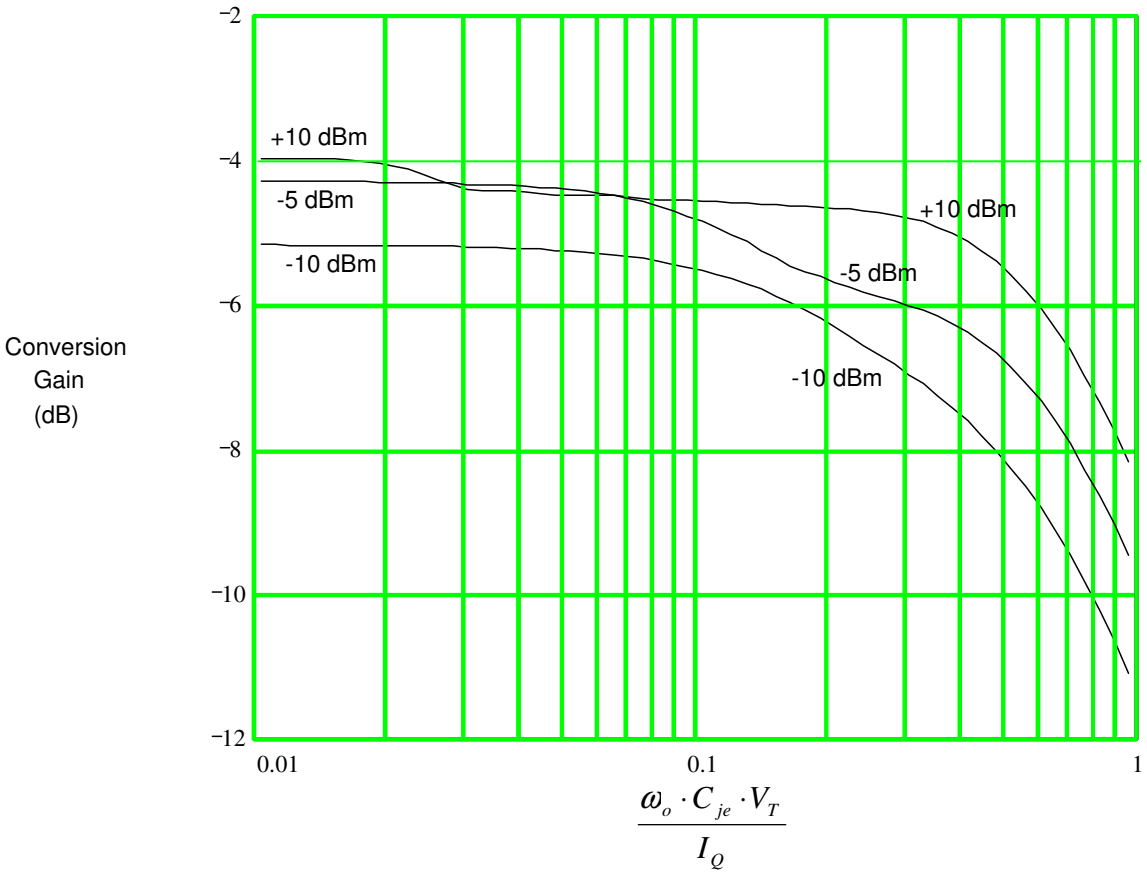

Figure 6: Conversion Gain vs. $\omega_o \cdot C_{je} \cdot V_T / I_Q$

6.7: Parameter Interaction

At high frequencies and moderate current densities the effects of increased transition time (due to r_b) and waveform tilting (due to C_{je} of the off device) combine. Since C_{je} primarily affects the collector current during the non-transition periods, and r_b affects the transition period only, the two effects are, in some sense, orthogonal to each other. That is, each one can be analyzed separately, and the effects of the two can be "added" together. To check the validity of this intuitive assumption, simulations were run with: $\omega_o \cdot C_{je} \cdot V_{LOA} / I_Q = \omega_o \tau_f \cdot r_b \cdot I_Q / V_{LOA} = 0.125,0,25,0.5$. The collector current waveforms for these three cases are shown in Figures 7a,b,c respectively. The current density is the same for each of the three cases.

From Figure 7a, superposition of effects appears to be valid. There is a tilt in the collector current waveform that is quite similar to the one with $\omega_o \cdot C_{je} \cdot V_{LOA} / I_Q = 0.125$ and $\omega_o \tau_f \cdot r_b \cdot I_Q / V_{LOA} = 0$ (Figure 5a). The presence of a reasonably small value of r_b does not seem to change the tilting effect of C_{je}. Likewise, the transition slope is similar to the case where $C_{je} = 0$ (Figure 3a). The turn-off transition time is shorter since there is less current to swing (only about 80% of I_Q). Likewise, the turn-on transition time is somewhat longer.

As the frequency is increased (Figure 7b) the assumption of orthogonality begins to break down. The waveform no longer resembles a square wave. It is difficult to even distinguish the transition time from the non-transition time.

As the frequency is increased further (Figure 7c) the assumption of orthogonality has completely broken down. At these frequencies the interaction of parameters is significant.

A rough maximum frequency for the validity of the orthogonality assumption is:

$$\omega_o \approx \frac{0.25}{\sqrt{\tau_f \cdot r_b \cdot C_{je}}} \qquad (19)$$

If the factors $\omega_o \cdot \tau$ or $\omega_o \cdot r_b \cdot C_{je}$ approach unity, they will also affect the performance. It is therefore assumed that:

$$\omega_o \cdot \tau_f < 0.25 \quad (20a)$$

and

$$\omega_o \cdot r_b \cdot C_{je} < 0.25 \qquad (20b)$$

Given these assumptions, one can conclude that the behavior of the emitter-coupled pair mixer can be understood by analyzing the effects of $\omega_o \cdot C_{je} \cdot V_T / I_Q$ and $\omega_o \tau_f \cdot r_b \cdot I_Q / V_T$ independently.

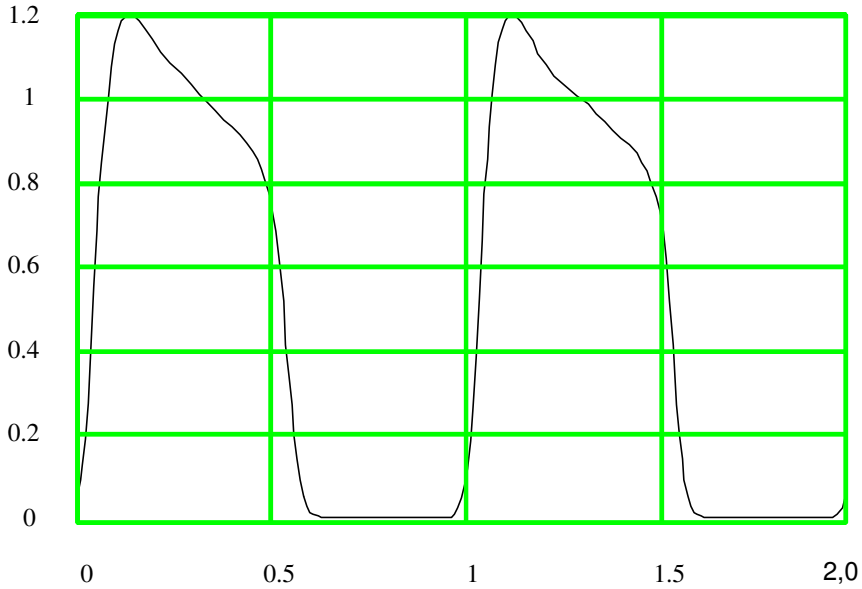

Figure 7a: $I_c(t)$ *vs .time* for $\omega_o \cdot C_{je} \cdot V_{LOA} / I_Q = 0.125$ & $\omega_o \tau_f \cdot r_b \cdot I_Q / V_{LOA} = 0.125$

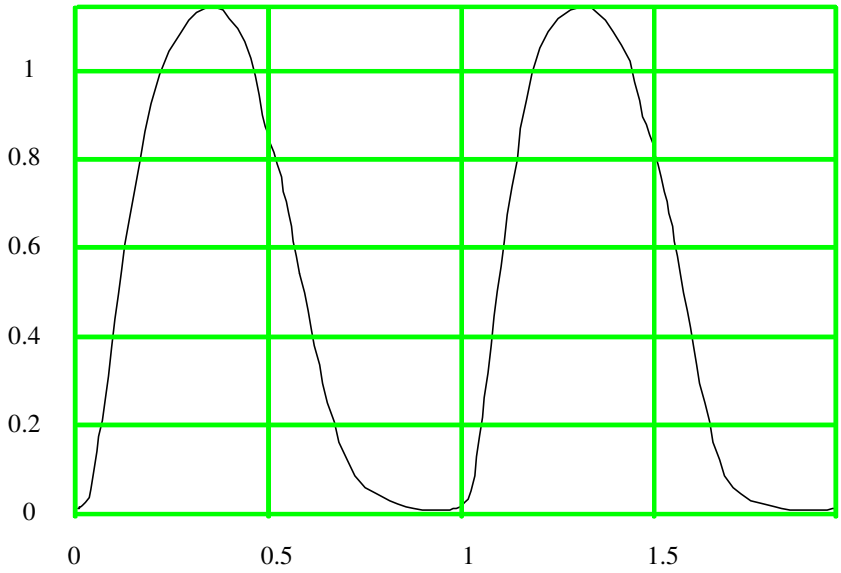

Figure 7b: $I_c(t)$ *vs .time* for $\omega_o \cdot C_{je} \cdot V_{LOA} / I_Q = 0.25$ & $\omega_o \tau_f \cdot r_b \cdot I_Q / V_{LOA} = 0.25$

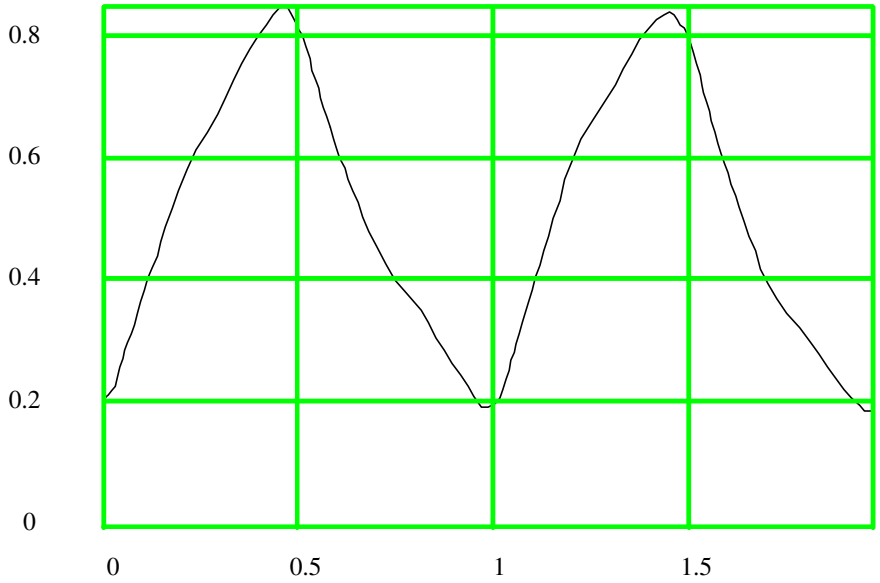

Figure 7c: $I_c(t)$ *vs .time* **for** $\omega_o \cdot C_{je} \cdot V_{LOA} / I_Q = 0.5$ **&** $\omega_o \tau_f \cdot r_b \cdot I_Q / V_{LOA} = 0.5$

6.8: Parametric Relationship to Current Density

Since r_b is inversely proportional to device area, and C_{je} is directly proportional to device area, the product $r_b \cdot C_{je}$ is nearly constant. Below the current density that the Kirk Effect becomes significant, τ_f is nearly constant. Now consider the product of the parameters:

$$\frac{\omega_o \cdot \tau_f \cdot r_b \cdot I_Q}{V_T} \cdot \frac{\omega_o \cdot C_{je} \cdot V_T}{I_Q} = \omega_o{}^2 \cdot r_b \cdot C_{je} \cdot \tau_f$$

For a given frequency, this product is approximately constant. It is convenient to define:

$$\omega_x \equiv \frac{1}{\sqrt{r_b \cdot C_{je} \cdot \tau_f}} \qquad (21a)$$

and

$$K \equiv \frac{r_b \cdot I_Q}{V_T} \cdot \sqrt{\frac{\tau_f}{r_b \cdot C_{je}}} \qquad (21b)$$

then:

$$\frac{\omega_o \cdot \tau_f \cdot r_b \cdot I_Q}{V_T} = K \cdot \frac{\omega_o}{\omega_x} \qquad (22a)$$

$$\frac{\omega_o \cdot C_{je} \cdot V_T}{I_Q} = \frac{1}{K} \cdot \frac{\omega_o}{\omega_x} \quad (22b)$$

The parameter K is proportional to the current density, and will be referred to as the *current density factor.* Increasing the current density factor increases the importance of the parameter $\omega_o \cdot \tau_f \cdot r_b \cdot I_Q / V_T$ and decreases the importance of the parameter $\omega_o \cdot C_{je} \cdot V_T / I_Q$. Decreasing the current density factor has the opposite effect. If $\omega_o << \omega_x$ then only one of the parameters can be near unity. It was previously asserted that if $\omega_o \cdot \tau_f < 0.25$ and $\omega_o \cdot r_b \cdot C_{je} < 0.25$, then the assumption that the effects are orthogonal is reasonable. These two conditions imply that the maximum frequency where orthogonality of effects can hold is given by: $\omega_o = 0.25 \cdot \omega_x$. This frequency is extremely important, since it represents (in some sense) the maximum frequency that the mixer can be used without substantial degradation in performance (as is shown in Chapters 7-9).

6.9: Conversion Gain at Moderate Current Densities

The conversion gain at moderate current densities is obtained by combining the effects of low and high current densities.

EXAMPLE: $\omega_o \cdot C_{je} \cdot V_{LOA} / I_Q = 0.125$

$\omega_o \tau_f \cdot r_b \cdot I_Q / V_{LOA} = 0.125$

$V_{loa} = 178mV$

At low frequencies ($r_b = C_{je} = 0$) the conversion gain for this LO amplitude is -4.2dB. From Figure 6, the conversion gain if r_b were zero would be about -4.9dB. From Figure 4, the conversion gain if C_{je} were zero is -4.0dB. The effect of the r_b parameter is to increase the conversion gain by 0.2dB, and the effect of the C_{je} parameter is to decrease the gain by 0.7 dB. Since the effects are approximately orthogonal, the net effect is a decrease in conversion gain by 0.5 dB. Thus the conversion gain is approximately -4.7dB. Simulations have verified the accuracy of this assertion.

Chapter 7: Noise in the Emitter-Coupled Pair

Before analyzing the noise performance of the mixer, it is helpful to consider the output noise of an emitter-coupled pair amplifier (Figure 1). If the base shot noise is neglected, then the differential output current noise at low frequencies is given by:

$$i_{odn}{}^2 = 2 \cdot q \cdot I_Q \cdot \Delta f \cdot \left[1 + \frac{r_b \cdot I_Q}{V_T} \right] \qquad (1)$$

The first term in Equation 1 is due to the collector shot-noise, and the second term is due to the base ohmic resistance.

At high frequencies, the output noise due to r_b is reduced because of the single pole response of the circuit (which reduces the gain at high frequencies). The total output noise at high frequencies is given by:

$$i_{odn}{}^2(j \cdot \omega) = 2 \cdot q \cdot I_Q \cdot \Delta f \cdot \left[1 + \frac{r_b \cdot I_Q}{V_T} \cdot \frac{1}{1 + (r_b \cdot C_\pi \cdot \omega)^2} \right] \qquad (2)$$

.

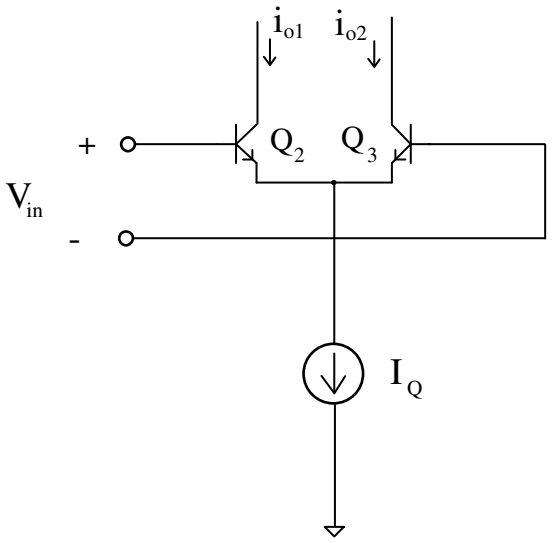

Figure 1: Emitter-Coupled Pair Amplifier

For a single-ended output, the noise output and signal output are each nominally reduced by 6 dB. However, any noise present in the current source no longer cancels, and the output noise may increase significantly above the value given by Equation 2.

Now consider the case where the input voltage has a DC offset. The output noise will be changed, since the device operating points change. The normalized DC offset is defined by:

$$b \equiv \frac{V_{OS}}{V_T}$$

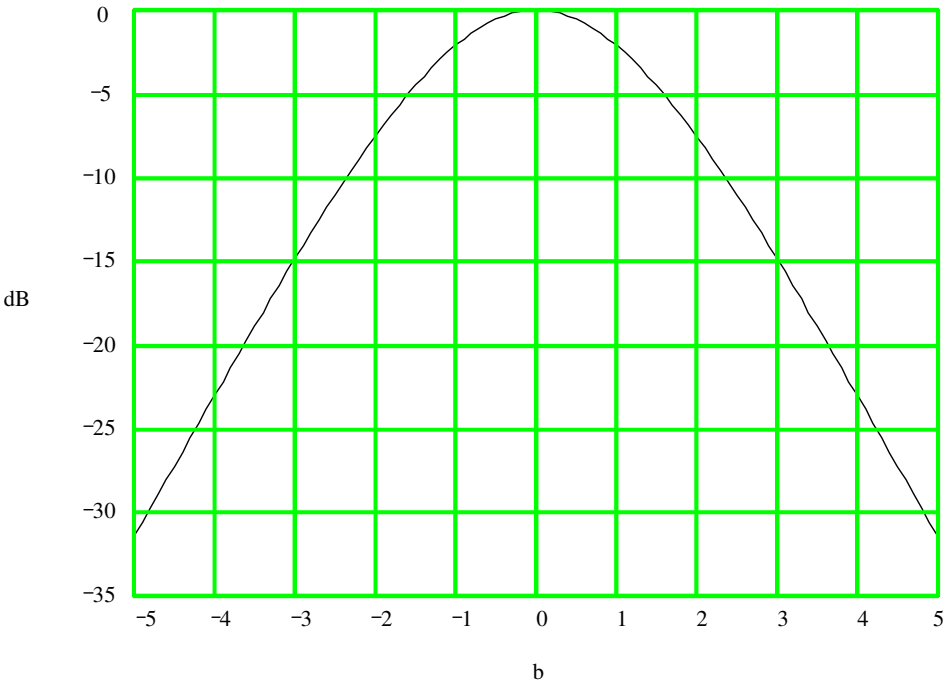

Figure 2: Relative Shot Noise vs. DC Offset in an Emitter-Coupled Pair Amplifier

At low frequencies, the output noise in the presence of a DC offset is given by:

$$i_{odn}{}^2 = 2 \cdot q \cdot I_Q \cdot \Delta f \cdot \left[\frac{1}{\cosh^2(b/2)} + \frac{r_b \cdot I_Q}{V_T} \cdot \frac{1}{\cosh^4(b/2)} \right] \tag{3}$$

The output noise decreases with either a positive or negative DC offset. In Figure 2, the change in the shot noise component against the DC offset is shown. With a DC offset, the noise contribution from r_b decreases more rapidly than the shot noise component. The change in the r_b noise component will be twice

as much in dB. Note that for an offset voltage of magnitude greater than 100mV ($b \approx 4$) the output noise is reduced drastically.

There are two factors that cause the output noise to be reduced with increasing offset voltage. First, as the magnitude of the offset voltage increases, the bias current through one of the transistors decreases. This reduces both its transconductance (thus affecting the base-ohmic noise component) and its shot noise. Although the current in the other device increases, the impedance at its emitter increases sufficiently to reduce the output noise.

7.1: Noise in the Emitter-Coupled Pair Mixer at Low Frequencies

In a mixer (as with any other circuit) there are two sources of noise at the output: intrinsic noise created by the circuit elements within the mixer, and extrinsic noise which is transferred from the input ports of the mixer to its output port. In linear amplifiers extrinsic noise is multiplied by the same gain as the signal, so it is not necessary to give it special attention. For example, in specifying the noise figure of an amplifier, it is understood that the noise from previous stages will increase the output noise. For mixers the situation is complicated by its inherently non-linear characteristic, the associated translation of frequencies, and the multiplicity of ports. For this reason it is important to consider the characteristics of the mixer with respect to extrinsic as well as intrinsic noise sources.

Intrinsic Noise of the ECP Mixer At Low Frequencies

As shown in Chapter 5, if the input spectral density is white then the output noise is given by:

$$S_{yo} = S_{xo} \cdot \frac{1}{T} \cdot \int_0^T h^2(t)dt \tag{4}$$

That is, the output noise is the mean-squared gain times the input noise. This is equivalent to taking the mean-square value of the output noise as a function of time. If the input voltage for the emitter-coupled pair is given by:

$$V_{in}(t) = V_{LOA} \cdot \sin(t) = b \cdot V_T \cdot \sin(t)$$

then intrinsic output noise of the emitter-coupled pair at low frequencies is given by:

$$i_{odn}{}^2 = 2 \cdot q \cdot I_Q \cdot \Delta f \cdot \left[f_1(b) + \frac{r_b \cdot I_Q}{V_T} \cdot f_2(b) \right] \tag{5a}$$

where:

$$f_1(b) \equiv \frac{1}{T} \cdot \int_0^T \frac{dt}{\cosh^2\left(\frac{b}{2} \cdot \sin(t)\right)} \tag{5b}$$

$$f_2(b) \equiv \frac{1}{T} \cdot \int_0^T \frac{dt}{\cosh^4\left(\frac{b}{2} \cdot \sin(t)\right)} \tag{5c}$$

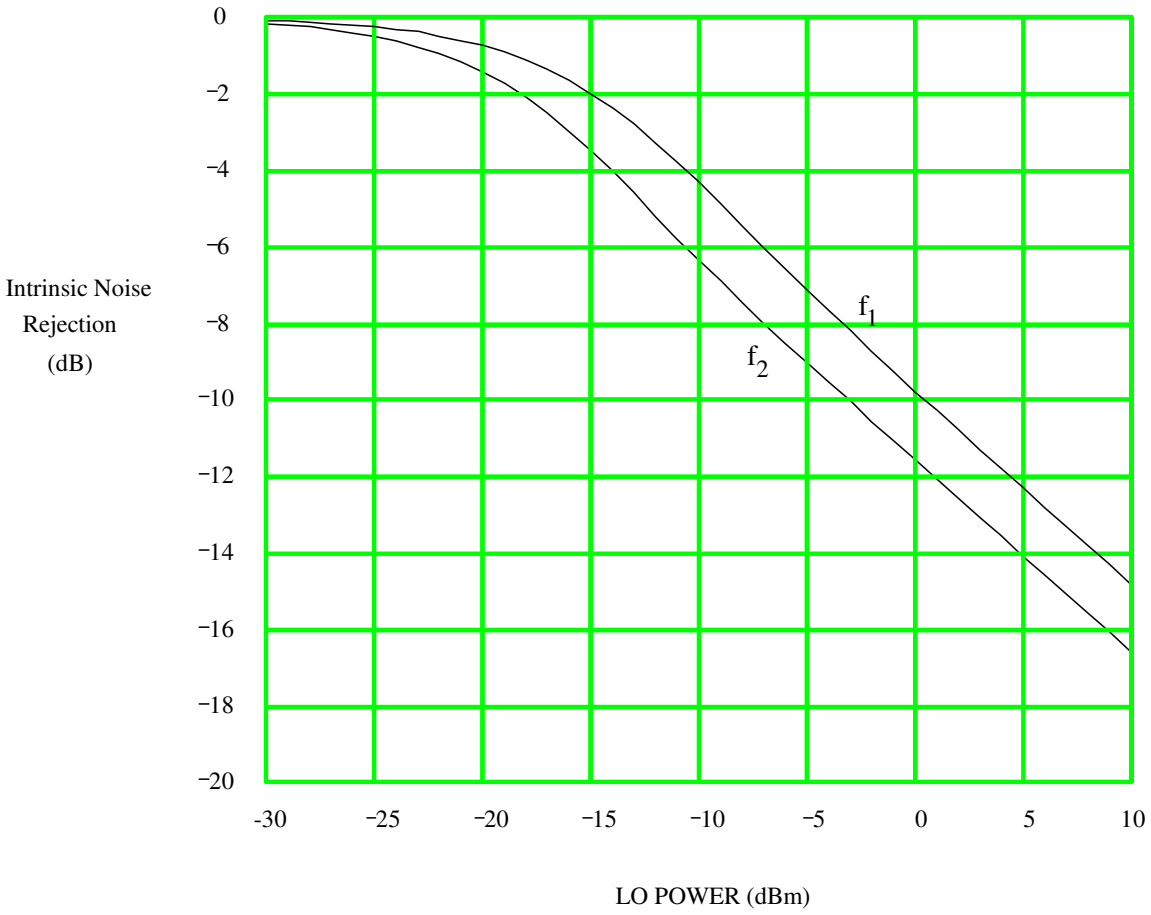

Figure 3: Rejection of base-ohmic and collector shot-noise vs. LO Power

The functions f_1 and f_2 are plotted in Figure 3 as a function of LO Power. Note that for small LO amplitudes the output noise approaches that of the emitter-coupled pair amplifier. As the LO power is increased, the output noise decreases.

A convenient way of seeing this is to consider the noise contribution during the transition time and non-transition time (these terms are discussed in Chapter 6). During the transition time both devices are on, and the output noise is close to that of the ECP amplifier. During non-transition times, the output noise contribution is quite small since the on device sees a high impedance from its emitter to ground. To clarify this point, a schematic is shown of the ECP switch when device Q_2 is off. Since transistor Q_1 sees an open circuit at its emitter (for ac signals), amplification is reduced, and the output noise is negligible. It can be shown that the output noise of the configuration in Figure 4 is given by:

$$i_{odn}{}^2 = 2 \cdot q \cdot I_Q \cdot \Delta f \cdot \frac{1}{\beta_o}$$

For $\beta_o = 100$ this output noise is reduced by at least 20dB from the zero-bias case. In fact, the base-ohmic noise component is completely rejected, and the shot noise is rejected by a factor of β_o. For LO amplitudes greater than 1V (+10 dBm) the transition time becomes so short that the noise during non-transition times may become significant.

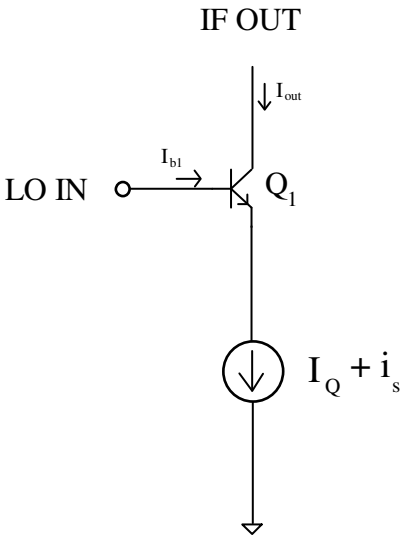

Figure 4: Emitter-Coupled Pair when Q_2 is "off"

Referring to Figure 3, one can see that as the LO amplitude increases the output noise decreases at a rate approaching 0.5dB per dB of LO power. This result is not surprising since a 6dB increase in LO amplitude increases the slope of the LO signal by a factor of two. This in turn decreases the transition time by a factor of two, and therefore the output noise by about 3dB.

Extrinsic Noise of the ECP Mixer at Low Frequencies

The emitter-coupled pair mixer, as with all mixers, has two input ports. Therefore, it is important to characterize the response to noise for both input ports. The response to noise from the LO input port is essentially identical to that of the response to r_b noise. The reason for this is that the noise sources for r_b appear in series with the LO source. Assuming the input spectrum is white, the output variance is given by:

$$i_{odn}{}^2 = g_m{}^2 \cdot f_2\left[\frac{V_{LOA}}{V_T}\right] \cdot v_{idn}{}^2 \tag{6}$$

If a double-balanced configuration is used (see Chapter 2, Figure 11) then noise from the LO port is rejected. For single-balanced mixers it is necessary to place a band-pass filter between the LO and the input of the mixer. This band-pass filter will reject all noise components except those that are very close to the LO frequency. Referring to Figure 11 of Chapter 5, we see that for an ECP mixer, noise near odd harmonics of the LO frequency tends to be rejected. This occurs because of the absence of even-order distortion components in the ECP power series (See distortion analysis of ECP in Chapter 4). In other mixer configurations this is not necessarily the case (e.g. diode and single transistor mixers), and the use of unbalanced configurations with LO noise will produce poor mixer noise performance. To see this, consider the effect of a second-order term on noise at the signal (or image frequency) which is incident at the LO port.

$$\begin{aligned} v_o &= \ldots + a_2 \cdot v_{in1} \cdot v_{in2} = \ldots + a_2 \cdot v_n \cdot V_{LOA} \cdot \cos(\omega_s \cdot t) \cdot \cos(\omega_o \cdot t) \\ &= \ldots + \frac{1}{2} \cdot v_n \cdot V_{LOA} \cdot \left[\cos\left[(\omega_s - \omega_o) \cdot t\right] + \cos\left[(\omega_s + \omega_o) \cdot t\right]\right] \end{aligned}$$

From this equation it is seen that noise components are produced at the IF frequency (as well as a frequency near $2 \cdot \omega_o$).

Extrinsic noise from the signal port also contributes to the output noise, since:

$$I_{od} = I_{EE} \cdot \tanh\left[\frac{V_{LO}}{2 \cdot V_T}\right] = \left[I_Q + i_s\right] \cdot \tanh\left[\frac{V_{LOA} \cdot \sin(\omega_o \cdot t)}{2 \cdot V_T}\right]$$

$$i_{odn}{}^2 = i_{idn}{}^2 \cdot \frac{1}{2 \cdot \pi} \cdot \int_0^{2 \cdot \pi} \tanh^2\left[\frac{V_{LOA}}{2 \cdot V_T} \cdot \sin(t)\right] dt \qquad (7a)$$

let

$$f_3(b) \equiv \frac{1}{2 \cdot \pi} \cdot \int_0^{2 \cdot \pi} \tanh^2\left[\frac{b}{2} \cdot \sin(t)\right] dt$$

then:

$$i_{odn}{}^2 = i_{idn}{}^2 \cdot f_3\left[\frac{V_{LOA}}{V_T}\right] \qquad (7b)$$

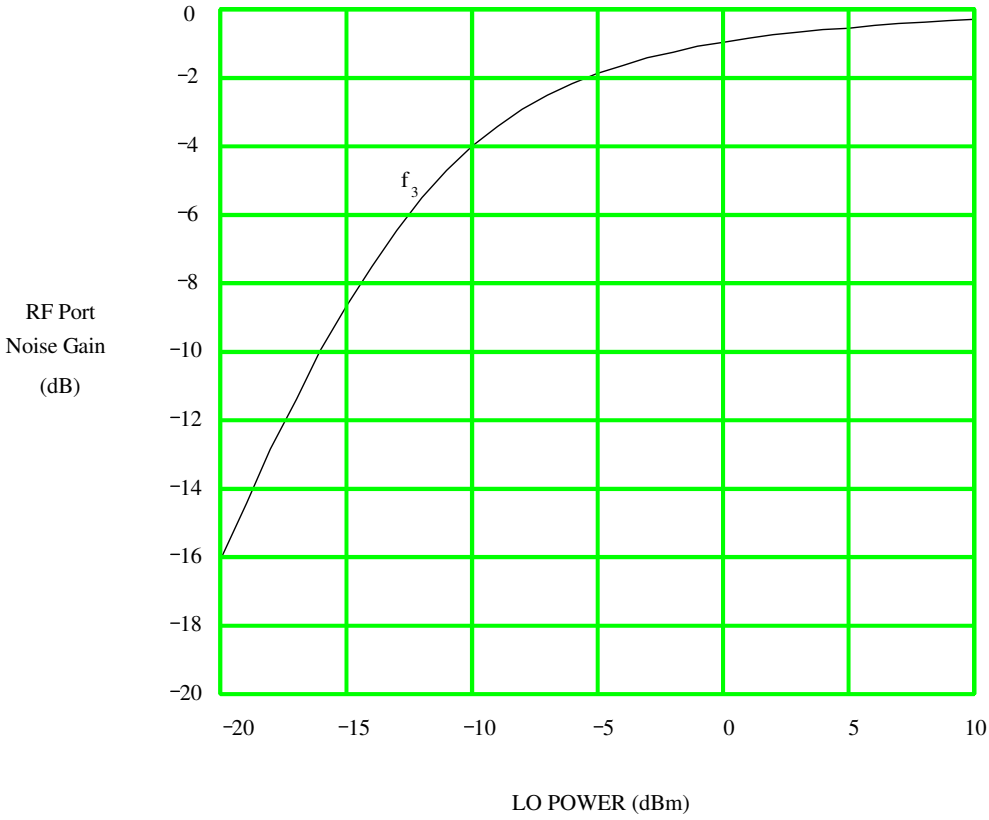

Figure 5: White Noise Gain from RF to IF port vs. LO Power

The RF input port noise gain (f_3) as a function of LO power is plotted in Figure 5. Note that the gain increases with increasing LO power. This is due to the increasing conversion efficiency of the mixer. At very large LO amplitudes the noise gain approaches unity. This situation corresponds to an ideal switch

that is chopping white noise. Since white noise varies infinitely fast, intuitively one would expect that chopping it (multiplying it by +1 or -1 depending on the LO phase) would not affect its statistics.

It is interesting to compare the conversion gain of white noise to that of a narrowband signal. From Equation 11 of Chapter 6, the conversion gain (at low frequencies) is given by:

$$a_{ic}(b) = \frac{1}{2 \cdot \pi} \cdot \int_0^{2 \cdot \pi} \tanh\left[\frac{b}{2} \cdot \sin(t)\right] \cdot \sin(t) dt$$

$$b \equiv \frac{V_{LOA}}{V_T}$$

The ratio of the white noise gain to the signal conversion gain when expressed in terms of power is given by:

$$f_4(b) \equiv \frac{f_3(b)}{a_{ic}{}^2(b)}$$

This function is plotted in Figure 6a. Over the range of LO powers, f_4 is between 3.0 and 3.9 dB, indicating that white noise has higher conversion gain than a signal does. There are two reasons that the noise gain is higher. First, noise sources at the image frequency produce additional noise at the output of equal magnitude to those at the signal frequency (thus adding 3dB to the output noise). Second, the conversion of noise from higher order harmonics down to the IF frequency contributes up to an additional 0.93dB of noise.

Notice that for weak LO powers (< -20 dBm) the difference in signal gain and conversion gain is only 3dB, indicating negligible conversion from higher harmonics. As the LO power is increased, the spectral content of the modulating signal becomes richer, and the amount of output noise increases. In the limit of very large LO amplitudes, the difference approaches a factor of $\pi/2$ or 3.92 dB.

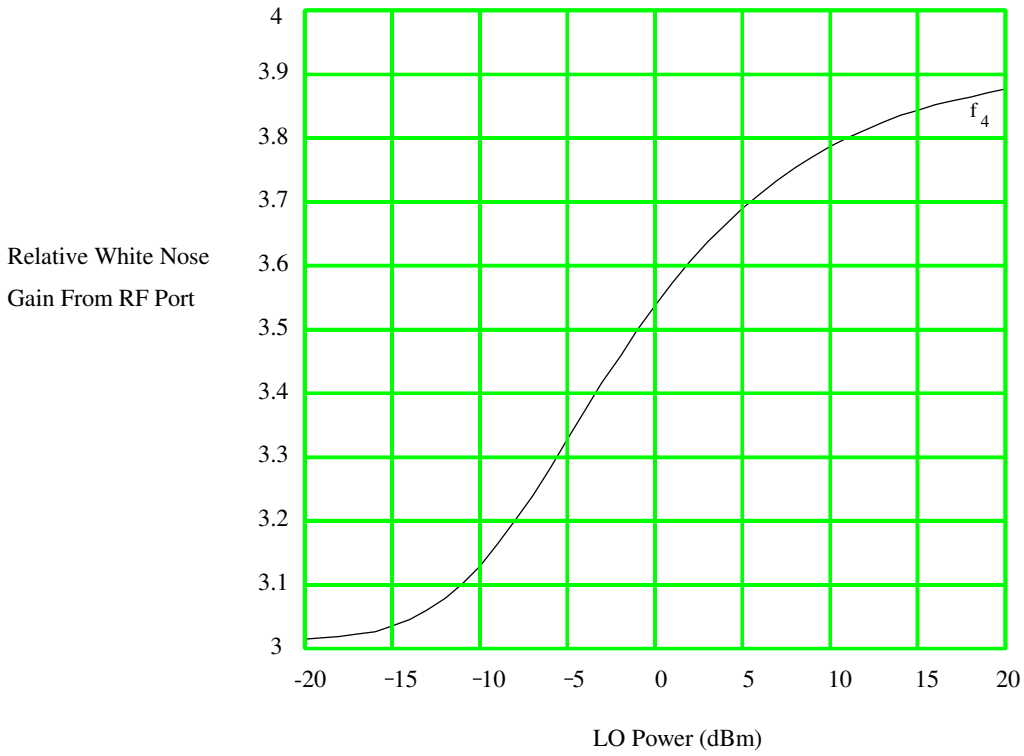

Figure 6a:Conversion gain of White Noise Relative to Signals

Extrinsic Noise For an ECP Mixer with Single-Ended Output

Often it is more convenient to take a single ended output from the emitter-coupled pair mixer. This avoids the use of current mirrors or BALUNS. However, taking a single ended output degrades the noise performance. The reason for this is that a single-ended output yields an unbalanced mixer. That is, signals at the input port at ω_{if} pass through to the output port with little rejection (see Chapter 2).

To see the quantitative effect on noise, consider the large signal equation for the mixer when a single ended output is taken:

$$I_{od} = \frac{I_{EE}}{2} \cdot \left[1 + \tanh\left[\frac{V_{LOA}}{2 \cdot V_T} \cdot \sin(\omega_o \cdot t) \right] \right] \tag{8a}$$

The output noise is then:

$$i_{odn}{}^2 = i_{idn}{}^2 \cdot \frac{1}{2 \cdot \pi} \cdot \frac{1}{4} \cdot \int_0^{2 \cdot \pi} \left[1 + \tanh\left[\frac{V_{LOA}}{2 \cdot V_T} \cdot \sin(t) \right] \right]^2 \cdot dt = \left[\frac{i_{idn}}{2} \right]^2 \cdot \left[1 + f_3(b) \right] \tag{8b}$$

The conversion gain is:

$$a_{ics}(b) = \frac{1}{2\cdot\pi}\cdot\frac{1}{2}\int_0^{\pi}\left[1+\tanh\left[\frac{b}{2}\cdot\sin(t)\right]\right]\cdot\sin(t)dt = \frac{a_{ic}}{2}$$

The conversion gain is reduced by 6dB for a single-ended output.

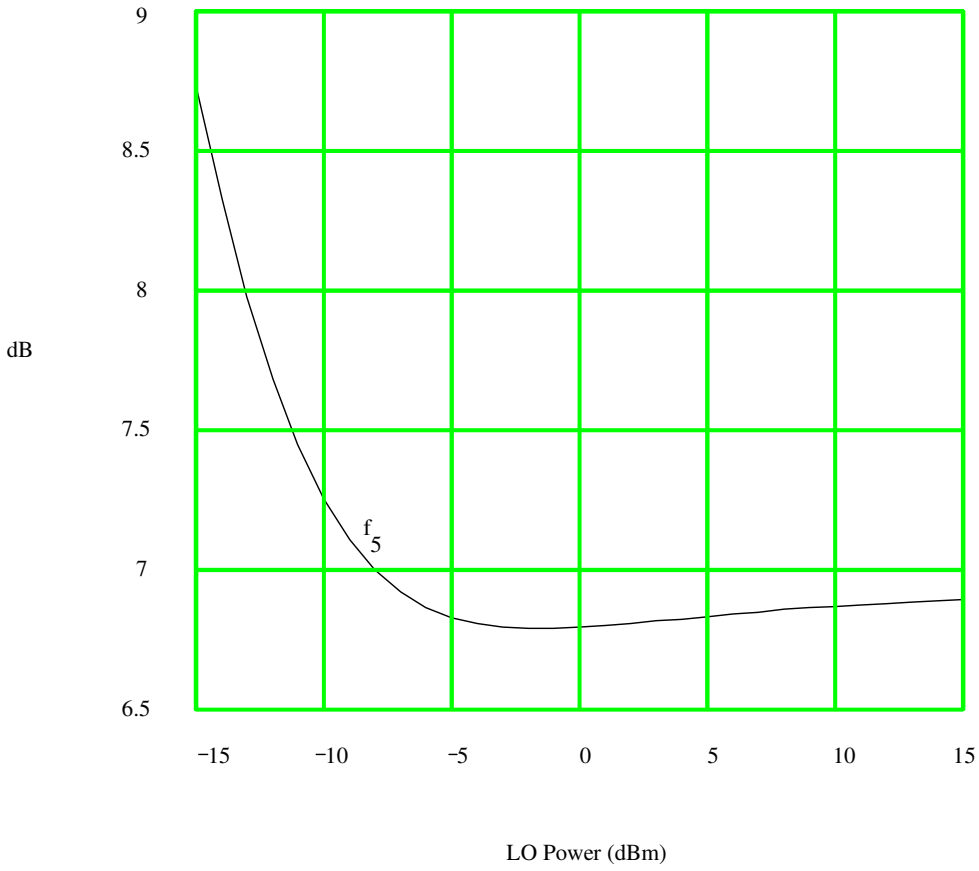

Figure 6b:Conversion gain of White Noise Relative to Signals for a single-ended output

The ratio of the white noise gain to the signal conversion gain when expressed in terms of power is given by:

$$f_5(b) \equiv \frac{\left[1+f_3(b)\right]/2^2}{a_{ic}{}^2(b)/2^2} = \frac{1}{a_{ic}{}^2} + f_4(b) \qquad (9)$$

The first term in Equation 9 is due to the noise at the signal port at the intermediate frequency. It is this additional term that increases the output noise. From Equation 8b it is seen that the first term corresponds to

noise gain that is independent of LO power. In effect, the noise at the IF frequency passes through with a gain of 0.5 regardless of the LO power.

The function f_5 is plotted against LO power in Figure 6b. Notice that the performance degrades rapidly for LO powers lower than -10dBm. This is because the signal gain drops while the noise gain remains nearly constant for $P_{LO} < -10\text{dBm}$. In this circumstance the dominant noise source is due to IF noise passing directly from the input port to the output port.

7.2: Noise in the Emitter-Coupled Pair Mixer at High Frequencies

As discussed in Chapter 6, Section 7, the effects of the parameters $\omega_o \tau_f \cdot r_b \cdot I_Q / V_T$ and $\omega_o \cdot C_{jeo} \cdot V_T / I_Q$ may be assumed orthogonal. As with low frequencies, one must consider three major noise sources: collector shot noise, noise incident at the LO port (including noise from the ohmic base resistance), and noise incident at the signal port.

Because of the non-linear nature of the circuit function, no closed-form solution is available. Since the solution is known to depend on a few normalized parameters (See Equation 9 of Chapter 6), it is convenient to express the output noise at high frequencies in the form:

$$i_{odn}{}^2 = 2 \cdot q \cdot I_Q \cdot \Delta f \cdot \left[f_1\left[\frac{V_{LOA}}{V_T}, \omega_o \cdot \tau_f, \frac{r_b \cdot I_Q}{V_T}, \frac{\omega_o C_{je} \cdot V_T}{I_{EE}} \right] + \frac{r_b \cdot I_Q}{V_T} \cdot f_2\left[\frac{V_{LOA}}{V_T}, \omega_o \cdot \tau_f, \frac{r_b \cdot I_Q}{V_T}, \frac{\omega_o C_{je} \cdot V_T}{I_{EE}} \right] \right] \tag{10}$$

When $\omega_o \to 0$, Equation 10 reduces to Equation 5a.

For low LO frequencies significant output noise exists only during the short time when both devices are active (the transition time). However, at high frequencies there may be output noise during the non-transition times. To see this, consider the case where transistor Q_1 is on and Q_2 is off (see Figure 7). At high frequencies the impedance seen at the emitter of Q_1 is reduced because of the base-emitter junction capacitance of Q_2. Since parasitic capacitances tend to be more significant at low current densities, this noise contribution is expected to be most significant when the current density is low and the frequency is high.

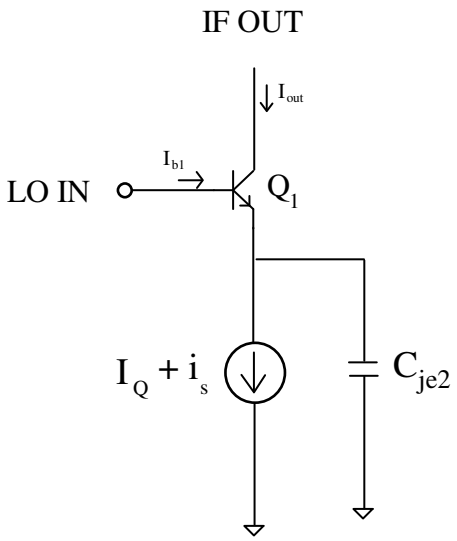

Figure 7: ECP Mixer with Q_2 "off"

Noise at High Current Density

At higher current density the parasitic capacitances tend to be small, and the dominant time constant is $r_b \cdot C_b$ (which is proportional to $\tau \cdot r_b \cdot I_Q / V_T$). As seen in Chapter 6, the main change in the collector current waveform is an increase in the transition time (relative to a period) for increasing values of the parameter $\omega_o \cdot \tau \cdot r_b \cdot I_Q / V_{LOA}$.

It is expected that an increase in transition time will cause an increase in the output noise. Therefore, one would expect the output noise to increase monotonically with $\omega_o \cdot \tau \cdot r_b \cdot I_Q / V_{LOA}$. However, while the shot noise component does increase monotonically with $\omega_o \cdot \tau \cdot r_b \cdot I_Q / V_{LOA}$, the base-ohmic noise component does not. To understand this one need only consider the output noise of the emitter-coupled pair amplifier at high frequencies. If C_{je} is neglected, the output noise variance in an ECP is given by:

$$i_{odn}{}^2 = 2 \cdot q \cdot I_Q \cdot \Delta f \cdot \left[1 + \frac{r_b \cdot I_Q}{V_T} \cdot \frac{1}{1 + (\omega \cdot r_b \cdot C_b)^2} \right] \tag{11}$$

As seen from Equation 11, the output noise of an emitter-coupled pair amplifier decreases with frequency (this is especially true at high current densities where the r_b noise component dominates and the $r_b \cdot C_b$

time constant is large). Hence, there are two conflicting effects: a decrease in the output noise due to the $r_b \cdot C_b$ time constant, and an increase in noise due to the increased transition time.

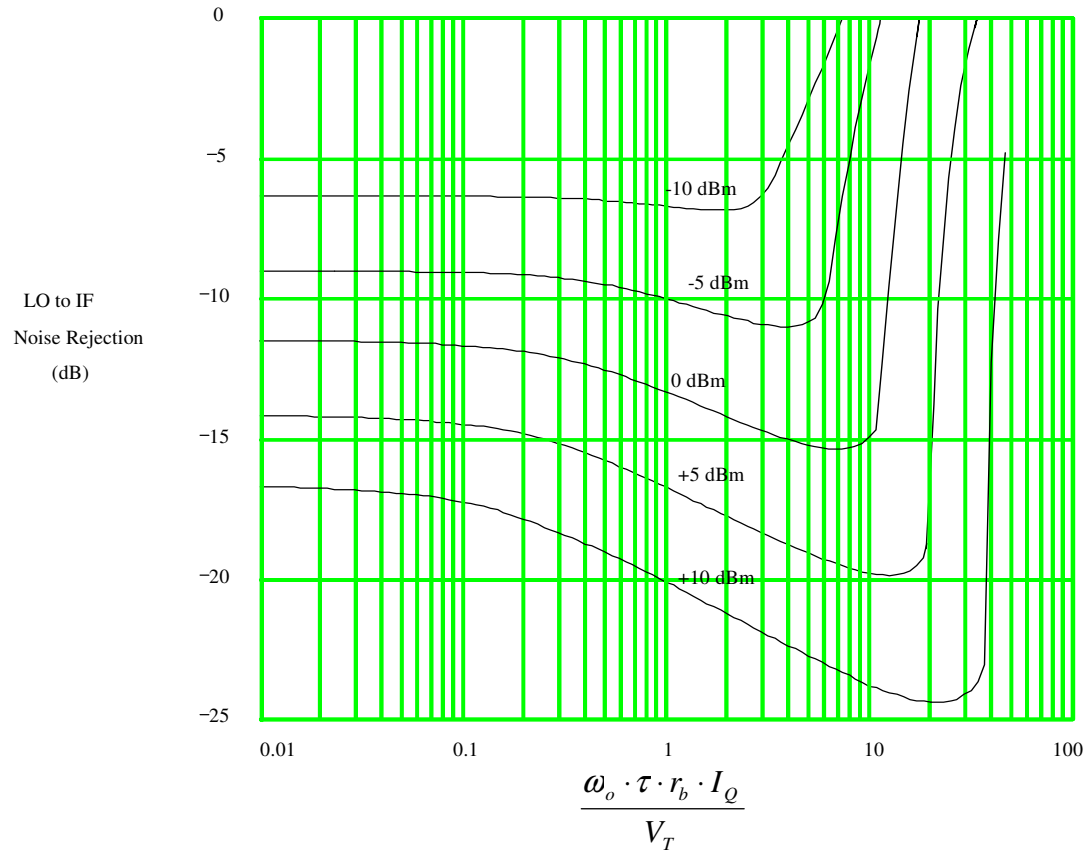

Figure 8a: Noise Rejection Factor (f_2) from LO to IF port vs. $\omega_o \cdot \tau \cdot r_b \cdot I_Q / V_T$

To find out what actually happens, noise simulations were run using the methods of Chapter 5. In Figure 8a the function f_2 (which is the rejection of the base-ohmic noise at the output) is plotted against $\omega_o \cdot \tau \cdot r_b \cdot I_Q / V_T$ for LO amplitudes of 100mV, 178mV, 316mV, 562mV, and 1V. These amplitudes correspond to LO powers of -10dBm, -5dBm, 0dBm, +5dBm, and +10dBm, respectively, into a 50 ohm load. Initially as the parameter $\omega_o \cdot \tau \cdot r_b \cdot I_Q / V_T$ increases, the output noise decreases. However, when $\omega_o \cdot \tau \cdot r_b \cdot I_Q / V_T$ exceeds a certain value (which is dependent on LO power), the output noise increases rapidly.

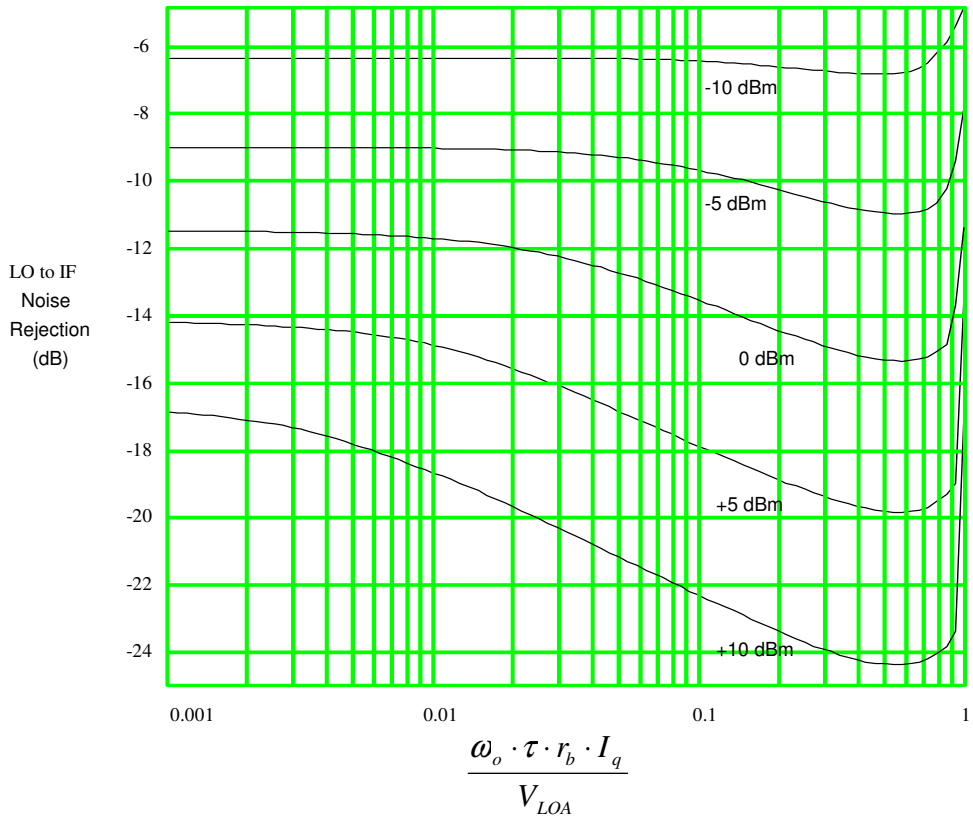

Figure 8b: Noise Rejection Factor (f_2) from LO to IF port vs. $\omega_o \cdot \tau \cdot r_b \cdot I_Q / V_{LOA}$

The frequency at which the noise begins to increase rapidly can be seen more clearly by plotting f_2 against $\omega_o \cdot \tau \cdot r_b \cdot I_Q / V_{LOA}$ (Figure 8b), since this parameter is most closely related to the transition time. Note that as $\omega_o \cdot \tau \cdot r_b \cdot I_Q / V_{LOA}$ approaches unity, the output noise begins to increase rapidly. To understand why the noise increases so rapidly it is necessary to consider the collector current waveform as the parameter $\omega_o \cdot \tau \cdot r_b \cdot I_Q / V_{LOA}$ approaches unity. Looking at Figures 3b&c of Chapter 6, it is clear that as $\omega_o \cdot \tau \cdot r_b \cdot I_Q / V_{LOA}$ approaches unity, the collector current waveform loses its square wave shape and becomes a sine wave. When the collector current waveform is sinusoidal, both devices remain active at all times. Hence, the output noise rejection is poor.

Since the output noise increases rapidly and the conversion gain decreases rapidly for $\omega_o \cdot \tau \cdot r_b \cdot I_Q / V_{LOA} \geq 1$, it is necessary to restrict operation to frequencies with

$\omega_o \cdot \tau \cdot r_b \cdot I_Q / V_{LOA} < 1$. Because of parametric variations over supply, process, and temperature, it is best for a nominal design to have $\omega_o \cdot \tau \cdot r_b \cdot I_Q / V_{LOA} < 0.5$.

In Figure 9a the shot noise rejection factor, f_1, is plotted against $\omega_o \cdot \tau \cdot r_b \cdot I_Q / V_T$. As expected, the shot noise increases monotonically with frequency. The noise rejection is about 3dB less than its low frequency value when $\omega_o \cdot \tau \cdot r_b \cdot I_Q / V_T = 1$.

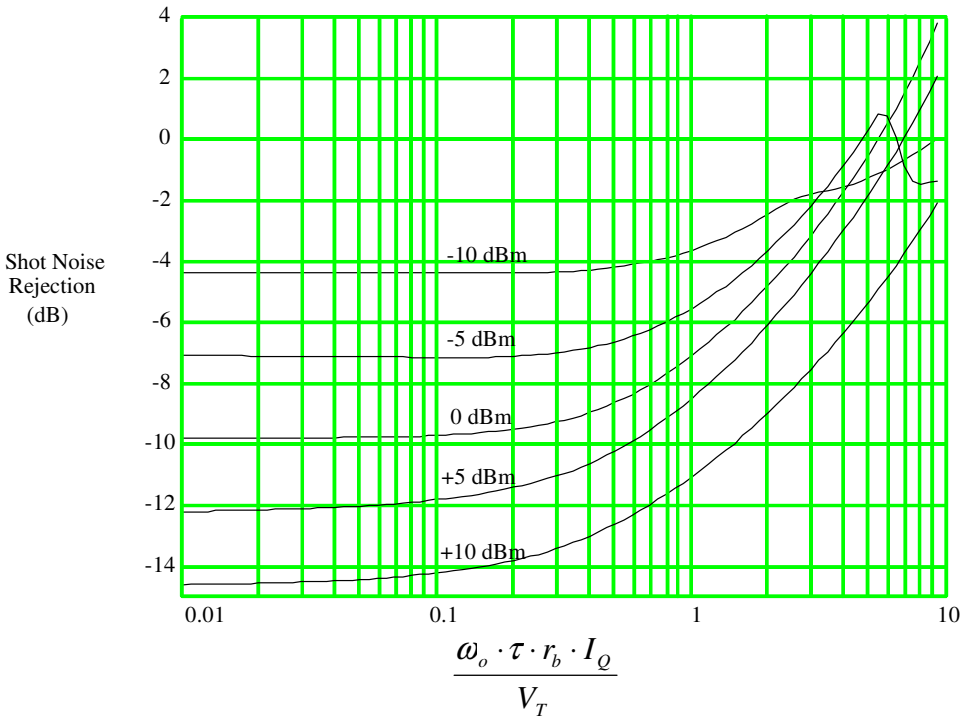

Figure 9a: Shot Noise Rejection Factor (f_1) vs. $\omega_o \cdot \tau \cdot r_b \cdot I_Q / V_T$

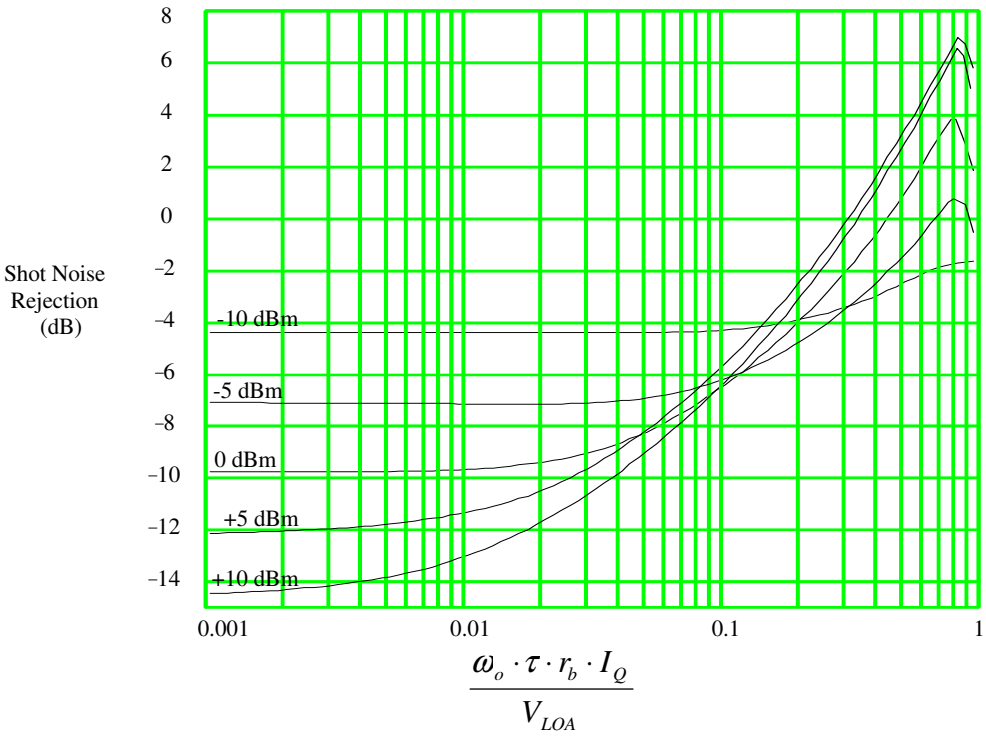

Figure 9b: Shot noise rejection Factor (f_1) vs. $\omega_o \cdot \tau \cdot r_b \cdot I_Q / V_{LOA}$

In Figure 9b, the shot noise rejection is plotted against the parameter $\omega_o \cdot \tau \cdot r_b \cdot I_Q / V_{LOA}$. The output noise (due to the shot noise component) reaches a maximum $\omega_o \cdot \tau \cdot r_b \cdot I_Q / V_{LOA} = 0.8$ and then decreases. However for $\omega_o \cdot \tau \cdot r_b \cdot I_Q / V_{LOA} > 0.8$, the output noise due to r_b is increasing rapidly. Since the r_b noise component is the dominant one at high frequencies, the overall output noise will increase for $\omega_o \cdot \tau \cdot r_b \cdot I_Q / V_{LOA} > 0.8$.

In addition to the base-ohmic noise and shot noise, one must consider the noise incident at the signal port. In Figure 10, the signal-port white-noise gain relative to the signal gain is plotted against $\omega_o \cdot \tau \cdot r_b \cdot I_Q / V_{LOA}$. Note that as $\omega_o \cdot \tau \cdot r_b \cdot I_Q / V_{LOA}$ increases, the noise gain increases. As with the shot noise, the white-noise gain reaches a maximum near $\omega_o \cdot \tau \cdot r_b \cdot I_Q / V_{LOA} = 0.8$. At both low and high frequencies, the white-noise gain is worse for large LO amplitudes, because of the increased harmonic content of the collector current waveform.

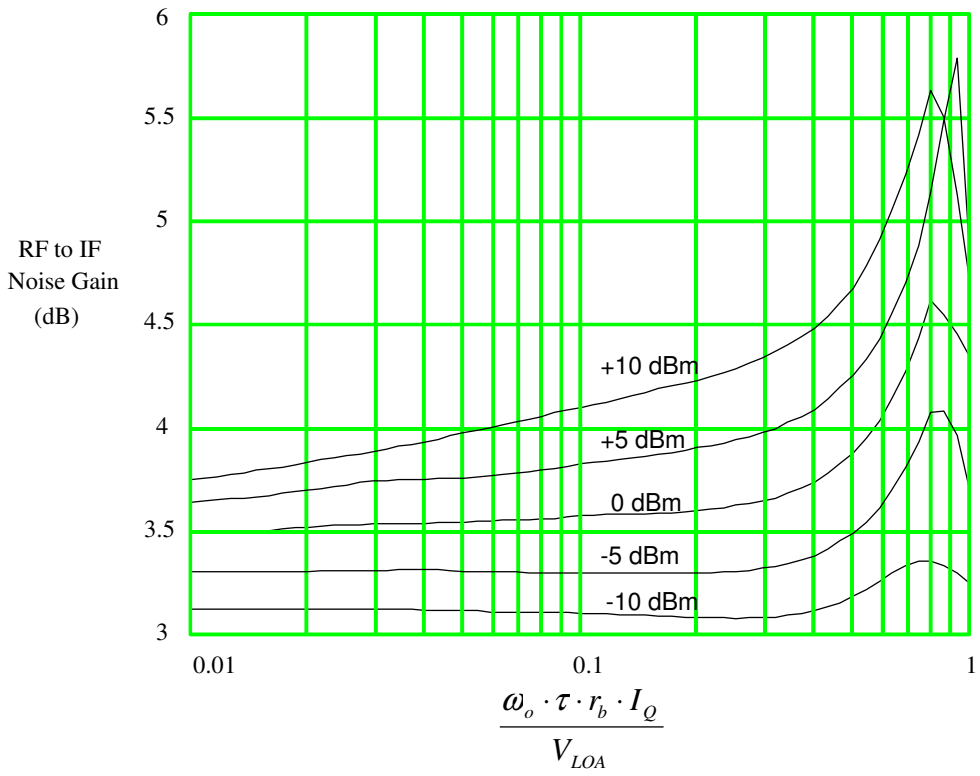

Figure 10: RF to IF white noise gain vs. $\omega_o \cdot \tau \cdot r_b \cdot I_Q / V_{LOA}$

Noise at Low Current Density:

At low current density the resistive parasitics tend to be insignificant, and the capacitive parasitics dominate. As discussed in Chapter 6, the dominant effect at low current densities is the collector current waveform "tilting" due to the C_{je} of the off device. The transition time is fairly independent of the parameter $\omega_o \cdot C_{jeo} \cdot V_{LOA} / I_Q$. The reason for this is that the time constant $r_b \cdot C_{je}$ is very short compared to a period if $\omega_o \cdot r_b \cdot C_{je} << 1$.

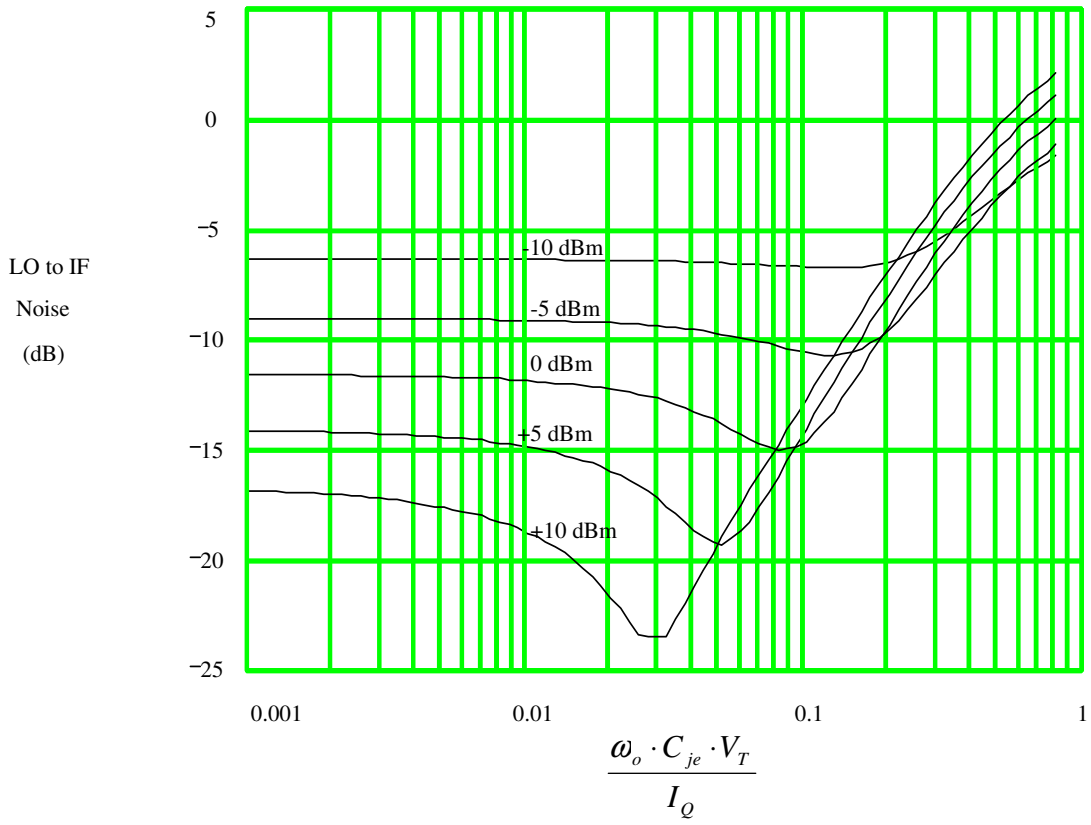

Figure 11a: Noise Rejection Factor (f_2) from LO to IF port vs. $\omega_o \cdot C_{jeo} \cdot V_T / I_Q$

As discussed previously, at low current densities there may be significant noise contribution during the non-transition times. Simulations were run over a wide range of values for the parameter $\omega_o \cdot C_{jeo} \cdot V_{LOA} / I_Q$. LO amplitudes used were 100mV, 178mV, 316mV, 562mV, and 1V as with other noise and conversion gain simulations.

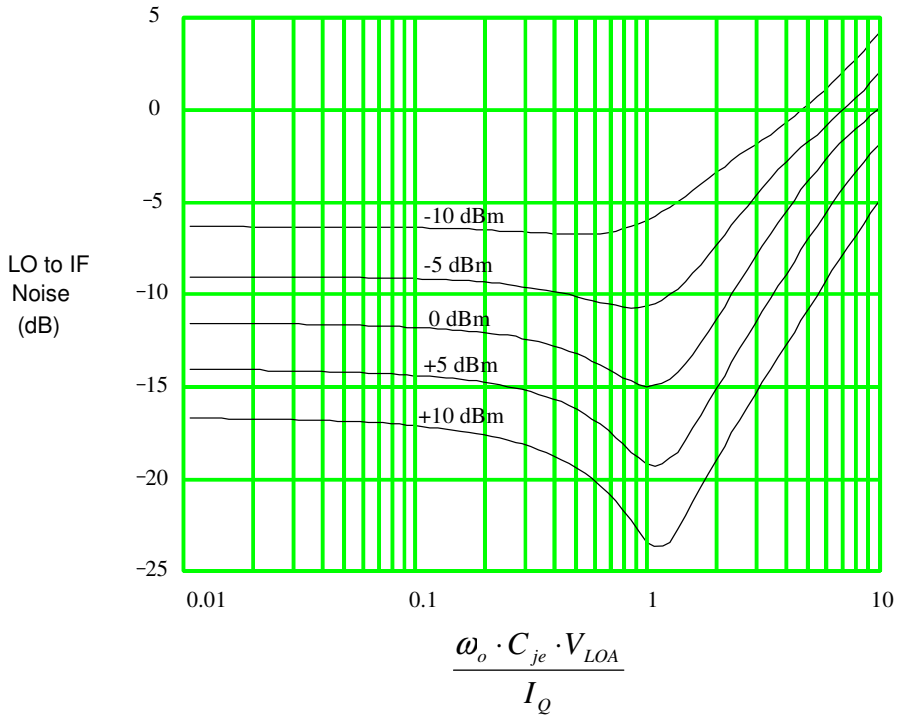

Figure 11b: Noise Rejection Factor (f_2) from LO to IF port vs. $\omega_o \cdot C_{jeo} \cdot V_{LOA} / I_Q$

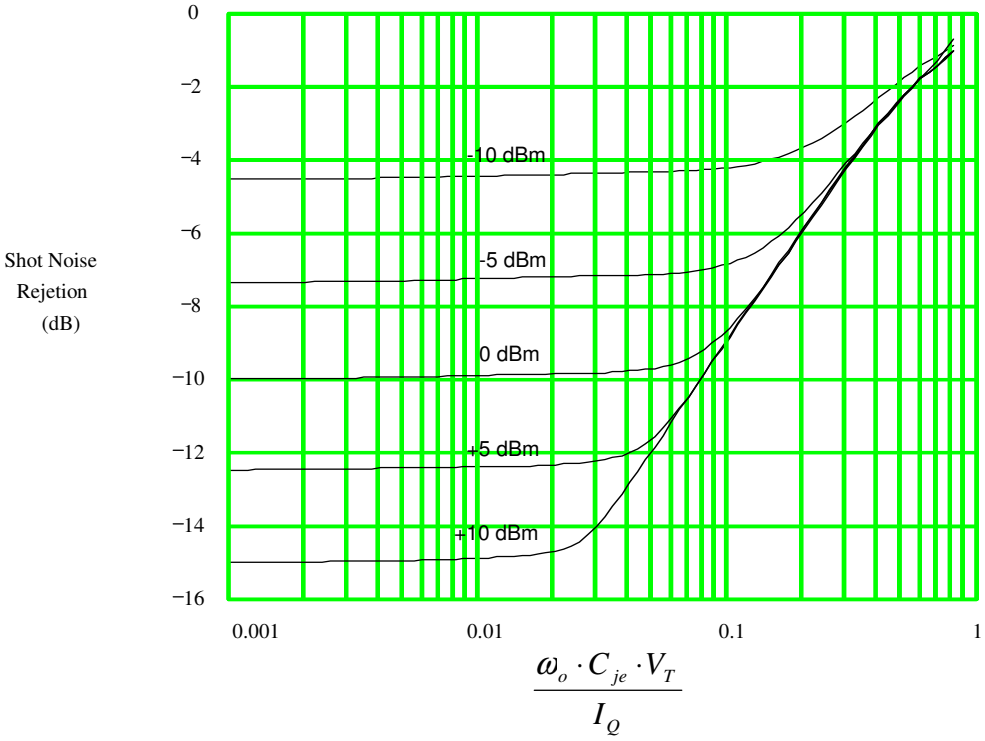

Figure 12a: Shot Noise Rejection Factor (f_1) vs. $\omega_o \cdot C_{je} \cdot V_T / I_Q$

The noise rejection from the LO port, f_2, is plotted as a function of $\omega_o \cdot C_{jeo} \cdot V_T / I_Q$ in Figure 11a. The noise rejection is also plotted against $\omega_o \cdot C_{jeo} \cdot V_{LOA} / I_Q$ in Figure 11b. Note that the output noise reaches a minimum near $\omega_o \cdot C_{jeo} \cdot V_{LOA} / I_Q = 1$ and then increases for $\omega_o \cdot C_{jeo} \cdot V_{LOA} / I_Q > 1$.

Shot noise rejection is plotted against $\omega_o \cdot C_{je} \cdot V_T / I_Q$ in Figure 12a. As $\omega_o \cdot C_{je} \cdot V_T / I_Q$ approaches unity, the output noise becomes independent of LO amplitude. To understand this consider that as $\omega_o \cdot C_{je} \cdot V_T / I_Q$ increases, the output noise during the non-transition times is increasing (see Figure 7, and associated discussion). Eventually most of the noise output is from the non-transition time noise mechanism. As this mechanism dominates, the output noise becomes independent of the transition time, and hence the LO power.

In Figure 12b, the shot noise rejection is plotted against $\omega_o \cdot C_{je} \cdot V_{LOA} / I_Q$. The shot noise is close to its low frequency value for $\omega_o \cdot C_{je} \cdot V_{LOA} / I_Q < 1$ and then increases at a rate of approximately 3dB/octave for $\omega_o \cdot C_{je} \cdot V_{LOA} / I_Q > 1$.

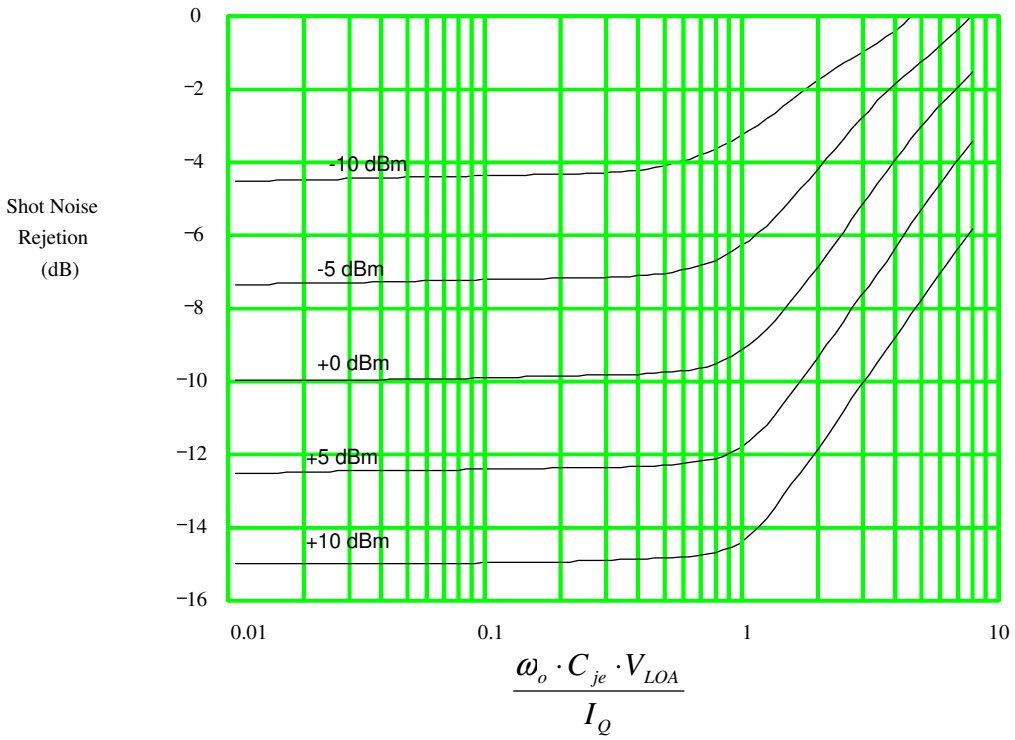

Figure 12b: Shot noise rejection Factor (f_1) vs. $\omega_o \cdot C_{je} \cdot V_{LOA} / I_Q$

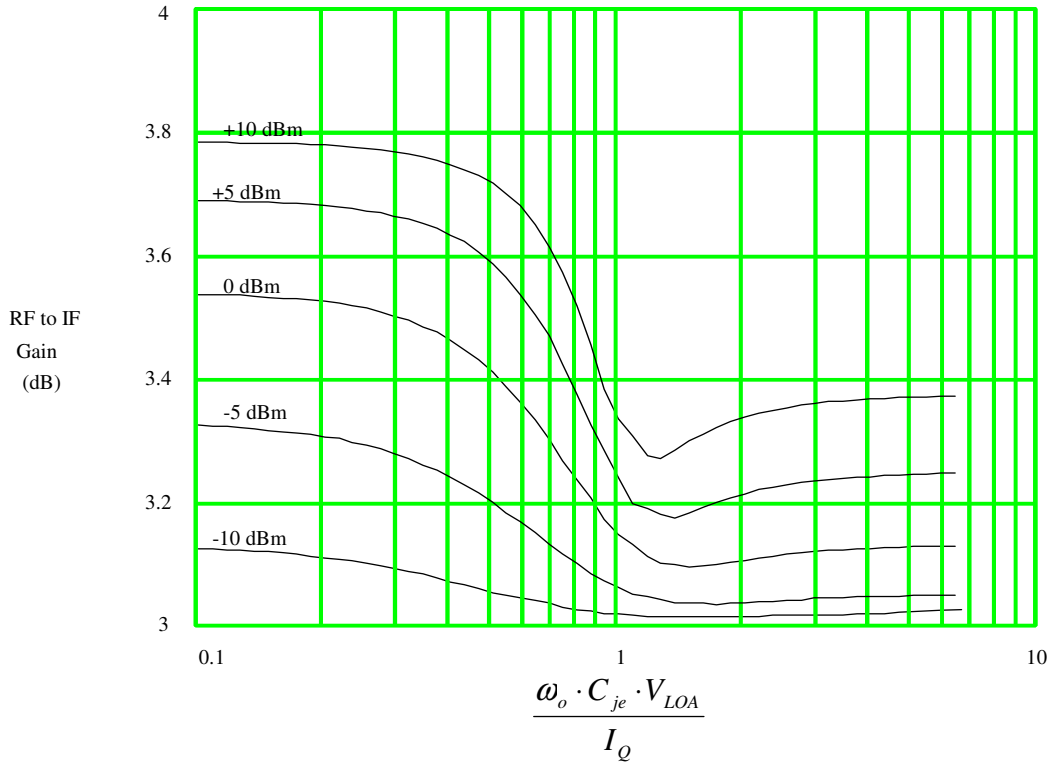

Figure 13: RF to IF white noise gain vs. $\omega_o \cdot C_{je} \cdot V_{LOA} / I_Q$

The gain of white noise incident at the RF port relative to the signal gain is plotted in Figure 13. As $\omega_o \cdot C_{je} \cdot V_{LOA} / I_Q$ increases the noise gain drops, reaching a minimum near $\omega_o \cdot C_{je} \cdot V_{LOA} / I_Q = 1$. The maximum variation is only on the order of 0.5 dB.

7.3: Intrinsic Noise Performance at Moderate Current Density

At moderate current densities both the non-transition time effects due to parasitic capacitances and the transition time effects due to parasitic resistances affect the output noise. Since the two effects are orthogonal, the change in output noise due to one effect may be added to the change in noise of the other.

A convenient way to calculate the output noise is to use Figures 8 and 9 as a starting point for noise calculations. These graphs take into account the effect of resistive parasitics. Then, the effect of

capacitive parasitics must be added. Plots of the change in the output noise components against $\omega_o \cdot C_{je} \cdot V_{LOA} / I_Q$ are shown in Figures 14 and 15.

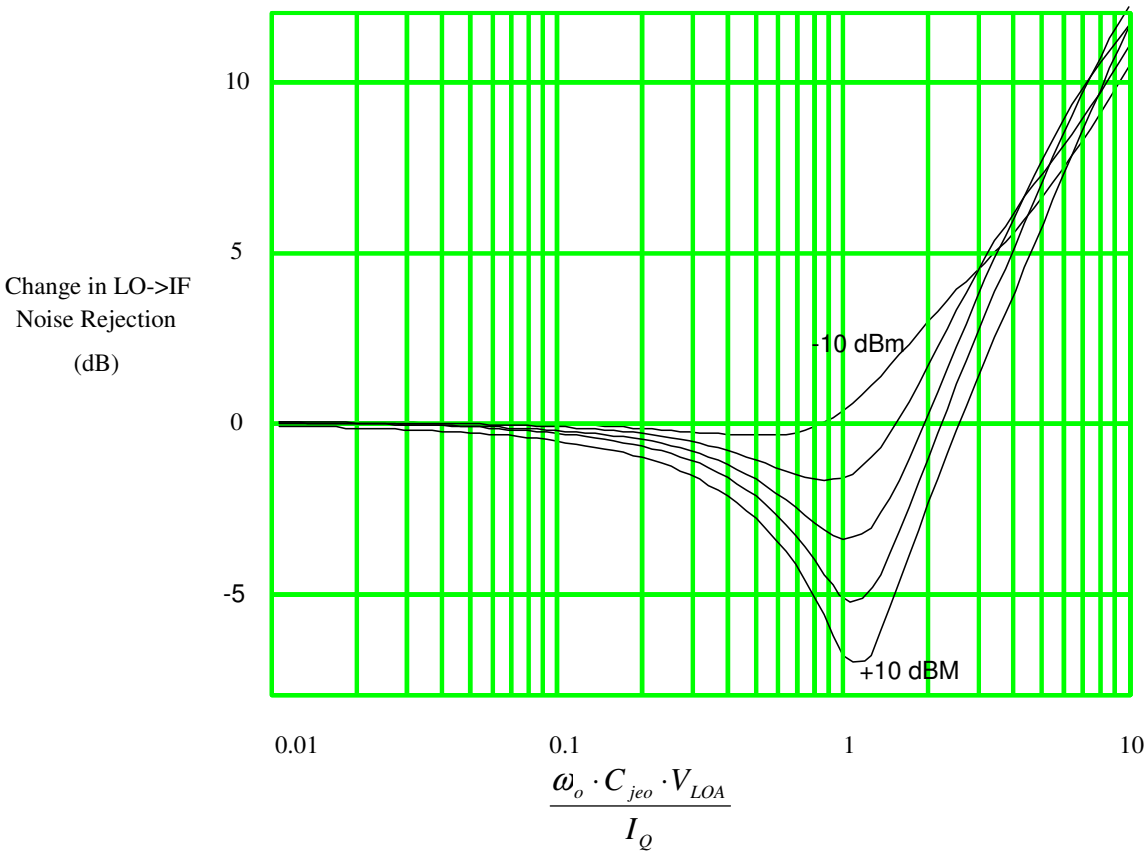

Figure 14: Relative Noise Rejection from LO to IF port vs. $\omega_o \cdot C_{je} \cdot V_{LOA} / I_Q$

In Figure 14 the change in the base-ohmic output noise component is plotted against $\omega_o \cdot C_{je} \cdot V_{LOA} / I_Q$. In Figure 15 the change in the shot noise component of the output noise is plotted against $\omega_o \cdot C_{je} \cdot V_{LOA} / I_Q$.

The total output noise rejection is calculated by first using Figures 8 and 9 to get the rejection values for each component, and then adding the values obtained from Figures 14 and 15.

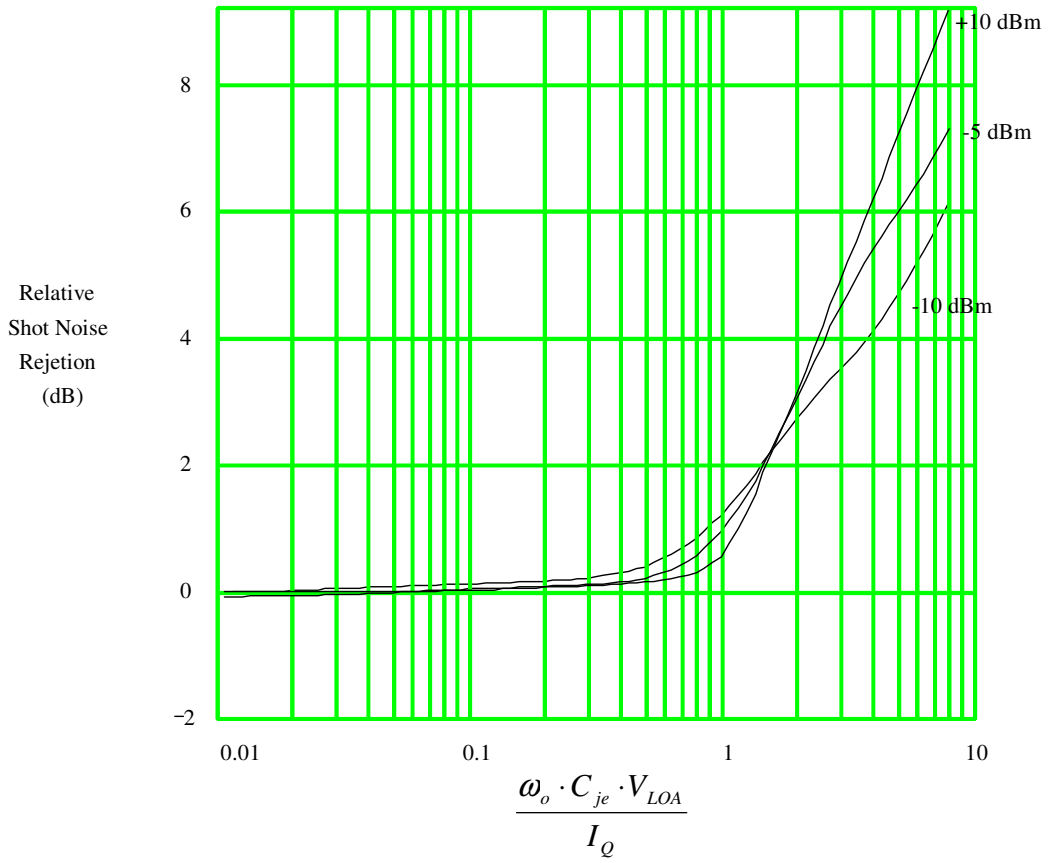

Figure 15: Relative shot noise rejection vs. $\omega_o \cdot C_{je} \cdot V_{LOA} / I_Q$

Using Equations 22a&b from Chapter 6, the output noise can be expressed in the form:

$$i_{odn}{}^2 \approx 2 \cdot q \cdot I_Q \cdot \Delta f \cdot \left[g_1\left[b, K, \frac{\omega}{\omega_x} \right] + \frac{r_b \cdot I_Q}{V_T} \cdot g_2\left[b, K, \frac{\omega}{\omega_x} \right] \right] \tag{12}$$

where:

$$\omega_x \equiv \frac{1}{\sqrt{r_b \cdot C_{je} \cdot \tau_f}}$$

$$K \equiv \frac{r_b \cdot I_Q}{V_T} \cdot \sqrt{\frac{\tau_f}{r_b \cdot C_{je}}}$$

As mentioned in Chapter 6, K is the *current-density factor.* And ω_x is a measure of the maximum possible frequency of operation for the mixer. The simulation results presented above are transformed into the form of Equation 12 in order to see how the noise performance varies with current densities.

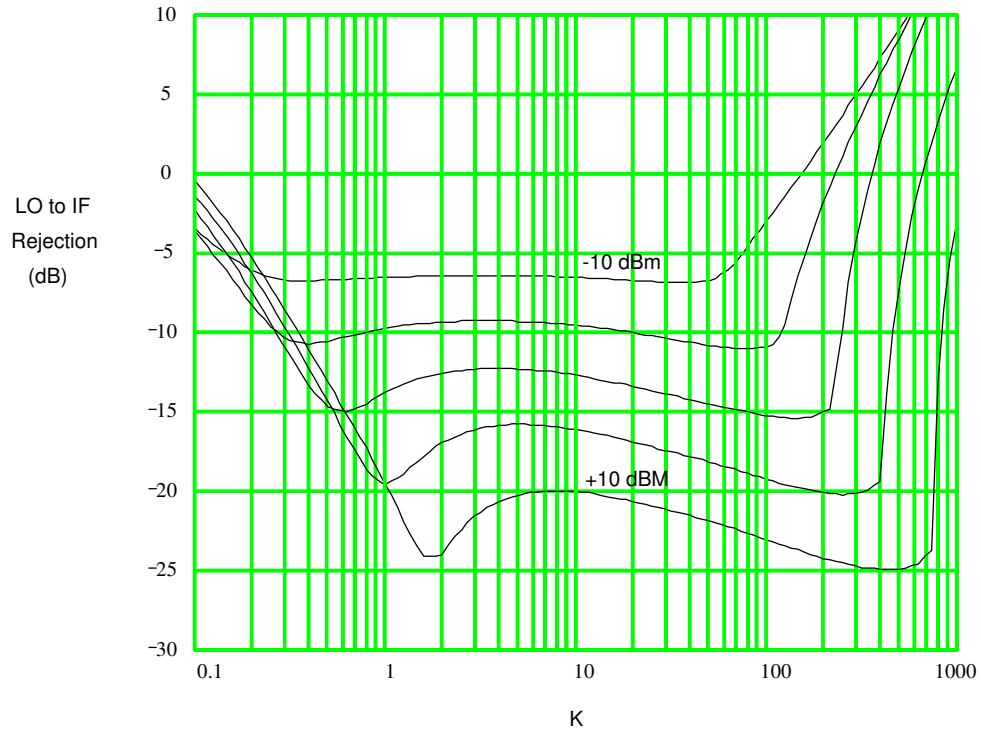

Figure 16a: Rejection of Noise from LO port vs. Current-density factor for $\omega/\omega_x = 0.05$

In Figures 16a,b,c the noise rejection from the LO port is plotted against the current-density factor for ω/ω_x =0.05, 0.1, and 0.2 respectively. Referring to Figure 16a, the noise rejection is relatively good over a wide range of current densities. In general, increasing the large LO amplitudes requires increasing the device current density. While two minima exist for noise rejection, the minimum output noise occurs at lower current densities, since the effect of r_b increases when the current-density factor is increased. Figures 16b and c are similar to Figure 16a, except that the range of current-density factors which give near optimal noise rejection is reduced.

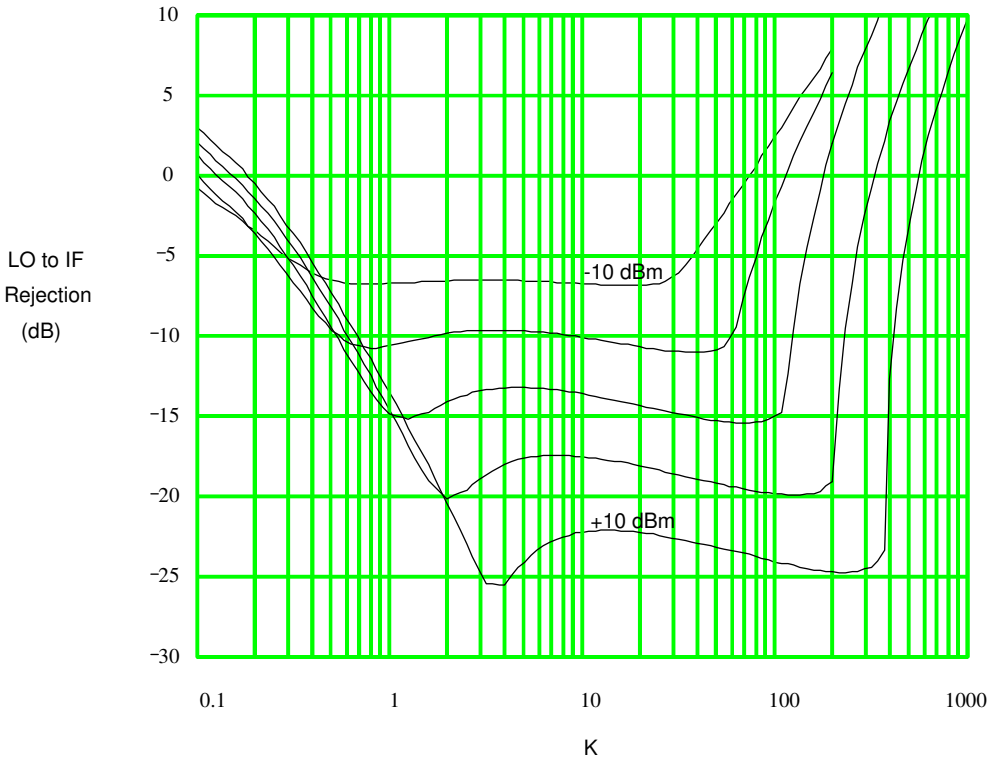

Figure 16b: Rejection of Noise from LO port vs. Current-density factor for $\omega/\omega_x = 0.1$

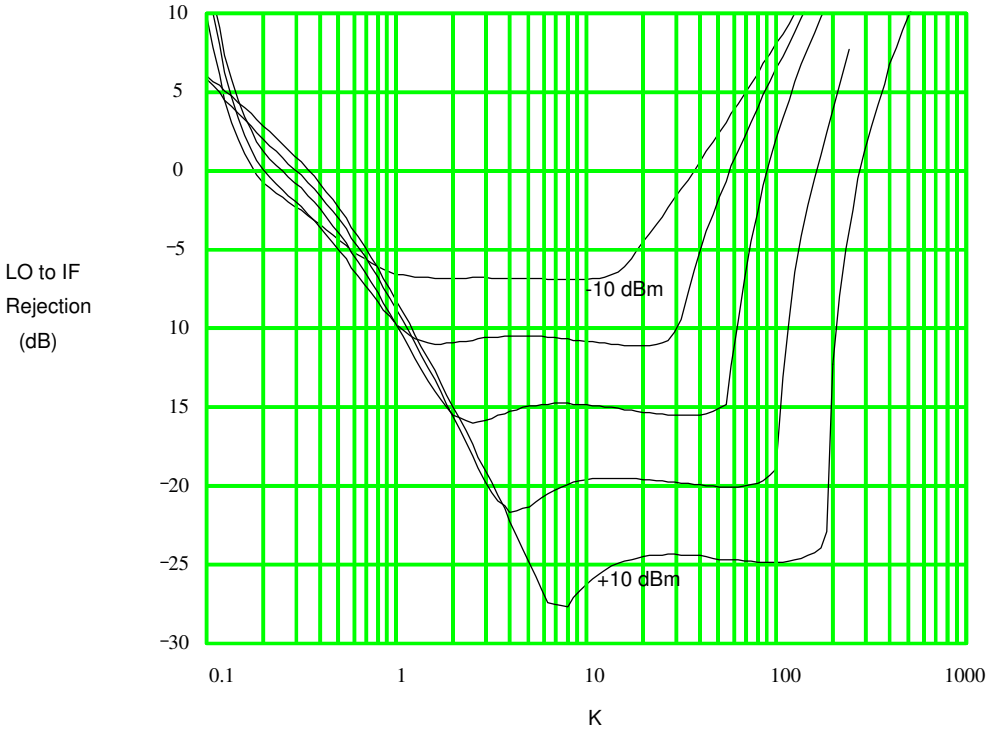

Figure 16c: Rejection of Noise from LO port vs. Current-density factor for $\omega/\omega_x = 0.2$

In Figures 17a,b,c the shot noise rejection is plotted against the current-density factor for ω/ω_x =0.05, 0.1, and 0.2 respectively. The shot noise rejection has a more parabolic-like dependency on the current-density factor. Optimum current-density factors (for minimum shot noise output) depend on the LO amplitude and the frequency of operations, but are generally in the range of 2-7.

Shot noise is especially important at low current density, where resistive parasitics tend to be relatively small (along with their associated thermal noise) in comparison to $1/g_m$.

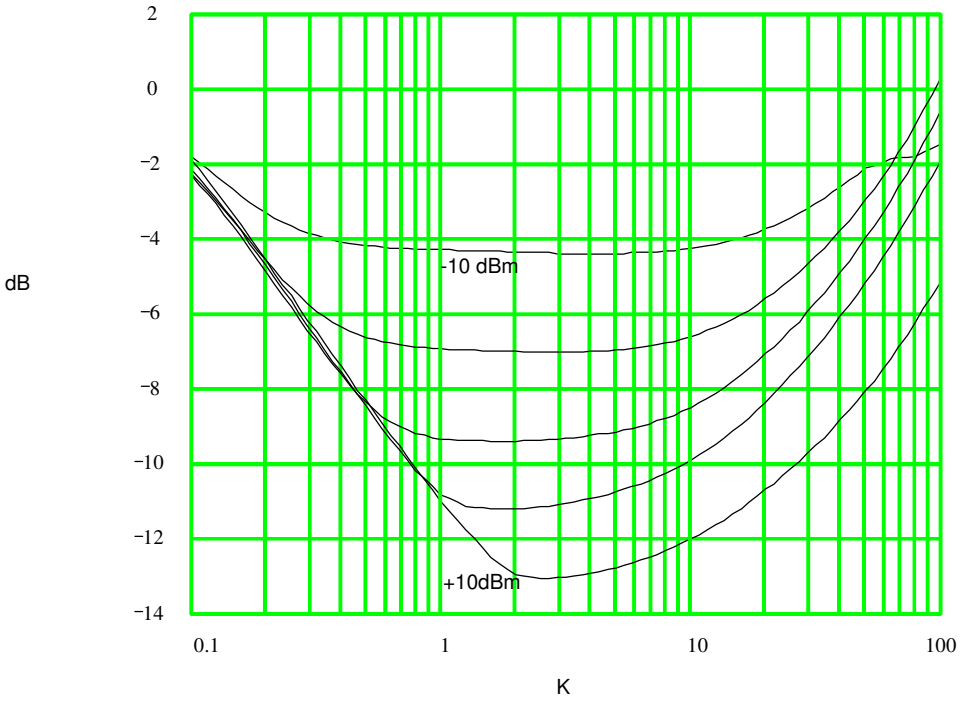

Figure 17a: Rejection of Shot Noise vs. Current-density factor for $\omega/\omega_x = 0.05$

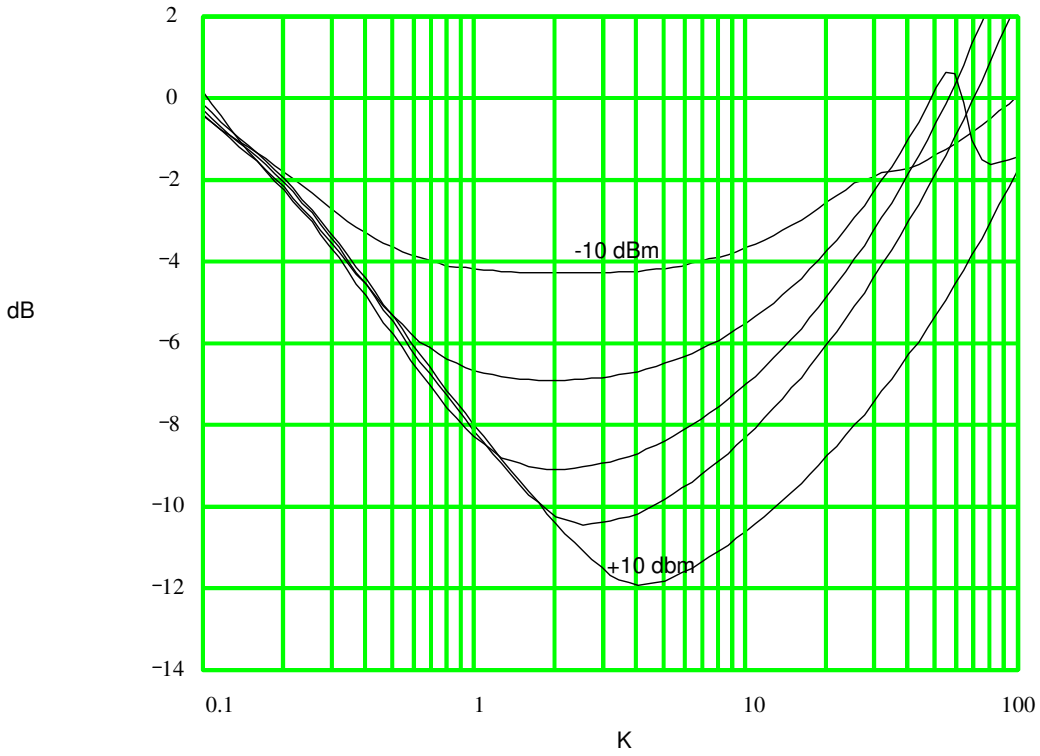

Figure 17b: Rejection of Shot Noise vs. Current-density factor for $\omega/\omega_x = 0.1$

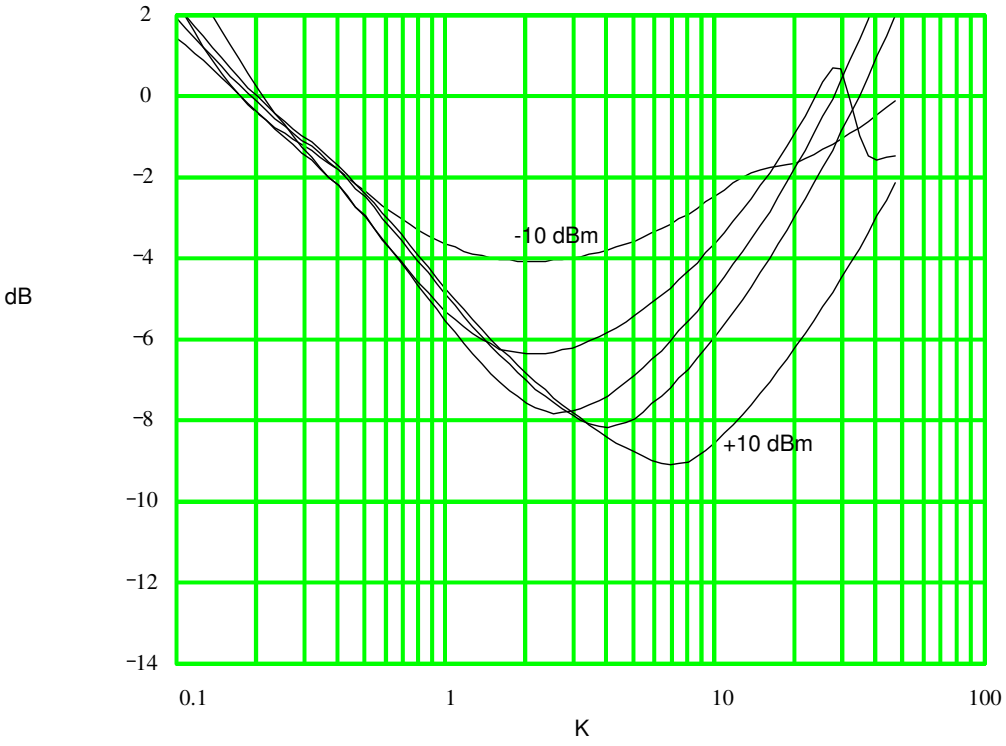

Figure 17c: Rejection of Shot Noise vs. Current-density factor for $\omega/\omega_x = 0.2$

In order to calculate the total output noise, it is necessary to make some assumptions about the particular process parameters. In particular if it is assumed that $\tau_f = r_b \cdot C_{je}$, Equation 10 simplifies to

$$i_{odn}{}^2 \approx 2 \cdot q \cdot I_Q \cdot \Delta f \cdot \left[g_1\left[b, K, \frac{\omega}{\omega_x} \right] + K \cdot g_2\left[b, K, \frac{\omega}{\omega_x} \right] \right] = 2 \cdot q \cdot I_Q \cdot \Delta f \cdot g_{tot}\left[b, K, \frac{\omega}{\omega_x} \right] \qquad (12)$$

where:

$$\omega_x = \frac{1}{\tau_f}$$

$$K = \frac{r_b \cdot I_Q}{V_T}$$

While this assumption is only approximately true for most bipolar processes, it simplifies the equations and allows insight into the noise performance optimization. For processes with $r_b \cdot C_{je} / \tau_f \neq 1$, a similar set of curves can be generated.

Figures 18a,b,c show the value of g_{tot} as a function of the current-density factor for ω / ω_x=0.05, 0.1, and 0.2. A value of unity for g_{tot} indicates that the output noise is equal to the shot noise of a device with a DC current of I_Q.

Referring to Figure 18a, the optimum current-density factor appears to depend on the LO power, with larger LO powers requiring higher current densities. The optimal noise performance is better for large LO amplitudes, improving by about 0.5dB per dB of increase in LO power.

Looking at Figure 18b, the general trends are the same at ω / ω_x=0.1 as they were for ω / ω_x=0.05, but the optimum noise rejection is about 1.5dB worse, and the optimum current density is about twice as high. At ω / ω_x=0.2 (Figure 18c), the optimum current density increases by another factor of two, and the optimum noise performance is 2.5dB worse.

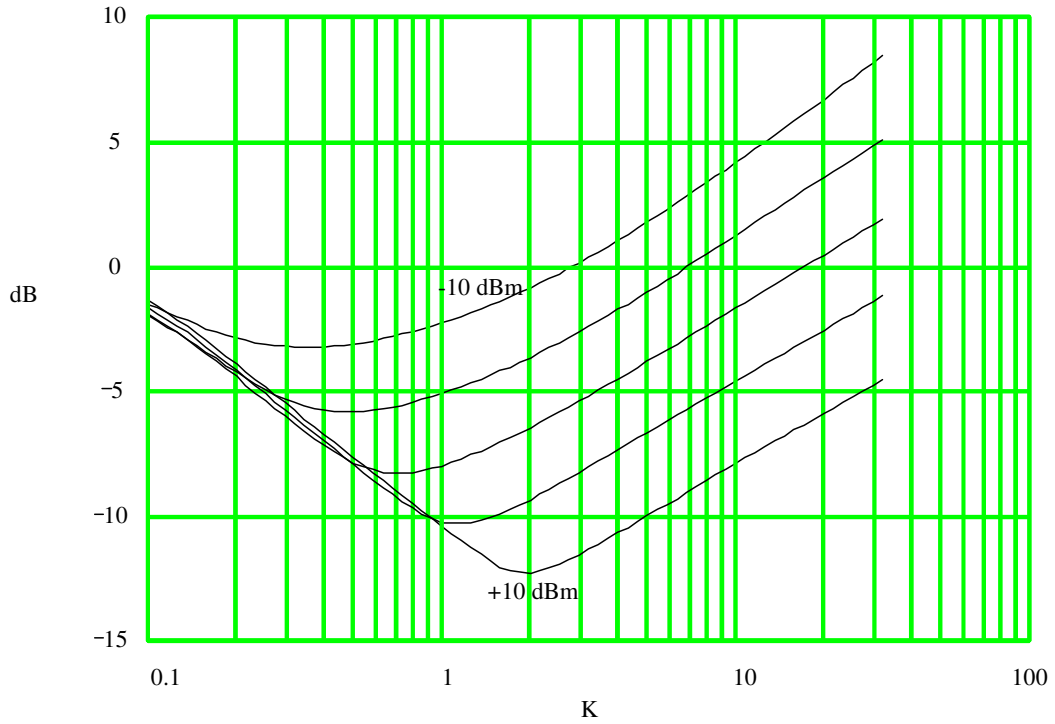

Figure 18a: Total Output Noise vs. Current-density factor for $\omega/\omega_x = 0.05$ and $\tau_f = r_b \cdot C_{je}$

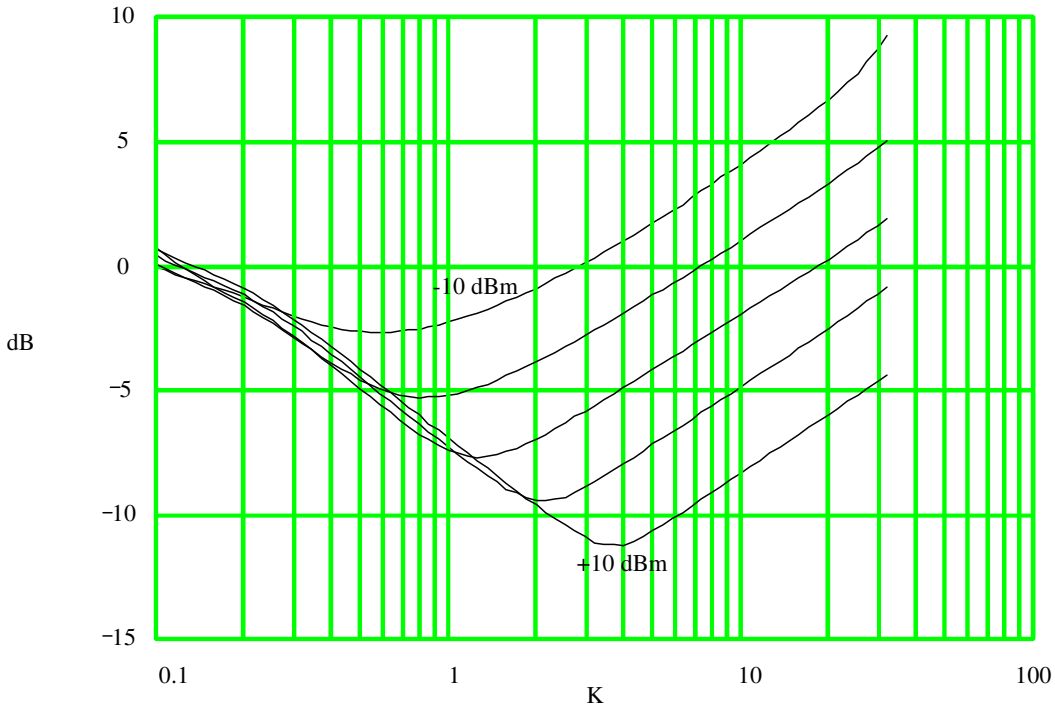

Figure 18b: Total Output Noise vs. Current-density factor for $\omega/\omega_x = 0.1$ and $\tau_f = r_b \cdot C_{je}$

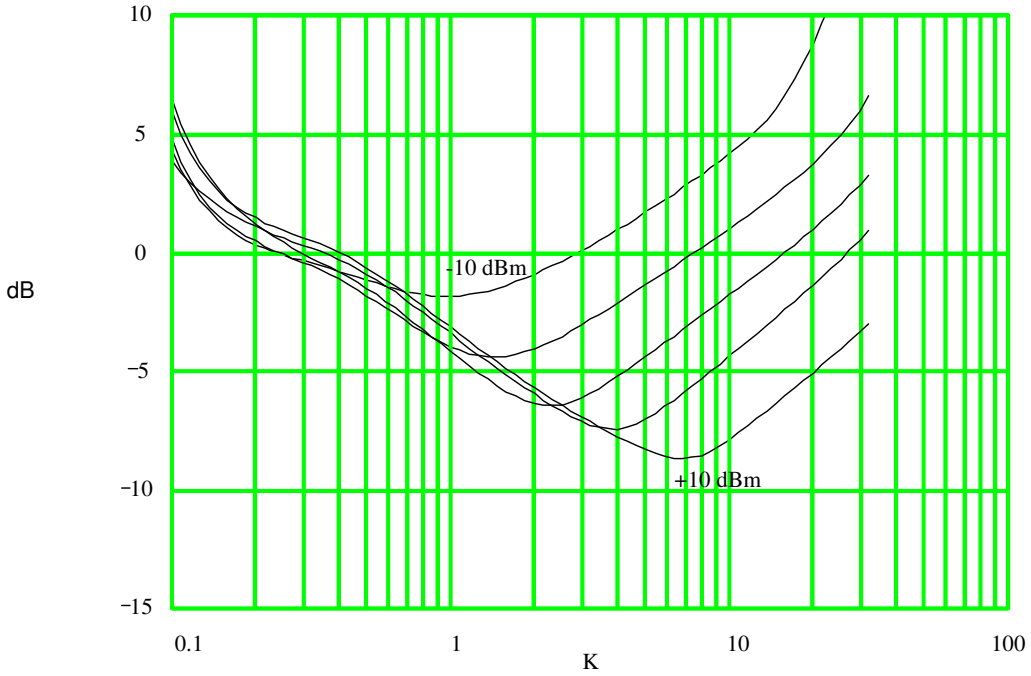

Figure 18c: Total Output Noise vs. Current-density factor for $\omega/\omega_x = 0.2$ and $\tau_f = r_b \cdot C_{je}$

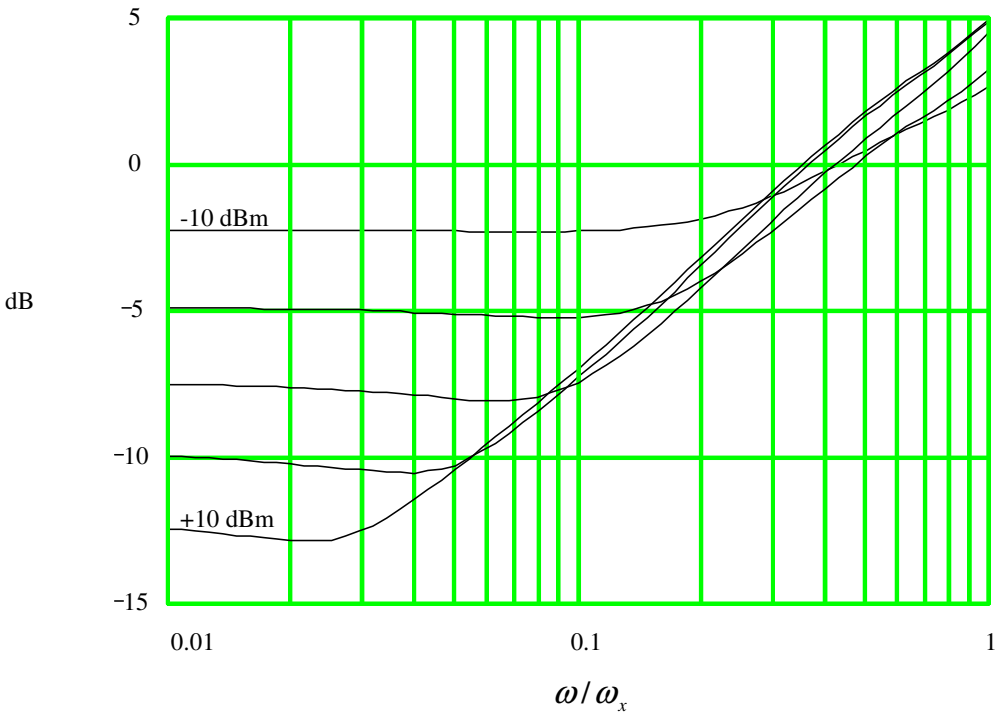

Figure 19a: Total Output Noise vs. Frequency for $K = 1$ and $\tau_f = r_b \cdot C_{je}$

In Figure 19a, the total output noise is plotted against frequency for a current-density factor of unity. At low frequencies this current-density factor gives excellent noise performance because of the small value of base-ohmic resistance. In addition, large LO power reduces the noise. However, as the frequency increases, the output noise begins to increase. At high frequencies the output noise becomes less sensitive to LO power.

The total output noise vs. frequency for K=3 is shown in Figure 19b. At low frequencies the output noise is 3-4 dB higher than for K=1. As the frequency increases, it becomes more desirable to use K=3, particularly for large LO amplitudes.

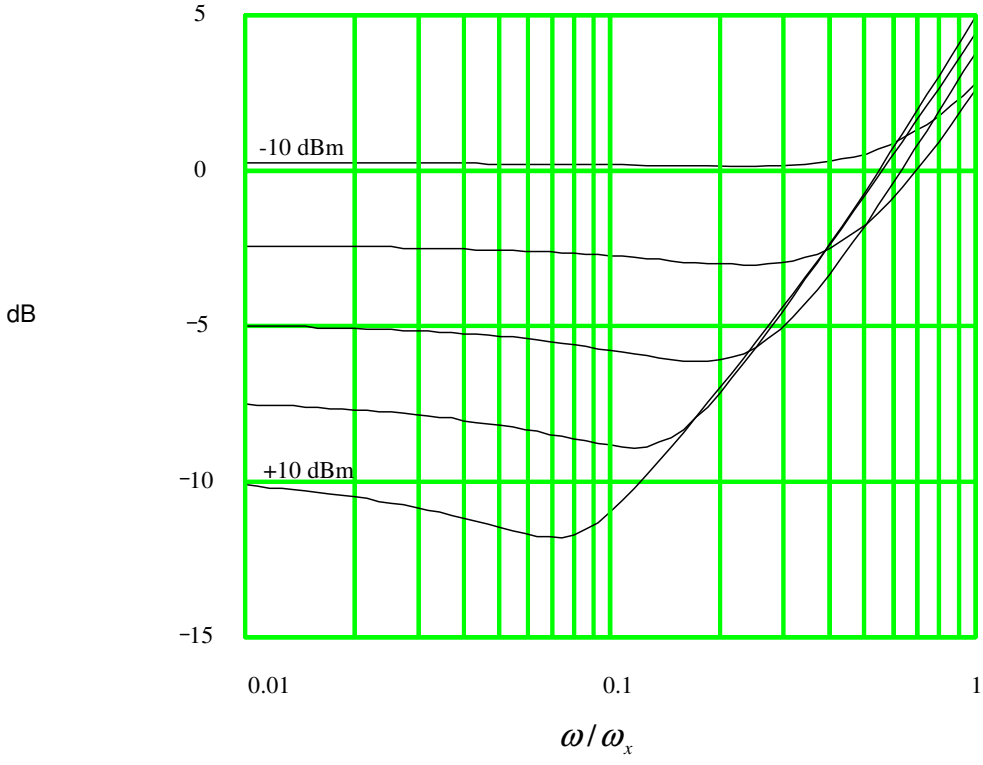

Figure 19b: Total Output Noise vs. Frequency for $K = 3$ and $\tau_f = r_b \cdot C_{je}$

In Figure 19c, the total output noise vs. frequency is plotted for a current-density factor of ten. For current densities this high, and at low frequencies, the noise performance is quite poor. At high frequencies

the noise performance shows a slight improvement for large LO amplitudes. Such a high current density might be appropriate if distortion is to be minimized (as is discussed in Chapters 8 and 9).

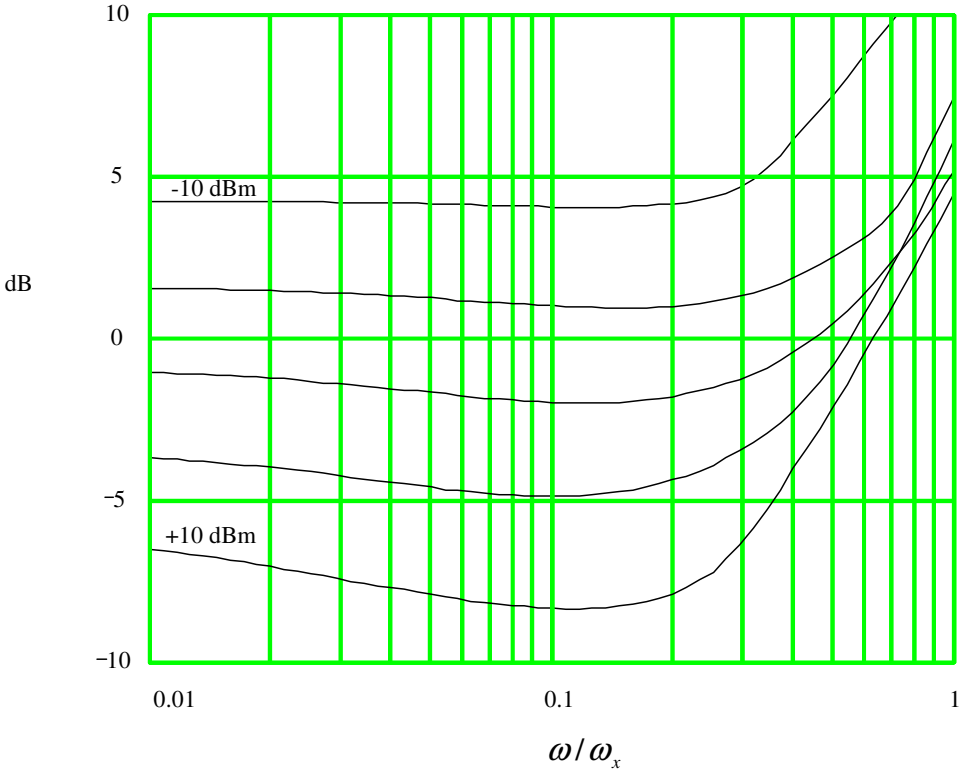

Figure 19c: Total Output Noise vs. Frequency for $K = 10$ and $\tau_f = r_b \cdot C_{je}$

Chapter 8: Intermodulation Distortion in the Emitter-Coupled Pair Mixer

As discussed in Chapter 6, the behavior of the emitter-coupled pair mixer is governed by three parameters:

$$\omega_o \cdot \tau_f \cdot r_b \cdot I_Q / V_T$$

$$\omega_o \cdot C_{je} \cdot V_T / I_Q$$

and

$$V_{LOA} / V_T$$

The first two of these parameters do not interact substantially so long as:

$$\omega_o \cdot \tau_f < 0.25$$

and

$$\omega_o \cdot r_b \cdot C_{je} < 0.25$$

As with amplifiers, simulations indicate that the 3rd order intermodulation distortion varies quadratically with input signal level. Thus it is possible to calculate a 3rd order intercept point with mixers as well as amplifiers.

8.1: Intermodulation Distortion at Low Current Density

At low current densities, the transition time (the time when both devices are on) is very short. The dominant distortion mechanism is due to C_{je} of the on device. However, C_{je} of the **off** device may have a substantial effect on distortion because of the "tilting" of the collector current waveform (see Figures 5a,b,c in Chapter 6).

In the absence of any waveform "tilting" ($\omega_o \cdot C_{je} \cdot V_{LOA} / I_Q << 1$), during non-transition times the switch appears to be a common-base amplifier (See Figure 1). Thus, the formula for intermodulation distortion in the common-base driver (Equation 4 of Chapter 4) can be used to approximate the distortion in the emitter-coupled pair mixer. Assuming the output impedance of the driver is large compared to r_b and $1/g_m$, the distortion in the mixer at low current density can be approximated by:

$$DIM_3(\omega_o) \approx \frac{1}{2} \cdot \frac{\omega_o \cdot C_{je} \cdot V_T}{I_Q} \cdot \left[\frac{i_{sa}}{I_Q} \right]^2 \qquad (1a)$$

The distortion is twice as large as an equivalent common-base amplifier, since the parasitic C_{je} of the off device adds to the distortion. If there are additional capacitive parasitics at the emitter of Q_1 and Q_2, the distortion will be:

$$DIM_3(\omega_o) \approx \frac{1}{4} \cdot \frac{\omega_o \cdot (2 \cdot C_{je} + C_x) \cdot V_T}{I_Q} \cdot \left[\frac{i_{sa}}{I_Q} \right]^2 \tag{1b}$$

where C_x is the parasitic capacitance. In particular C_{cs} and C_{jc} of the driver will add to C_{je} of the ECP switch.

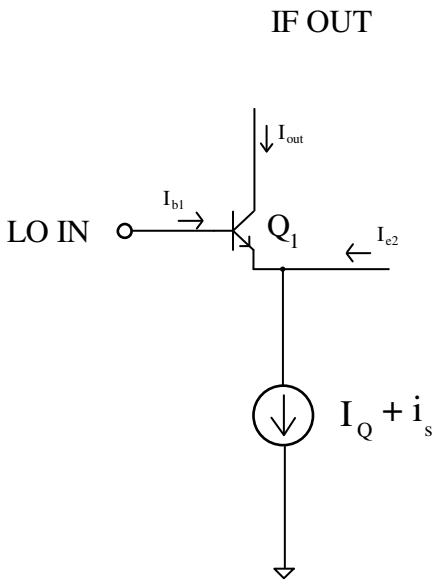

Figure 1: ECP Mixer during non-transition time (Q_2 is off)

The effect of waveform "tilting" on distortion is investigated by doing SPICE transient simulations. The output is put through a Fourier transform to determine the frequency spectrum. For simulations the frequencies chosen were 1.0GHz for the LO and 1.05 and 1.07 GHz for the RF signals. The desired output frequencies are 50 and 70 MHz. Distortion is produced at 30 and 90MHz. The simulation is run for 100ns in order to resolve frequency differences of 10MHz. It is necessary to allow sufficient time for transients to settle before collecting the 100ns of data. A total of 16,384 data points are taken at intervals

of about 6ps. This is sufficient to prevent significant aliasing. Aliasing is further reduced by a single pole IF filter at 700MHz.

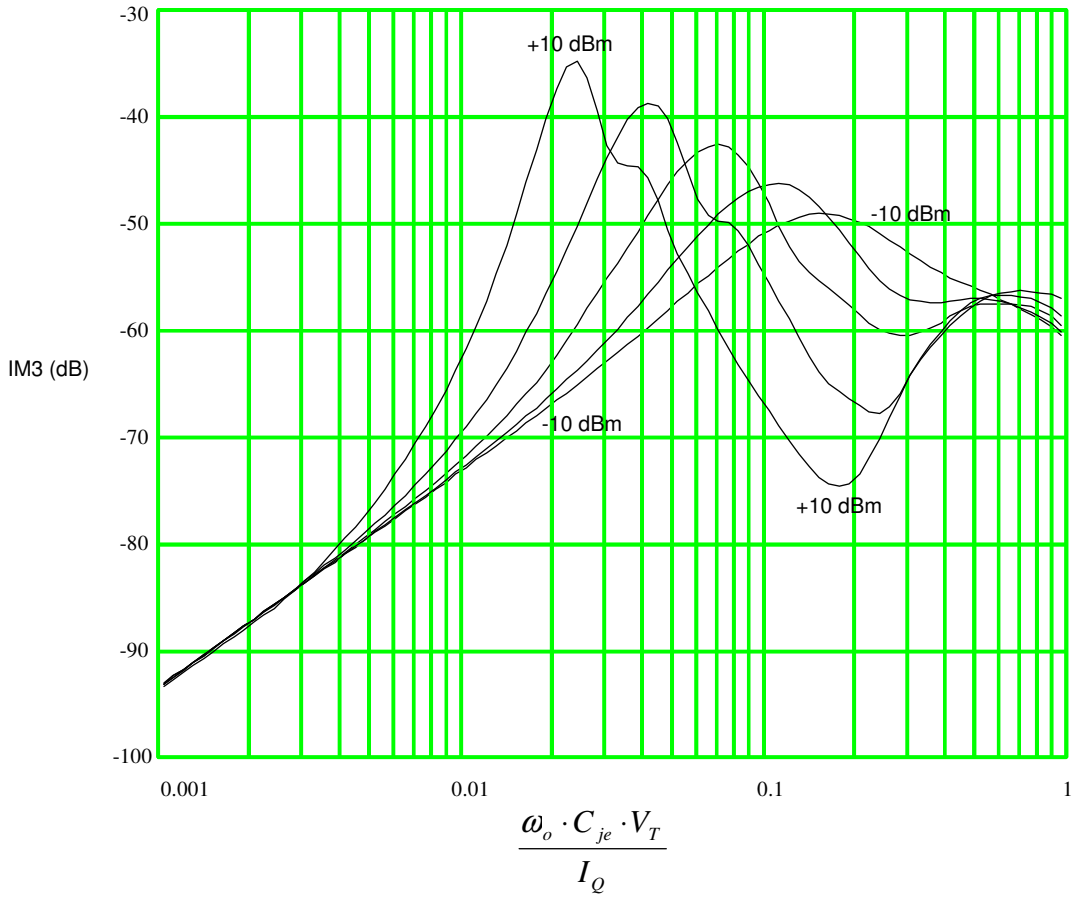

Figure 2: IM3 vs. $\omega_o \cdot C_{je} \cdot V_T / I_Q$ for $P_{LO} = -10,-5,0,+5,+10\text{dBm}$, $r_b = \tau_f = 0$, $i_{sa} / I_Q = 0.2$

For simulations purposes the modulation is set to 20%. That is $i_{sa} = 0.2 \cdot I_Q$. Large values of modulation lead to significant contributions from higher order distortion mechanisms. Reducing the modulation leads to numerical noise problems. Simulations were run at 10% and 40% modulation to check the proposed quadratic relationship between distortion and signal modulation (Equation 1). Because of higher order terms, there was significant deviation from the quadratic relationship at 40% modulation. At 20% modulation, the distortion was 12-13 dB higher than at 10% modulation, indicating that the quadratic relationship between distortion and modulation holds to within 1 dB for modulations up to 20% .

The extrapolated distortion at 100% modulation is 28dB higher than the distortion at 20% modulation. The intercept point as a current is then equal to :

$$IP_3 = \frac{I_Q}{\sqrt{DIM_3(100\%)}} \tag{2}$$

The intermodulation distortion vs. $\omega_o \cdot C_{je} \cdot V_T / I_Q$ with $r_b = \tau_f = 0$ is plotted for five different LO amplitudes in Figure 2. The LO amplitudes were 100mV, 178mV, 316mV, 562mV, and 1V, which correspond to LO powers of -10,-5,0,+5, and +10 dBm for a 50Ω system. For $\omega_o \cdot C_{je} \cdot V_T / I_Q < 0.003$, the distortion is independent of LO amplitude and is given by Equation 1. As $\omega_o \cdot C_{je} \cdot V_T / I_Q$ increases, the distortion becomes strongly dependent on the LO power.

In Figure 3 the ratio of the actual mixer distortion to the distortion predicted by Equation 1 is plotted. For $\omega_o \cdot C_{je} \cdot V_{LOA} / I_Q < 0.1$, Equation 1 appears to give an adequate approximation. As $\omega_o \cdot C_{je} \cdot V_{LOA} / I_Q$ is increased, the distortion begins to become substantially larger than predicted by Equation 1, especially for large LO amplitudes. The distortion peaks near $\omega_o \cdot C_{je} \cdot V_{LOA} / I_Q = 1$, and then drops rapidly. The mechanism that causes this variation from simple theory is the "tilting" of the collector current waveform. The additional current pumped into the common-emitter point from the C_{je} of the off device has a substantial effect on distortion.

$$I_{e2} = I_{b2} \approx C_{je} \cdot dV_{LO} / dt = -\omega_o \cdot C_{je} \cdot V_{LOA} \cdot \cos(\omega_o \cdot t) \tag{3}$$

From Figure 2 it appears that a distortion null can be achieved at high frequencies by using a large device and a large LO amplitude. This approach has a number of practical problems. First, parameter variations over temperature and supply make it impossible to achieve a controlled value of $\omega_o \cdot C_{je} \cdot V_T / I_Q$. In addition, very large amounts of reactive current flow into the base of the "off" device (See Equation 3).

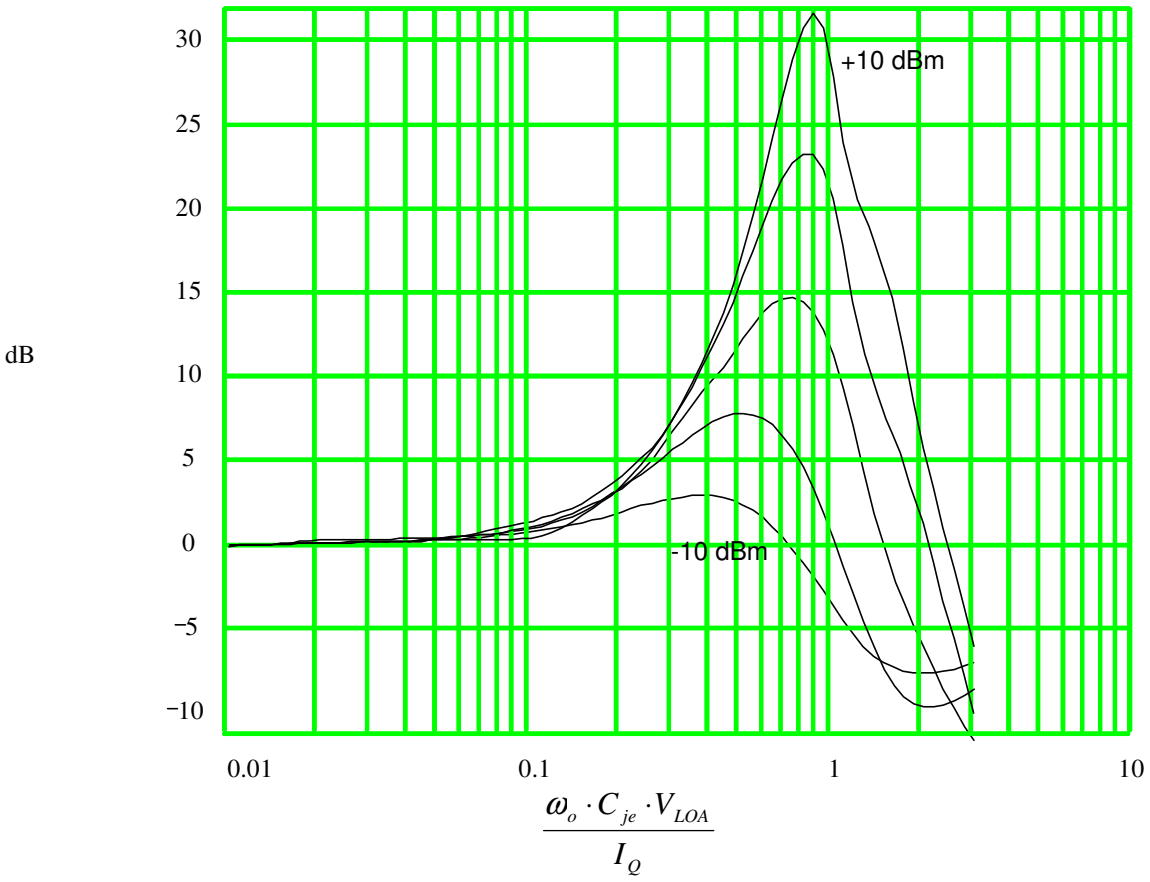

Figure 3: Excess Distortion due to waveform "tilting" vs. $\omega_o \cdot C_{je} \cdot V_{LOA} / I_Q$ for

$$P_{LO} = -10,-5,0,+5,+10\text{dBm}$$

8.2: Intermodulation Distortion at High Current Density

At high current densities, the transition time (the time when both devices are on) is increased significantly, but no significant "tilting" exists. Ideally, no distortion would occur during transition periods if the ideal exponential law of the transistor holds[xiii]. However, the parasitic base resistance adds a linear term to the exponential voltage-to-current relationship. Therefore distortion is generated. At low frequencies ($\omega_o << \omega_T$) the high current gain makes the voltage drop across r_b negligible. As the LO frequency increases the base current and voltage drop across r_b increase. The voltage drop is proportional to $\omega_o \cdot \tau_f \cdot r_b \cdot I_Q / V_T$, and thus it is expected that the distortion will increase as this parameter increases.

Simulated values of intermodulation distortion at 20% modulation vs. $\omega_o \cdot \tau_f \cdot r_b \cdot I_Q / V_T$ for LO power of -10,-5,0,+5,+10 dBm are shown in Figure 4. The distortion increases monotonically with frequency until it reaches 1% (-40 dB). The distortion generally decreases with LO power, though for very small values of $\omega_o \cdot \tau_f \cdot r_b \cdot I_Q / V_T$, the distortion actually increases with LO power. Intuitively one expects decreasing distortion with increasing LO power since the transition time is reduced. It is unclear why this does not universally hold true.

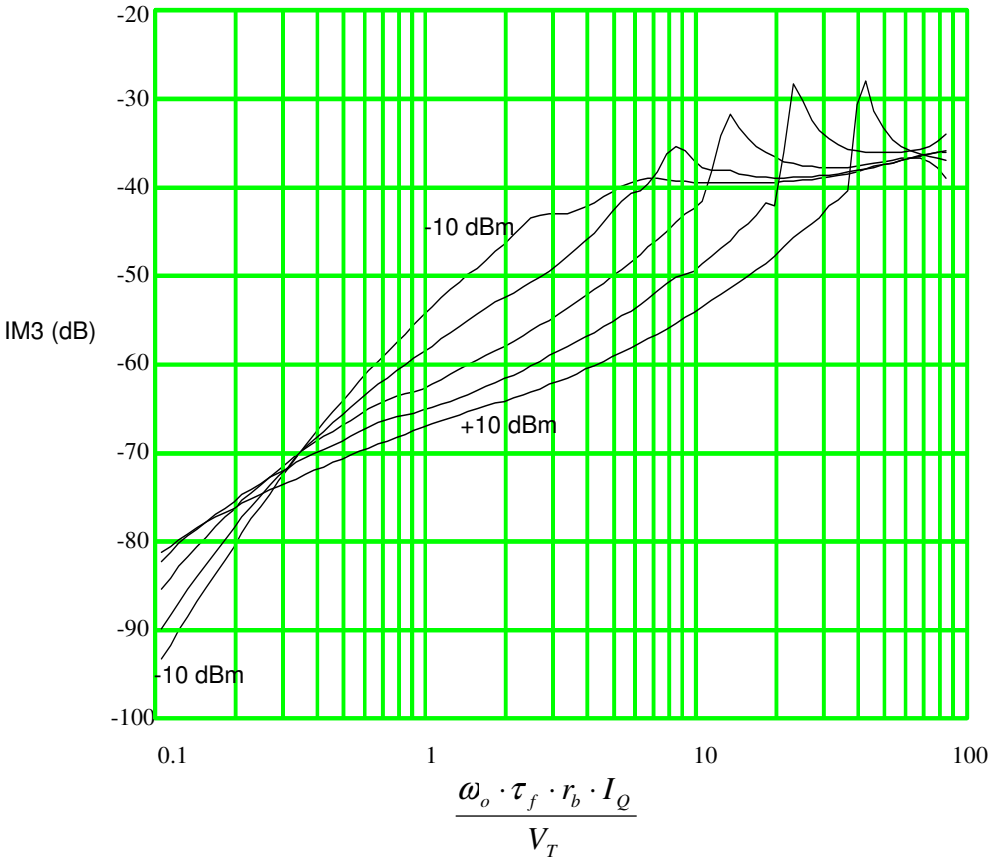

Figure 4: IM3 vs. $\omega_o \cdot \tau_f \cdot r_b \cdot I_Q / V_T$ for $P_{LO} = -10,-5,0,+5,+10\text{dBm}, C_{je} = 0, i_s / I_Q = 0.2$

In Figure 5, the distortion is plotted against the parameter $\omega_o \cdot \tau_f \cdot r_b \cdot I_Q / V_{LOA}$ for LO power levels of -10,-5 and +10 dBm. For $0.1 < \omega_o \cdot \tau_f \cdot r_b \cdot I_Q / V_{LOA} < 1$ the distortion is primarily dependent on this single parameter. This is not surprising, since the transition time is governed by this parameter. The

spike near $\omega_o \cdot \tau_f \cdot r_b \cdot I_Q / V_{LOA} = 1$ is at the bandedge of the mixer. For $\omega_o \cdot \tau_f \cdot r_b \cdot I_Q / V_{LOA} > 1$ the conversion gain drop rapidly (see Figure 4 of Chapter 6).

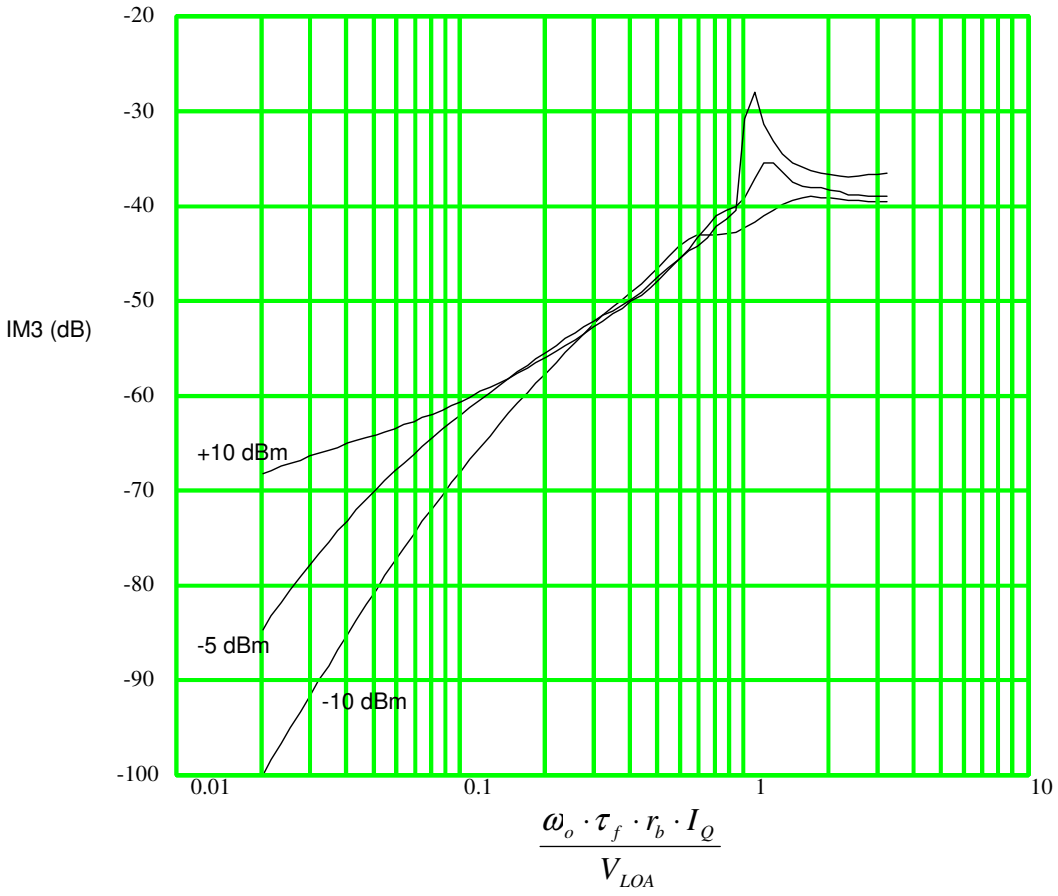

Figure 5: IM3 vs. $\omega_o \cdot \tau_f \cdot r_b \cdot I_q / V_{LOA}$ for $P_{LO} = -10,-5,+10\text{dBm}, C_{je} = 0, i_s / I_Q = 0.2$

8.3: Effect of Non-linear Base-Emitter Junction Capacitance

Previous results for distortion at low current densities were obtained by assuming a constant value of C_{je}. In reality, C_{je} is a non-linear capacitance. The model for a non-linear capacitor is given by:

$$C_{je} = \frac{C_{jeo}}{\left[1 - \frac{V_{be}}{V_{je}}\right]^{M_{je}}} \tag{4}$$

This formula holds for $V_{be} < F_c \cdot V_{je}$ where $F_c < 1$. The default value used by SPICE is $F_c = 0.5$, which does not accurately model a real base-emitter junction. Using the SPICE default value gives simulation results that are almost identical to those that use a constant value model for C_{je}. Results of device characterization show that a more reasonable value is $F_c = 0.85$. Since the C_{je} is dominant at low current densities, it is assumed that $V_{be(\max)} < F_c \cdot V_{je}$ so that Equation 4 holds at all times.

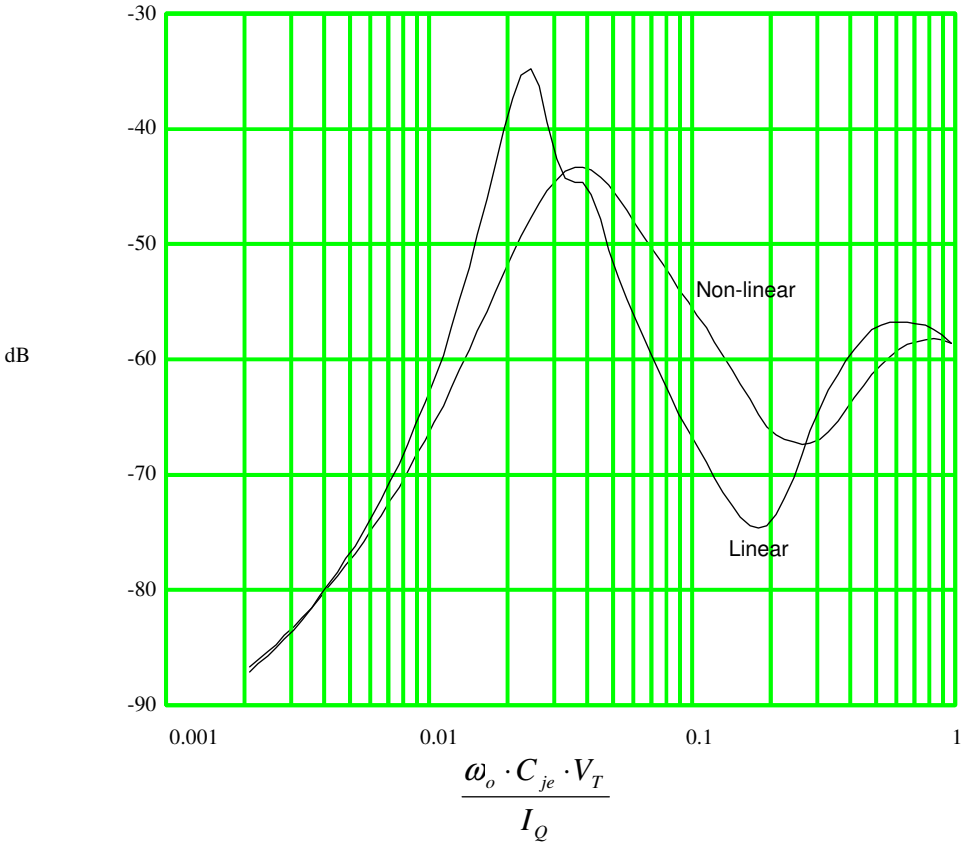

Figure 6: Distortion For Linear and Non-linear C_{je} vs. $\omega_o \cdot C_{je} \cdot V_{LOA} / I_Q$. $P_{LO} = +10\text{dBM}$, $r_b = 0$

The value of M_{je} is determined by the grading of the junction. For an abrupt junction $M_{je} = 0.5$ and for a linearly graded junction $M_{je} = 0.33$.[xiv] To simplify the investigation of the non-linear effects $M_{je} = 0.41$ is used in simulations. This represents a value midway between a linear junction and an abrupt junction.

Simulation results indicate significant changes in the distortion values when a non-linear model for C_{je} is used. The changes are most dramatic for large LO amplitudes. In Figure 6, the distortion for the linear and non-linear model of C_{je} are compared for an LO amplitude of 1 Volt (+10 dBm). At lower frequencies there is little difference so long as the value chosen for the linear model of C_{je} is equal to the actual value of C_{je} when the device is "on" (I_Q is flowing into the emitter of the device). As the frequency is increased, the predicted distortion in the non-linear model shows significant variation from that predicted by the linear model. In general the peaks and dips are "softened".

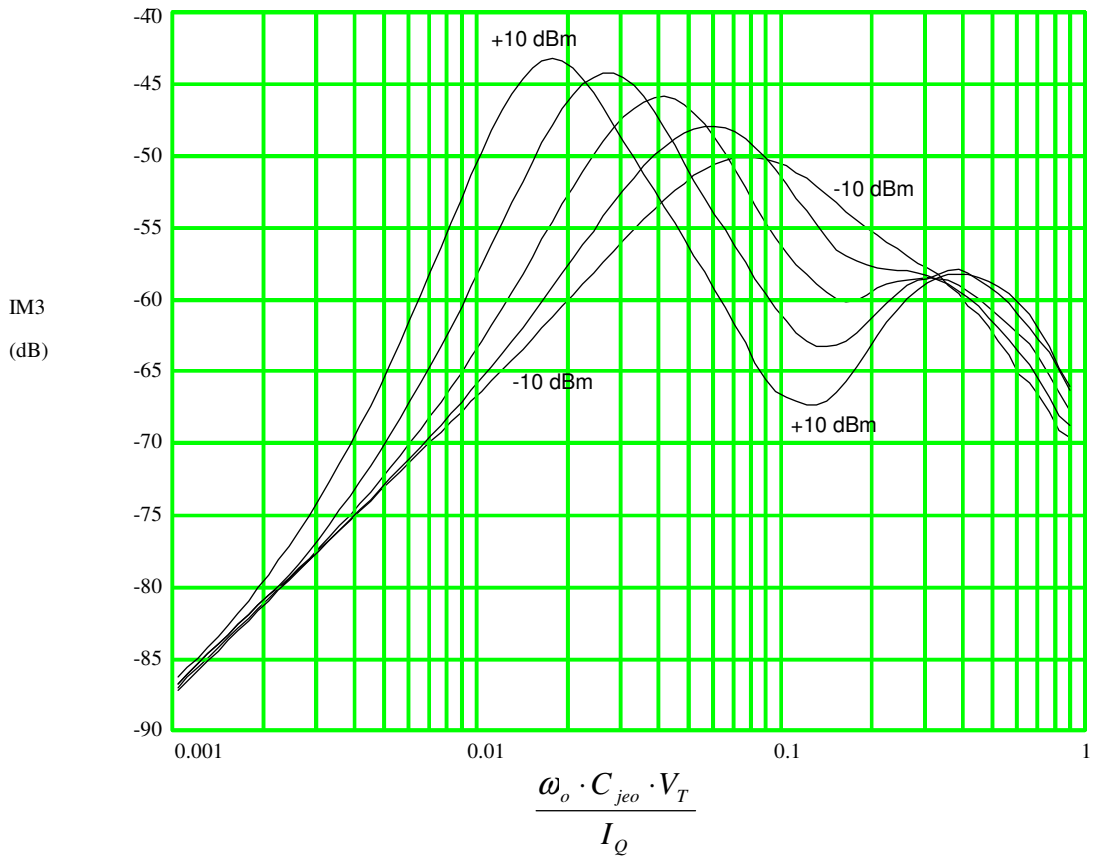

Figure 7: Distortion vs. $\omega_o \cdot C_{jeo} \cdot V_T / I_Q$ using nonlinear model for C_{je}

In Figure 7, the distortion using the nonlinear C_{je} model is plotted against $\omega_o \cdot C_{jeo} \cdot V_T / I_Q$ for LO power of -10,-5,0,+5, and +10 dBm (into 50 ohms). A comparison of Figure 7 and Figure 2 shows that the nonlinear model seems to decrease the maximum distortion and increase the minimum distortion.

8.4: Other Second Order Effects:

Referring to Equation 16 of Chapter 6, for low current densities the state equation is:

$$\frac{dI_{c1}'}{dt'} = \frac{1 + i_s' - I_{c1}' \cdot (1 + e^{-b \cdot \sin(t')})}{2 \cdot \left[\omega_o \cdot \tau_f + \frac{\omega_o \cdot C_{je} \cdot V_T}{I_Q} \cdot \frac{1}{I_{c1}'} \right]} \tag{5}$$

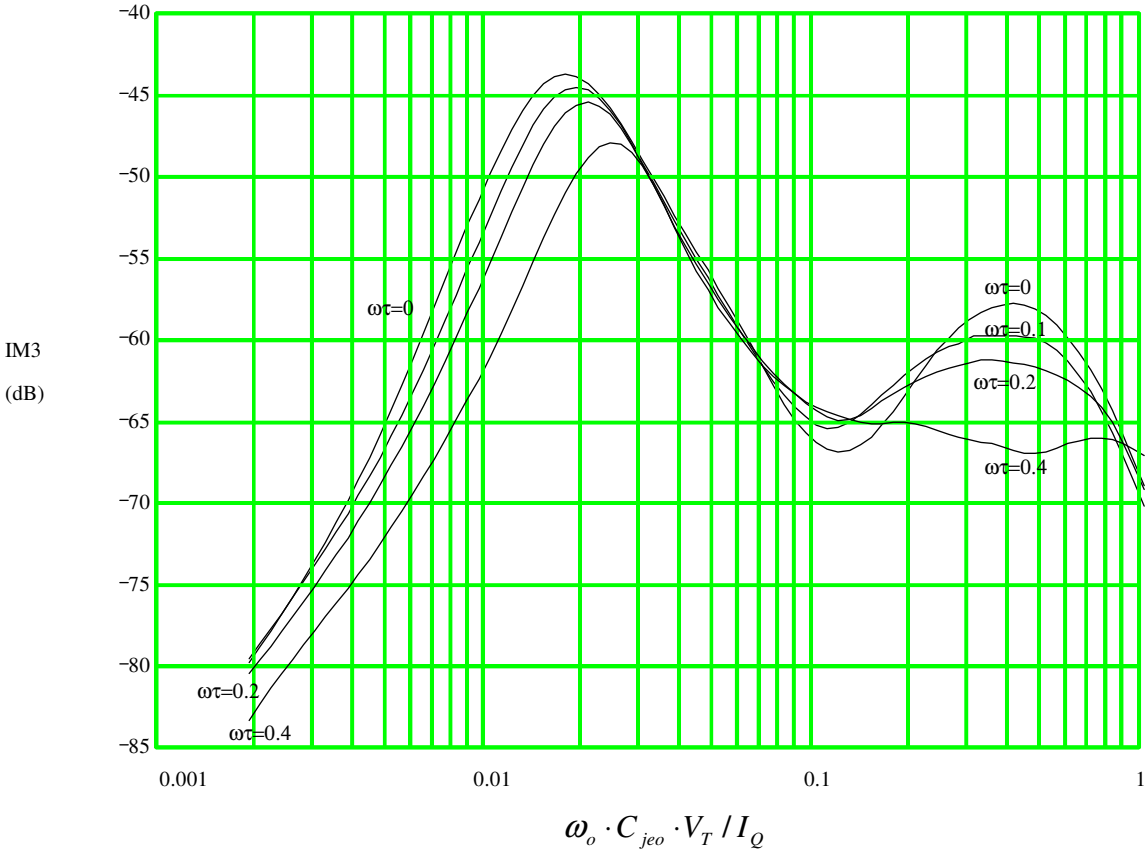

Figure 8: Intermodulation Distortion vs. $\omega_o \cdot C_{jeo} \cdot V_T / I_Q$ for $\omega_o \cdot \tau_f = 0, 0.1, 0.2, 0.4$

Notice that the solution is not only a function of $\omega_o \cdot C_{je} \cdot V_T / I_Q$, but also $\omega_o \cdot \tau_f$. As mentioned in Chapter 6, if $\omega_o \cdot \tau_f << 1$ the collector current shows little dependence on $\omega_o \cdot \tau_f$ (when $r_b = 0$). To

confirm that the distortion is independent of $\omega_o \cdot \tau_f$ (when $r_b = 0$), simulations were run for a range of values of $\omega_o \cdot C_{je} \cdot V_T / I_Q$ with $\omega_o \cdot \tau_f = 0,0.1,0.2,0.4$. Results of these simulations are plotted in Figure 8. Notice that for $\omega_o \cdot \tau_f \leq 0.2$ there is only a moderate change in the distortion.

Now consider the case where $\tau_f = 0$ but $r_b \neq 0$. Since $\tau_f = 0$, the transition time lengthening due to $r_b \cdot C_b$ does not exist. However, there is another time constant to consider: $r_b \cdot C_{je}$. As $\omega_o \cdot r_b \cdot C_{je}$ approaches unity, significant lengthening of the transition time does occur. Note that $r_b \cdot C_{je}$ is approximately independent of current density, so this effect occurs at both high and low current densities. However, at high current densities the effect of $r_b \cdot C_b$ swamps any small effect of $r_b \cdot C_{je}$ since $C_b >> C_{je}$ during the transition time. At low current densities this is not necessarily the case. Figure 9 shows the distortion vs. $\omega_o \cdot C_{je} \cdot V_T / I_Q$ for $\omega_o \cdot r_b \cdot C_{je} = 0$ and 0.4. Notice that the dependence of the distortion on $\omega_o \cdot r_b \cdot C_{je}$ is fairly weak.

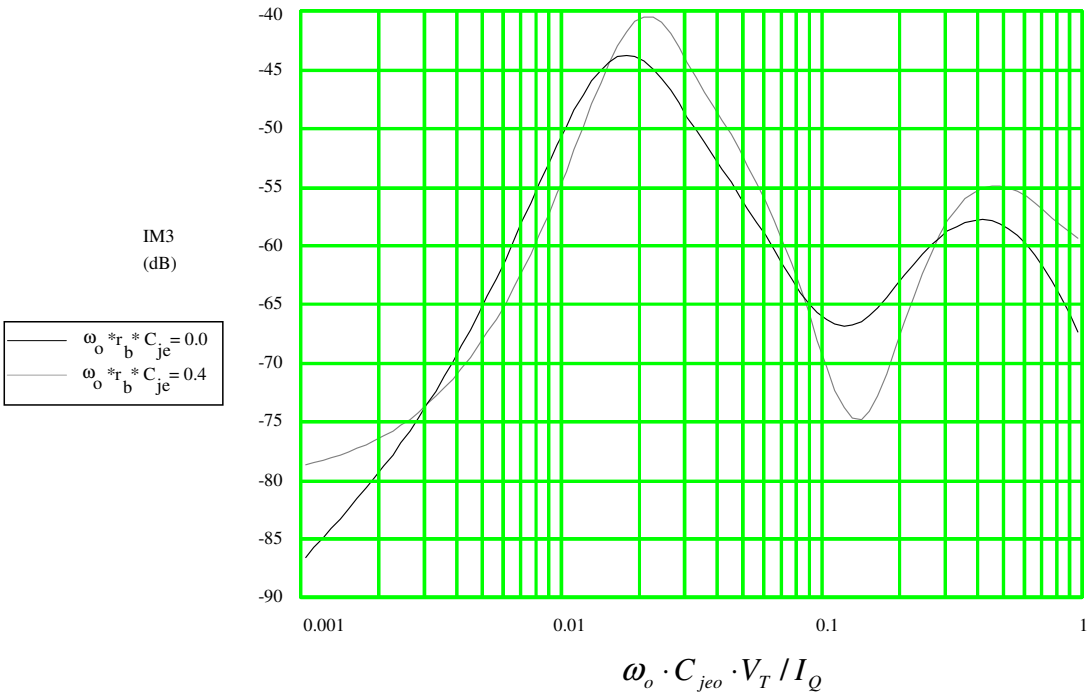

Figure 9: Distortion vs. $\omega_o \cdot C_{je} \cdot V_T / I_Q$ for $\omega_o \cdot r_b \cdot C_{je} = 0,0.05,0.4$

8.5: Distortion At Moderate Current Density

Simulations indicate that the distortion at moderate current densities is approximately equal to the sum of the distortions created by the high and low current densities mechanisms. That is, the two mechanisms generate distortion with the same phase.

$$IM3_{tot} \approx IM3\left[\omega_o \cdot \tau_f \cdot \frac{r_b \cdot I_Q}{V_T}\right]_{C_{je}=0} + IM3\left[\omega_o \cdot C_{je} \cdot \frac{V_T}{I_Q}\right]_{r_b,\tau_f=0} \tag{6a}$$

Using Equations 22a&b from Chapter 6:

$$IM3_{tot} \approx IM3\left[K \cdot \frac{\omega_o}{\omega_x}\right]_{C_{je}=0} + IM3\left[\frac{1}{K} \cdot \frac{\omega_o}{\omega_x}\right]_{r_b,\tau_f=0} \tag{6b}$$

where ω_x and K are given by Equations 21a&b in Chapter 6. As the current-density factor (K) increases the distortion due to the first term increases, and the distortion due to the second term decreases (at least for small values of $\omega_o \cdot C_{je} \cdot V_T / I_Q$). Therefore there is a tradeoff, and a minimum in the distortion is expected for some moderate current densities. In addition, a second minimum occurs for very low current density as is shown in Figure 7.

To verify Equations 6a&b, simulations were run with a complete bipolar transistor model. The current was held constant, and the device area was varied over three orders of magnitude. As the device area increases, the current density decreases. The minimum size device in the process has parameters:

$$I_s = 2.43 \cdot 10^{-18}\,\text{A}$$

$$r_{bo} \approx 950\Omega\,@\,I_C = 40\mu A$$

$$C_{jeo} = 5.9\text{fF}, M_{je} = 0.41, V_{je} = 0.895$$

$$\tau_f = 11\text{ps}$$

Using Equation 4 and the ideal exponential law, the emitter-base junction capacitance for 40 μA of forward-bias current is:

$$C_{je} = 14.3\text{fF}$$

$$r_b \cdot C_{je} \approx 13.5\text{ps}$$

From Equation 21a of Chapter 6:

$$f_x = \frac{\omega_x}{2 \cdot \pi} \approx 13.1\text{GHz}\,.$$

The actual value of f_x is slightly dependent on current density. However, the effect of the increase in value of C_{je} with current density tends to be canceled by the reduction of r_b . For this process the value of f_x is close to the peak f_T.

Simulations were run at LO frequencies of 1,2, and 4 GHz. This corresponds to values of ω/ω_x = 0.075, 0.15, 0.30. For these simulations, the LO amplitude is set to 1V, as variations from theory seem to be largest when the LO amplitude is large. The total current, I_Q, was set to 1mA. The device area was varied from a 1x (minimum size) to a 1000x device.

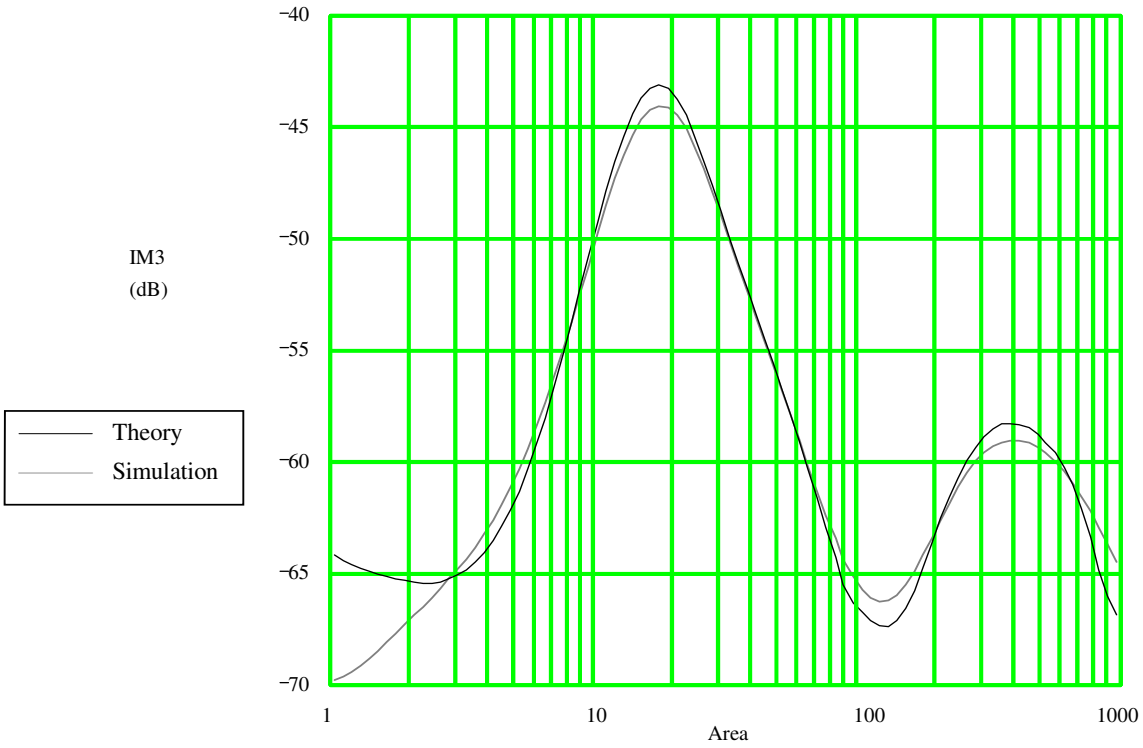

Figure 10a: Distortion Vs Device Area for $\omega/\omega_x = 0.075$ and $V_{LOA} = 1\text{V}$

The peak f_T of the minimum size device occurs at a bias current of 0.4mA. Therefore, for device areas smaller than 2.5x the current density is high and the Kirk Effect is expected to modify the level of distortion.

For this process and bias current, the current-density factor is related to device area by:

$$K \equiv \frac{r_b \cdot I_Q}{V_T} \cdot \sqrt{\frac{\tau_f}{r_b \cdot C_{je}}} \approx \frac{13.3}{A}$$

For $\omega / \omega_x = 0.075$ (Figure 10a) the value predicted by Equation 6 is very close to the simulated value over a wide range of areas. However, for device areas less than 3x (high current densities) there is a significant deviation. This deviation is due to the Kirk effect (which causes τ_f to increase at high current densities). The slight deviation in the minimum (near area=20x) and maximum (near area=150x) are due to the fact that $\omega_o \cdot \tau_f \neq 0$ (see Figure 8).

For $\omega / \omega_x = 0.15$ (Figure 10b) the value predicted by Equation 6 matches the predicted value within a couple of dB over the full range of current densities.

For $\omega / \omega_x = 0.30$ (Figure 10c) significant variations begin to appear at low current densities (large areas). The reason for this is that both $\omega_o \cdot \tau_f$ and $\omega_o \cdot r_b \cdot C_{je}$ are no longer much less than unity. However, the basic shape is fairly accurate and the distortion prediction for higher current densities is quite accurate.

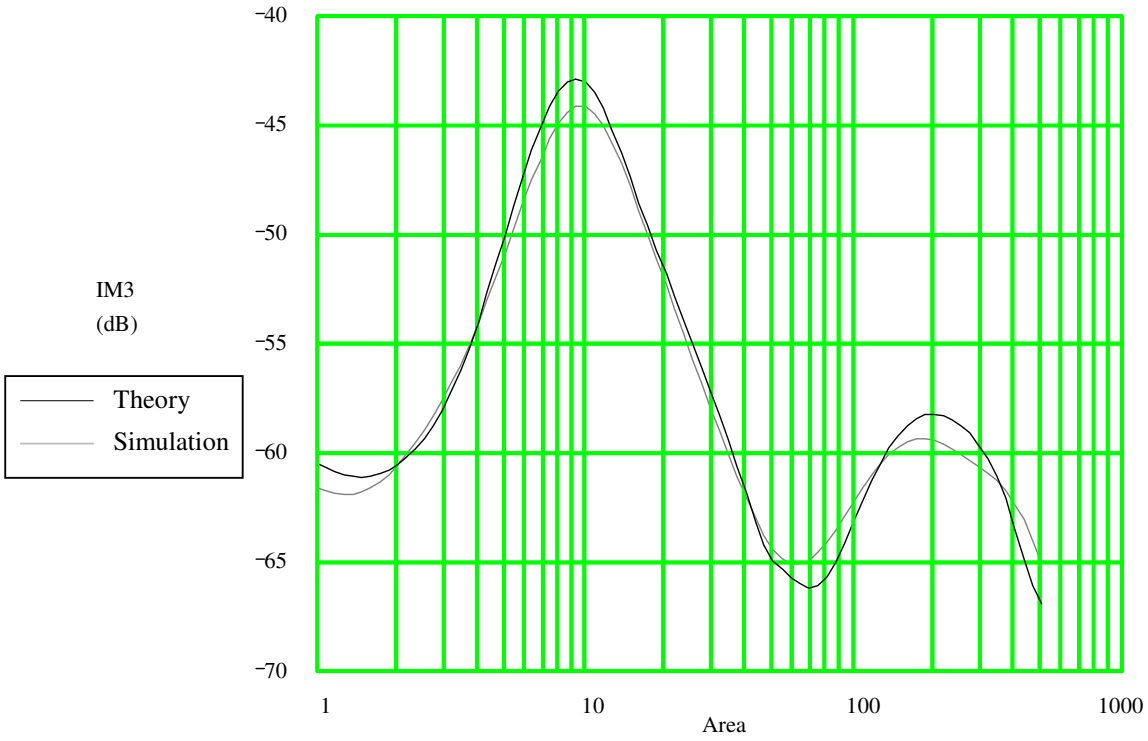

Figure 10b: Distortion vs. Device Area for $\omega/\omega_x = 0.15$ and $V_{LOA} = 1\text{V}$

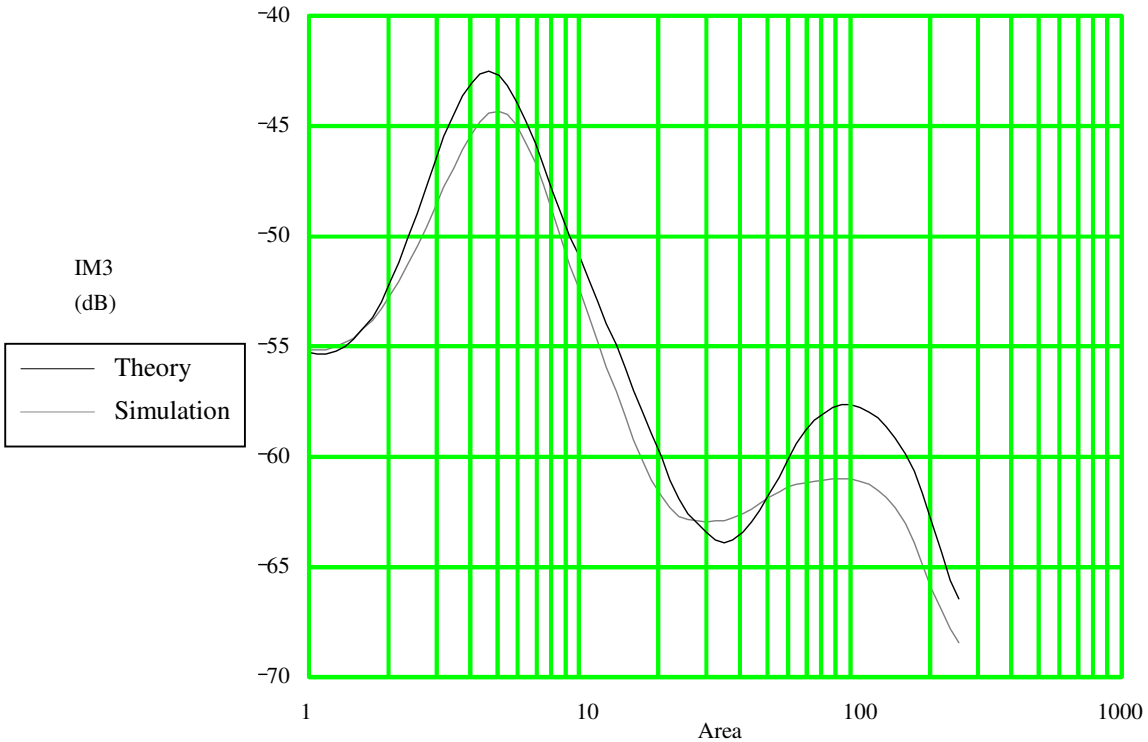

Figure 10c: Distortion vs. Device Area for $\omega/\omega_x = 0.3$ and $V_{LOA} = 1\text{V}$

For large LO amplitudes the C_{je} distortion mechanism tends to dominate at current densities up to that where the peak f_T occurs. For smaller LO amplitudes the r_b distortion mechanism becomes important at moderate to high current densities. To investigate the accuracy of Equation 6 under the condition where both distortion mechanisms are significant, simulations were done for $V_{LOA} = 178\text{mV}$ and $\omega/\omega_x = 0.075$. The results are shown in Figure 11. Note that the exact location of the minimum is off significantly, but the maximum error in the distortion prediction is about 3 dB.

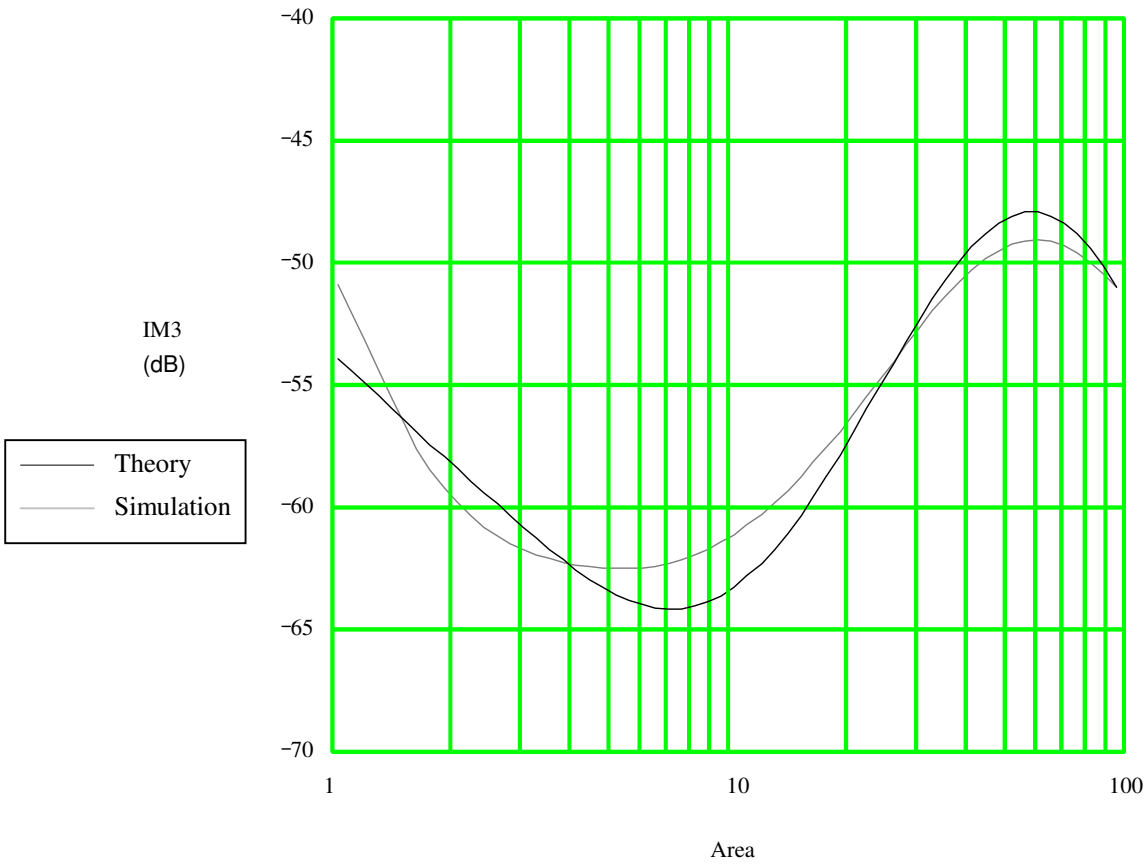

Figure 11: Distortion vs. Device Area for $\omega/\omega_x = 0.075$ and $V_{LOA} = 178\text{mV}$

8.6: Linearity Optimization

From Equation 6b it is seen that for a given frequency and process, the distortion is only a function of the current-density factor and the LO power. In Figures 12a,b,c the dependency of distortion on the current-density factor is plotted for values of $\omega/\omega_x = 0.05$, 0.1, and 0.2 respectively.

In Figure 12a, the distortion is plotted against current density for $\omega/\omega_x = 0.05$. As expected, there are two minimums. At very low current density there is a minimum. This minimum is discussed in the section on low current density. There is a second minimum that exists for current-density factors in the range of 5-12, depending on the LO power. These minima represent a compromise between the two types of distortion mechanisms (i.e. the transition time and non-transition time mechanisms). As the LO power is increased, the optimum current-density factor increases. The reason for this is that increasing the LO power generally increases the non-transition time distortion and decreases the transition time distortion.

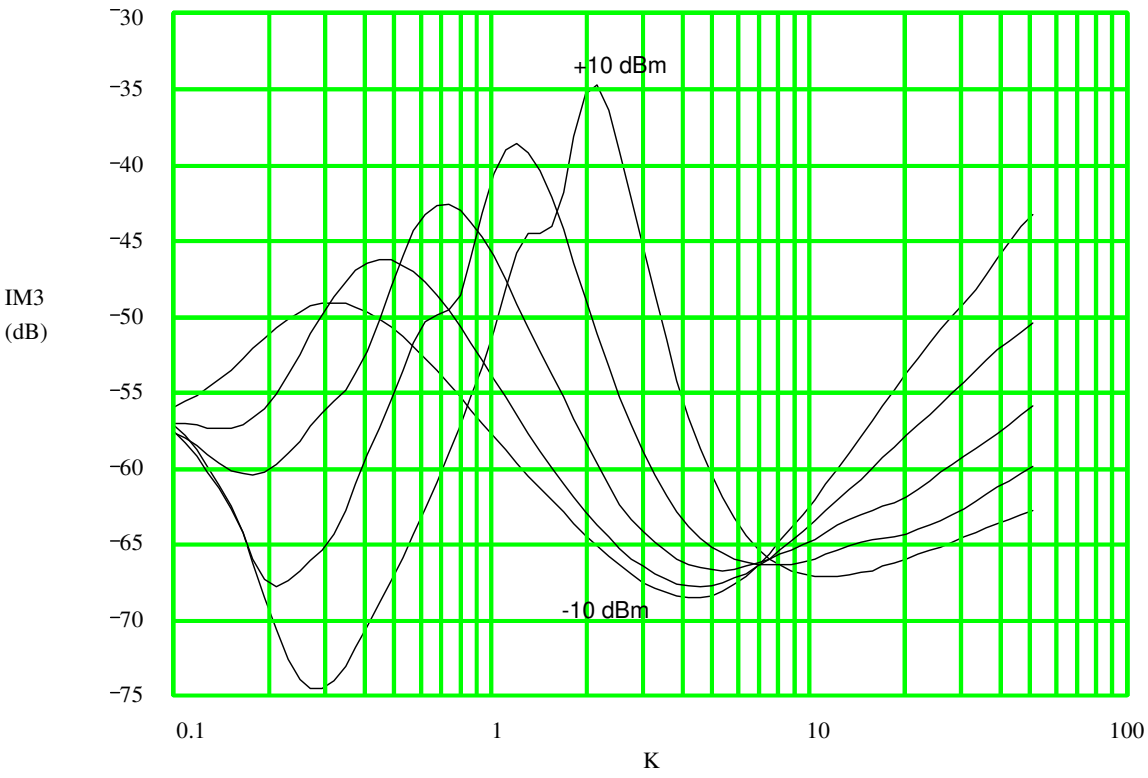

Figure 12a: Distortion vs. Current-density factor for $\omega/\omega_x = 0.05$

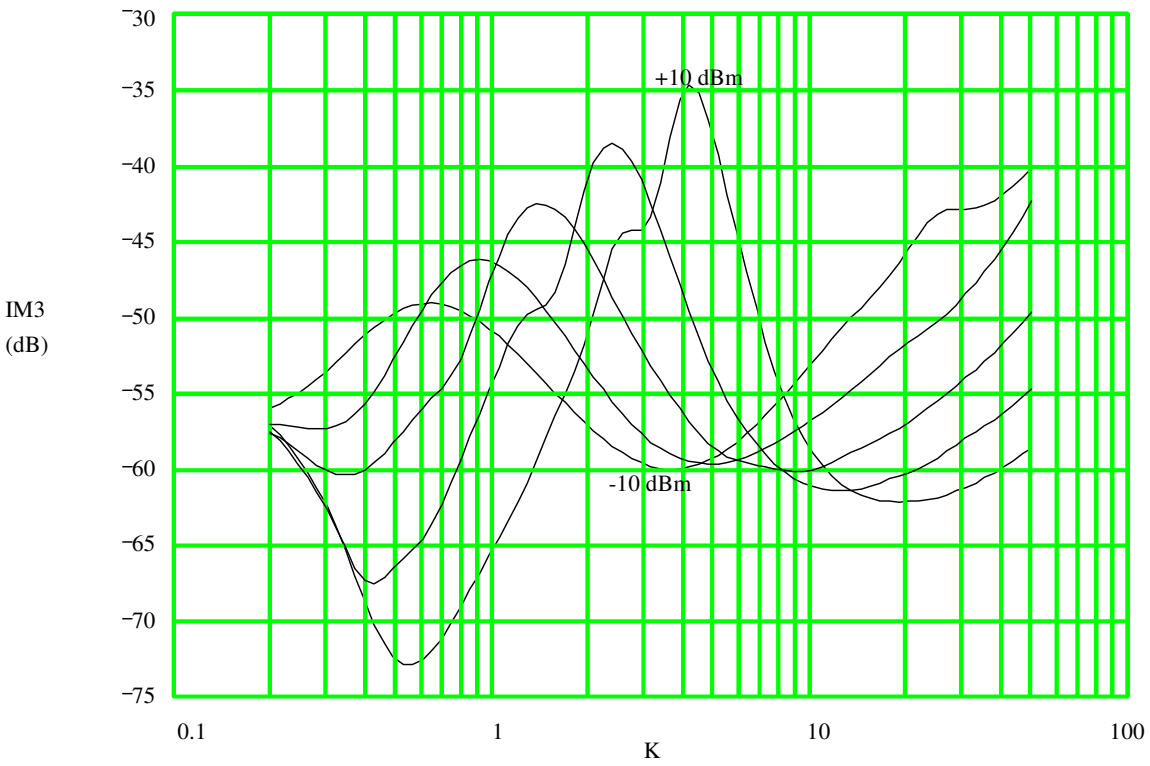

Figure 12b: Distortion vs. Current-density factor for $\omega / \omega_x = 0.1$

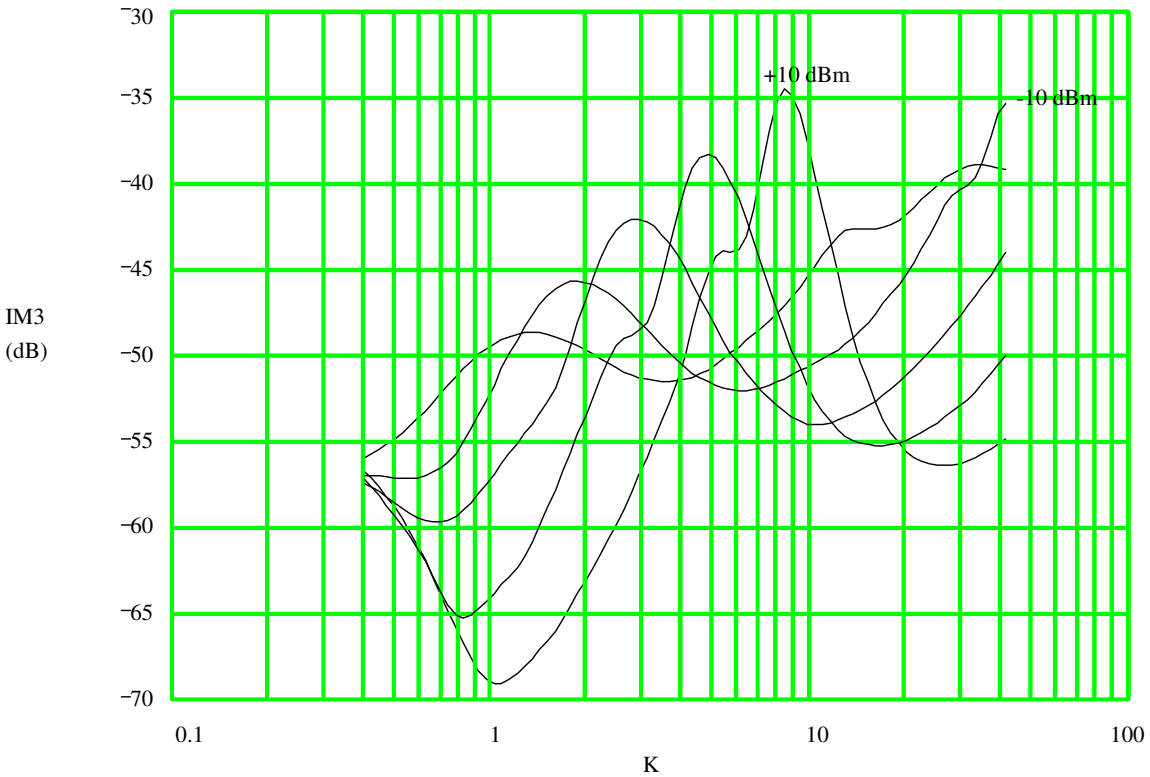

Figure 12c: Distortion vs. Current-density factor for $\omega / \omega_x = 0.2$

In Figure 12b, the distortion is plotted against current-density factor for $\omega/\omega_x = 0.1$. With an increase in frequency, an increase in current-density is required if a large LO amplitude is used. However, for weak LO amplitudes, the optimum value of K actually decreases. The reason for this is that the amount of "excess distortion" during non-transition times is substantially worse for large LO amplitudes. Thus, with large LO amplitudes, an increasingly higher current density is required as the frequency is increased. The general trend continues as ω/ω_x increase to 0.2 (Figure 12c).

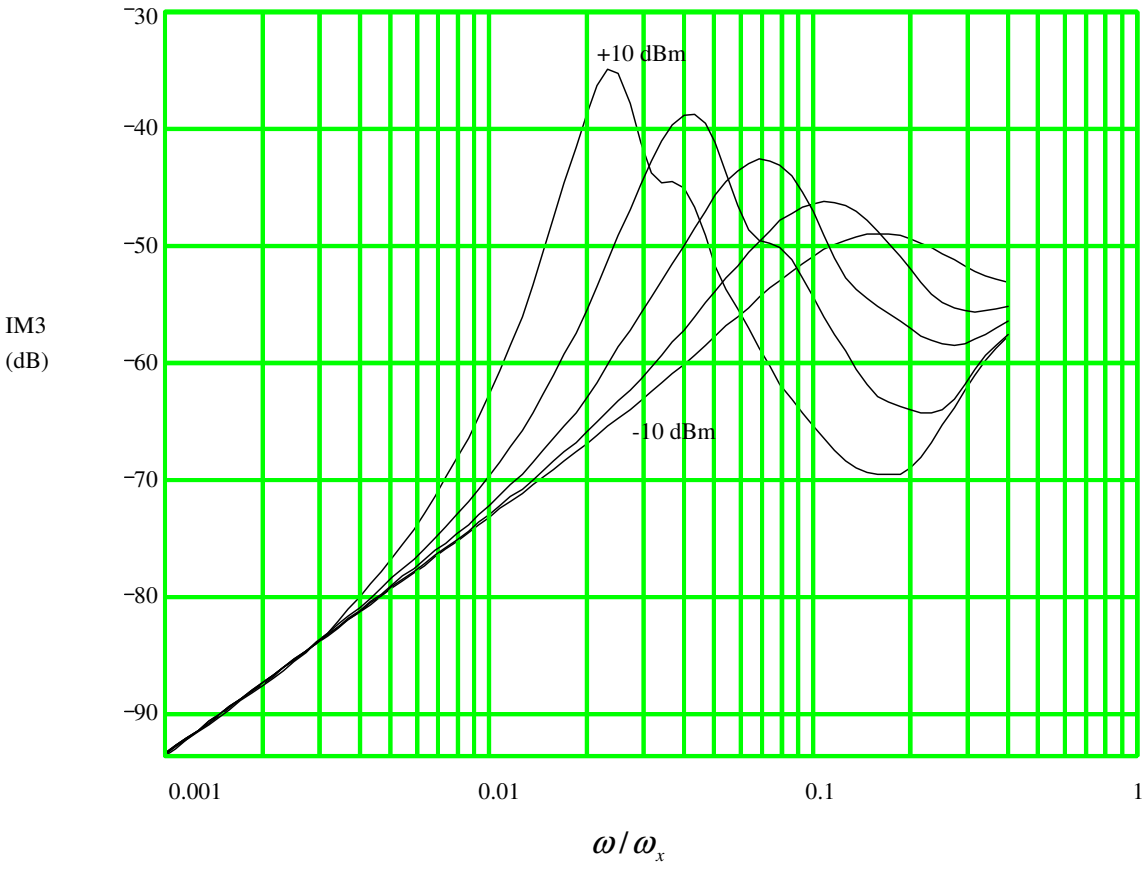

Figure 13a: Distortion vs. Frequency for K=1

It is interesting to see how distortion varies with frequency for a fixed current-density factor. In Figures 13a,b,and c, the distortion is plotted against frequency for K=1,3, and 10 respectively.

For K=1 (Figure 13a) the distortion curves appear nearly identical to those in Figure 2. At such a low a current-density factor, the transition time distortion mechanism is insignificant.

For K=3 (Figure 13b) the overall distortion decreases, and the dips and peaks occur at higher frequencies. This is because the waveform "tilting" has been reduced by the reduced value of C_{je}. The increase of the transition-time distortion mechanism does not yet seem significant.

For K=10 (Figure 13c) the situation has changed significantly. The distortion has increased at some LO powers and frequencies, and reduced for others. The effect of waveform "tilting" is not apparent until very high frequencies. The distortion appears to be fairly independent of LO power, and seems to be increasing at a rate of about 30 dB per decade.

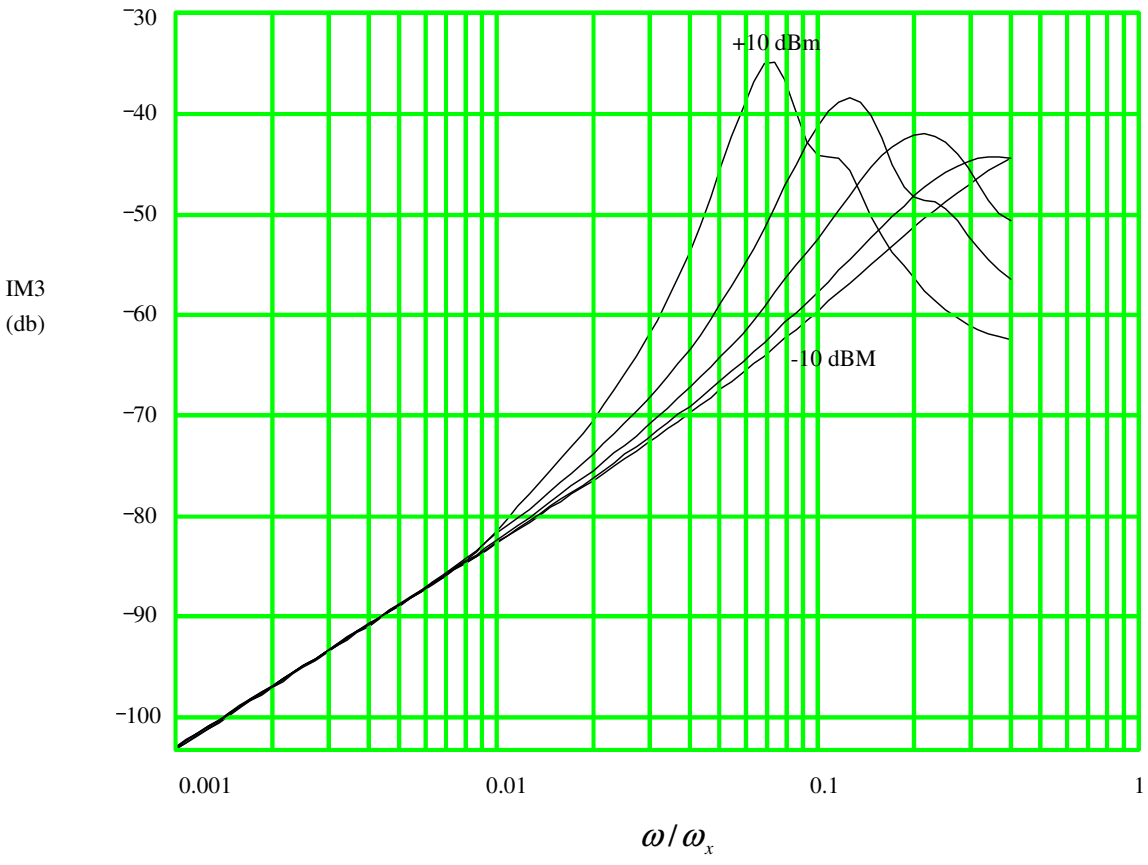

Figure 13b: Distortion vs. Frequency for K=3

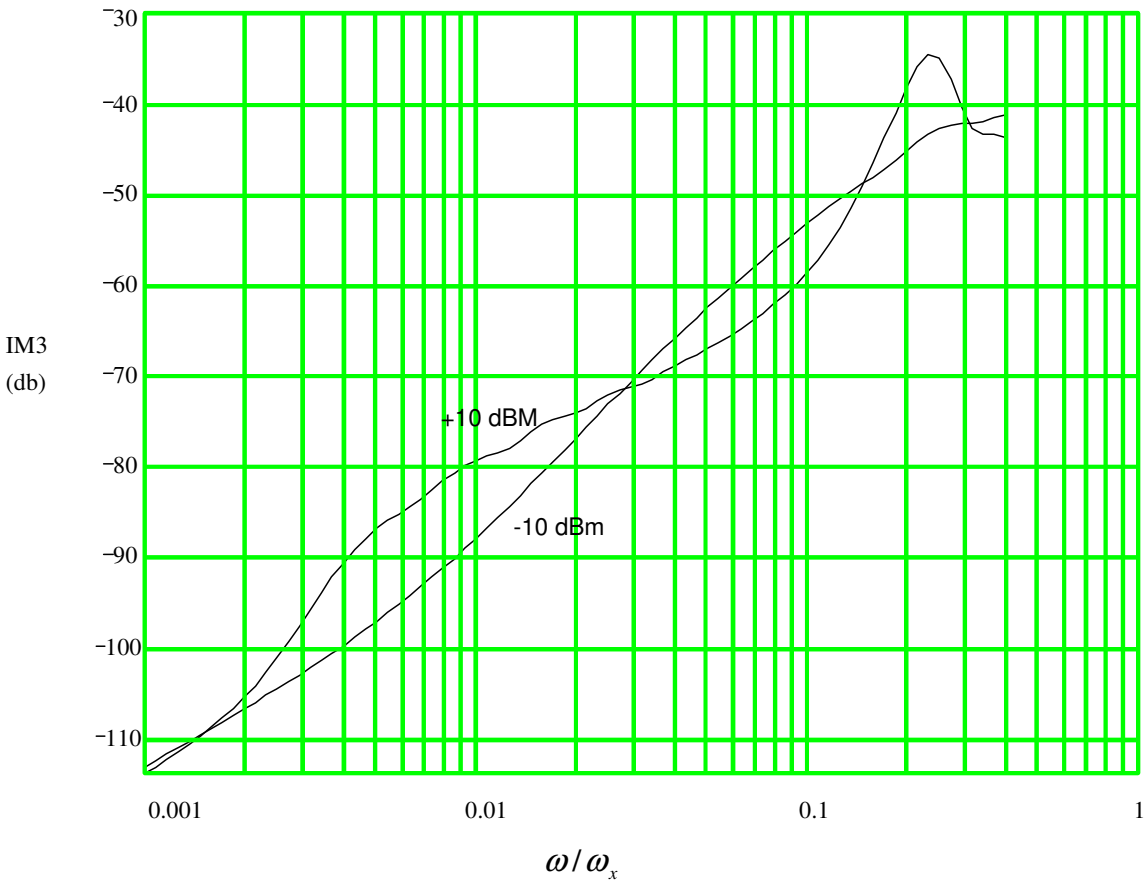

Figure 13c: Distortion vs. Frequency for K=10

Chapter 9: Calculating Mixer Noise Figure

In Chapter 7 the focus was on calculation of mixer output noise. However, noise figure is a more common figure of merit for both amplifiers and mixers. In this chapter the single-sideband noise figure is used to characterize mixer noise performance. Single-sideband noise figure is the noise figure that is obtained by assuming that input signals at the image frequency are blocked by ideal filters. Double-sideband noise figure is used to describe a system which has signal power coming both above and below the LO frequency. Double-sideband noise figure is generally about 3dB better than single-sideband noise figure, because of the increased power level of the incoming signal.

From Chapter 3, the noise figure is defined as

$$F = \frac{(S/N)_{in}}{(S/N)_{out}}$$

In a mixer, the output signal-to-noise ratio is measured at the IF frequency. The input signal-to-noise ratio is measured at the signal frequency. The noise figure may be expressed as

$$F = \frac{{i_{odn}}^2(\omega_{if})}{4 \cdot K \cdot T / R_s \cdot \Delta f} \cdot \frac{1}{\left[i_{out}(\omega_{if}) / i_s(\omega_s)\right]^2} \tag{1a}$$

which may be written as

$$F = \frac{{i_{odn}}^2(\omega_{if})}{4 \cdot K \cdot T / R_s \cdot \Delta f} \cdot \frac{1}{{a_{ic}}^2} \tag{1b}$$

where a_{ic} is the current conversion-gain which is defined by

$$a_{ic} \equiv \frac{i_{out}(\omega_{if})}{i_s(\omega_s)}$$

If Equations 5a and 7b of Chapter 7 are added, the total output noise of an emitter-coupled pair mixer is given by:

$${i_{odn}}^2 = {i_{idn}}^2 \cdot f_3 + 2 \cdot q \cdot I_Q \cdot \Delta f \cdot \left[f_1 + \frac{r_b \cdot I_Q}{V_T} \cdot f_2 \right] \tag{2}$$

In this context i_{idn} refers to the noise that is injected into the switching portion of the mixer, and is the output noise of the driver. Equations 2 and 3 assume that the output noise of the driver is white, but this is not always the case. As a first-order approximation it is assumed that the noise sources in the driver yield

white noise at the output, but that the noise from the source is narrowband (as is implicit in the concept of single-sideband noise figure). Under these assumptions, the noise figure can be written as

$$F \approx 1 + \frac{{i_{drv}}^2 \cdot f_3}{4 \cdot K \cdot T / R_s \cdot \Delta f} \cdot \frac{1}{{a_{ic}}^2} + \frac{I_Q \cdot R_s}{2 \cdot V_T} \cdot \frac{1}{{a_{ic}}^2} \cdot \left[f_1 + \frac{r_b \cdot I_Q}{V_T} \cdot f_2 \right] \tag{3}$$

where i_{drv} is the white noise portion of the driver's output noise. That is, it does not include the noise from the source.

If the noise figure of the driver is given by F_{dr}, then the total mixer noise figure may be written:

$$F \approx 1 + (F_{dr} - 1) \cdot \frac{f_3}{{a_{ic}}^2} + \frac{I_Q \cdot R_s}{2 \cdot V_T} \cdot \frac{1}{{a_{ic}}^2} \cdot \left[f_1 + \frac{r_b \cdot I_Q}{V_T} \cdot f_2 \right] \tag{4a}$$

The conversion gain is the product of the current gain of the driver and the current conversion-gain of the mixer. That is

$$a_{ic} = a_{id} \cdot a_{icm}$$

where

$$a_{id} \equiv \frac{i_{od}(\omega_s)}{i_s(\omega_s)}$$

$$a_{icm} \equiv \frac{i_{out}(\omega_{if})}{i_{od}(\omega_s)}$$

and the noise figure can be expressed as:

$$F \approx 1 + \frac{(F_{dr} - 1)}{{a_{id}}^2} \cdot f_4 + \frac{1}{{a_{icm}}^2 \cdot {a_{id}}^2} \cdot \frac{I_Q \cdot R_s}{2 \cdot V_T} \cdot \left[f_1 + \frac{r_b \cdot I_Q}{V_T} \cdot f_2 \right] \tag{4b}$$

$$f_4 \equiv \frac{f_3}{{a_{icm}}^2}$$

The function f_4 is shown (at low frequencies) in Figure 6a of Chapter 7.

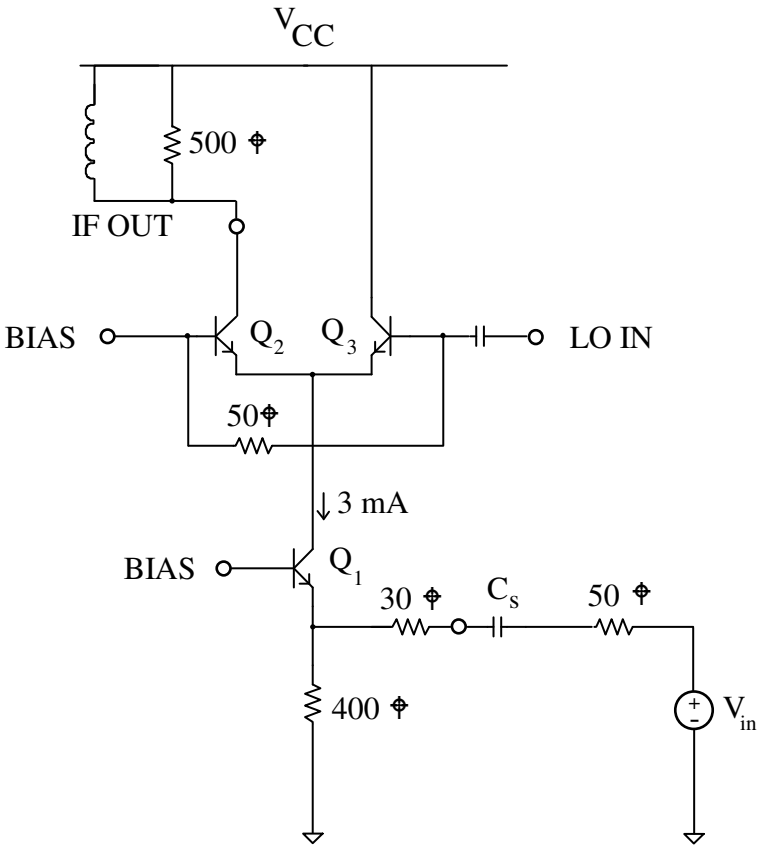

Figure 1 : Schematic of Single-Balanced Mixer Configuration

9.1: Design Example

Consider the circuit that was analyzed in Chapter 5. The techniques used in Chapter 5 were optimized for the exact circuit. It is interesting to see how accurate a noise figure Equation 4b will yield. Transistor Q_1 has an area of 24x, and transistors Q_2 and Q_3 have areas of 4x. The device parameters are as follows:

$$r_{b2} = r_{b3} = 83\Omega$$

$$C_{jeo2} = C_{jeo3} = 60\text{fF}$$

$$C_{js1} + C_{jc1} = 120\text{fF}$$

$$r_{b1} = 15\Omega$$

$$\tau_f = 11\text{pS}$$

For forward bias:

$$C_{je2} = C_{je3} \approx 150\text{fF}$$

$$C_{je1} = 1\text{pF}$$

$$\omega_o = 2 \cdot \pi \cdot 1\text{GHz}$$

$$I_Q = 3.16\text{mA}$$

Then it follows that:

$$\omega_o \cdot \left[C_{je} + \frac{C_x}{2} \right] \cdot \frac{V_T}{I_Q} = 0.014$$

$$\omega_o \cdot \tau_f \cdot \frac{r_b \cdot I_Q}{V_T} = 0.7$$

The conversion gain is calculated using the data presented in Chapter 6. Using to Figure 6 of Chapter 6, with $\omega_o \cdot \left[C_{je} + C_x / 2 \right] \cdot V_T / I_Q = 0.014$, we see that the conversion gain is unchanged from its value when that parameter is zero. Therefore the conversion gain is given by Figure 4 of Chapter 6.

Examination of Figure 12a of Chapter 7 indicates that the parameter $\omega_o \cdot \left[C_{je} + C_x / 2 \right] \cdot V_T / I_Q$ = 0.14 does not significantly affect the shot noise. However, there is a small change in the base-ohmic noise rejection at high LO powers. The change for LO power of +10dBm is -2.0dB and for +5 dBM it is -0.5 dB. Table 2 includes these corrections.

Table 1: Performance for $\omega_o \cdot \tau_f \cdot r_b \cdot I_Q / V_T = 0.7$

LO POWER	base-ohmic noise rejection: f_2	shot noise rejection : f_1	conversion gain: a_{icm}	relative white noise gain, f_4
-10 dBm	-6.5 dB	-4.0 dB	-5.3 dB	7.3 dB
-5 dBm	-10 dB	-6.5 dB	-4.2 dB	6.8 dB
0 dBm	-13 dB	-8 dB	-4.0 dB	6.7 dB
+5 dBm	-16 dB	-9.5 dB	-4.0 dB	6.8 dB
+10 dBm	-19.5 dB	-12 dB	-4.0 dB	6.9 dB

Table 2: Performance for $\omega_o \cdot \tau_f \cdot r_b \cdot I_Q / V_T = 0.7$ and $\omega_o \cdot (C_{je} + C_x / 2) \cdot V_T / I_Q = 0.014$

LO POWER	base-ohmic noise rejection: f_2	shot noise rejection : f_1	conversion gain: a_{icm}	relative white noise gain, f_4
-10 dBm	-6.5 dB	-4.0 dB	-5.3 dB	7.3 dB
-5 dBm	-10 dB	-6.5 dB	-4.2 dB	6.8 dB
0 dBm	-13 dB	-8 dB	-4.0 dB	6.7 dB
+5 dBm	-16.5 dB	-9.5 dB	-4.0 dB	6.8 dB
+10 dBm	-21.5 dB	-12 dB	-4.0 dB	6.9 dB

From Figure 3 of Chapter 4, the noise figure of the common-base driver is 4.1 dB, and the current gain as defined in this chapter is :

$$a_{id} = \frac{i_{od}(\omega_s)}{i_s(\omega_s)} = \alpha(j \cdot \omega) \cdot \frac{i_{in}(\omega_s)}{i_s(\omega_s)} = \frac{\alpha(j \cdot \omega) \cdot R_s}{R_s + R_{in}} \approx \frac{1}{2}$$

Table 4: Calculated vs. Measured Noise Figure

LO Power	Calculated Noise Figure	Measured Noise Figure
-10 dBm	21.4 dB	21.2 dB
-5 dBm	18.1 dB	16.0 dB
0 dBm	16.5 dB	14.0 dB
+5 dBm	15.4 dB	13.0 dB
+10 dBm	14.7 dB	N/A

The calculated and measured noise figures for the mixer in Figure 1 are tabulated in Table 4. The calculated noise figure is higher than the measured one (or that predicted in Chapter 5). The error in the calculation is due to the assumption that the driver's output noise is white. In fact, the output noise of the driver is not white (by design) and this helps reduce the noise figure. The use of "noise shaping" where one attempts to reduce the noise at non-signal frequencies is described below.

9.2: Noise Shaping

Because of the mixer nonlinearities, there are a number of frequencies at the input port which are translated to the IF frequency at the IF port. These frequencies (as is shown in Chapter 5) are:

$$\omega_{in} = n \cdot \omega_o + m \cdot \omega_{if}$$

where n is any integer and m is -1,0 or +1. Single-balanced mixers reject the term with either n=0 or m=0, but not both. Double-balanced mixers reject both the n=0 and m=0 terms. The three frequencies that contribute most of the noise to the output are:

$$\omega_{in} = \omega_o \pm \omega_{if}$$ (the signal and image frequency)

and

$$\omega_{in} = \omega_{if}$$

It is impossible to filter out the noise at the signal frequency without affecting the signal. It is quite difficult (though possible) to affect the noise at the image frequency. However, it is often quite easy to reduce the driver's output noise at the IF frequency, since the IF frequency is much lower than the signal frequency.

Referring to Figure 1, we see that if the blocking capacitor, C_s, is sufficiently small that it has a high impedance at ω_{if}, than the emitter of Q_1 will see approximately 400 ohms to ground. This is much higher than the 80 ohms seen at the signal frequency, and hence, the output noise at the IF frequency will be reduced substantially because of the increased emitter degeneration at that frequency. In the limiting case where the output noise at the IF frequency goes to zero, the noise performance of the single-ended output (single-balanced) mixer is identical to the double-balanced mixer.

9.3: Calculation of Mixer Input Third-Order Intercept

Calculation of the intercept point for the mixer requires knowledge of the distortion in the driver and switch. Distortion in the three common driver configurations is derived in Chapters 3 and 4. Distortion in the switching portion of the mixer for an ECP switch is discussed in Chapter 8.

Exact calculation of the distortion requires knowledge of the phase relationships between the various harmonics created by the nonlinearities. In addition to that, second-order interaction can change the overall system distortion. An approximate value of the total distortion can be obtained by assuming that the 3rd order distortions combine in phase and that the second-order interaction is negligible. Strictly speaking, this does not give an upper bound to the distortion, since it neglects the second-order interaction. In driver designs that have very little second-order distortion (such as the emitter-coupled pair), it is reasonable to assume that second-order interaction is negligible. In other driver designs (such as the common-emitter and the common-base) substantial second-order distortion exists and, in combination with the second-order nonlinearities of the switch, may significantly change the overall mixer intercept point.

Under the assumption that the third-order distortion components add in phase and there is no significant second-order interaction, the mixer intercept point can be calculated from the driver intercept point by:

$$\frac{1}{IP3_{mix}{}^2} = \frac{1}{IP3_{drv}{}^2} + \frac{1}{IP3_{swt}{}^2 \cdot a_{id}{}^2}$$

this is easily seen to be true by noting that:

$$IP3 \propto 1/\sqrt{IM3}$$

The above analysis assumes that the intercept point is expressed as either a voltage or current. If it is expressed as a power then one adds the inverses rather than the square of the inverses to get the total intercept point.

9.4: Distortion for the Design Example

Consider the circuit configuration of Figure 1. As discussed previously, at 1 GHz:

$\omega_o \cdot \tau_f \cdot r_b \cdot I_Q / V_T = 0.7$ and $\omega_o \cdot (C_{je} + C_x/2) \cdot V_T / I_Q = 0.014$

Table 5: Switch Distortion at 20% modulation

LO POWER	Distortion due to C_{je}	Distortion due to r_b	Total switch distortion	3rd Order Intercept (input)
-10 dBm	-70 dB	-59 dB	-57 dB	14.5 dBm
-5 dBm	-70 dB	-62 dB	-59 dB	15.5 dBm
0 dBm	-68 dB	-64 dB	-60 dB	16.0 dBm
+5 dBm	-63 dB	-66 dB	-58 dB	15.0 dBm
+10 dBm	-50 dB	-69 dB	-49 dB	10.5 dBm

From Figure 4 of Chapter 4, a common-base design with $C_{je} \approx 1/2 \cdot \omega_o \cdot R_s$ and 3mA of bias current has a third-order intercept point of +10 dBm.

Table 6: Predicted and Measured 3rd Order Intercept of Mixer.

LO POWER	3rd Order Intercept of Mixer (predicted)	3rd Order Intercept of Mixer (measured)
-10 dBm	8.5 dBm	4.0 dBm
-5 dBm	9.0 dBm	6.0 dBm
0 dBm	9.0 dBm	6.0 dBm
+5 dBm	8.5 dBm	4.0 dBm
+10 dBm	7.0 dBm	N/A

9.5: Front-End Design for Optimum Dynamic Range

The overall goal for a receiver front-end is to obtain as wide a dynamic range as possible with a given power level. Alternatively, one may wish to minimize the power consumption subject to dynamic range constraints.

When power consumption is a consideration, design simplicity is a considerable virtue. Any unnecessary active stages consume additional power. In addition, these stages will add additional noise and distortion components. As seen in previous chapters, there may be some performance advantages to increasing the complexity of a design. For example, balanced mixers tend to reject noise at certain input frequencies, and may improve the mixer noise figure. An image rejection mixer may also improve the noise performance, and reduce the filtering complexity. The designer must carefully consider whether the performance (and reduced filtering requirements) gained by using these more complex structures offsets the increased power consumption. For example, using a double-balanced mixer will increase the power consumption by a factor of two. If the dynamic range is increased by more than 3dB than it is probably worth using a double-balanced mixer. Quite often, careful filter design will allow a single-balanced mixer to achieve comparable performance to a double-balanced mixer. In this case, the designer must decide if the

reduced cost of simpler filtering offsets the increased power consumption (or decreased performance for a given power level).

One of the most important front-end specifications is the overall gain desired. This gain should only be enough to overcome any noise that may occur during the IF signal processing. Excessive gain will lead to a poor input intercept point for the front-end.

Once the gain of the system is set, the designer must choose the distribution of the gain between the preamp and mixer. The mixer gain is primarily determined by the driver type. A common-emitter driver will have high gain, whereas a common-base stage has relatively low gain. Thus, a common-base driver will require a high-gain preamp.

As is discussed in Chapters 3 and 4, the common-emitter stage exhibits excellent linearity and noise characteristics in the 1-3 GHz range (for a device $f_T = 10\text{GHZ}$). In addition, a simpler preamp may be used since less gain is required for that stage. If a common-emitter driver is used, than a single-stage common-emitter preamp will often be sufficient to meet system noise and gain specifications.

A common-base driver is more desirable at low frequencies, where it excels in linearity. Common-base drivers also offer constant gain over a very wide bandwidth, and are convenient for general purpose mixers. A high-gain preamp is necessary if a low noise figure is desired. Such a preamp will generally require at least two active transistors, and thus will consume a significant amount of power. A wideband feedback amplifier may be used for the preamp in a front-end designed to operate over a wide range of frequencies.

In optimizing the switching portion of the mixer one must choose the LO power and the device size. The choice of device size and LO power is interdependent. Use of large LO amplitudes requires a device operating at a higher current density (i.e. a smaller device). Increasing the LO power and the current-density together generally yields improved dynamic range. However, at very high current densities (small switching devices), parasitics at the collector of the driving device substantially degrade performance. If the driver devices are scaled down with the switching devices, then the driver noise figure is degraded. Hence, an optimum LO power exists, but in depends on the characteristics of the device parasitics and the driver design.

For a common-emitter driver a very large device is used. Such a large device has substantial parasitics at the collector. In this case a weaker LO with large switching devices seems reasonable. Because of the high current gain of the common-emitter stage, much of the noise comes from the common-emitter. The increase in switching noise (because of the weaker LO) does not substantially degrade the overall mixer performance. However, switch linearity is critical. Thus, when a common-emitter driver is used, the switch device sizes should be optimized for minimum distortion. Figures 12a,b,&c of Chapter 8 are useful in determining the optimum current density factor for minimum distortion.

For a common-base driver the dominant noise source is the switch. Hence, smaller driver devices should be used, so that driver linearity and switch linearity are maximized (since decreasing the parasitic capacitances will decrease the distortion in the common-base stage and the switch). Choosing the device sizes for the switch involves a compromise between optimum linearity and optimum noise. Unfortunately, the emitter-coupled pair switch reaches a maximum in distortion when the noise is minimized. This situation occurs when $\omega_o \cdot C_{je} \cdot V_{LOA} / I_Q \approx 1$. In general, the device size must be chosen so that $\omega_o \cdot C_{je} \cdot V_{LOA} / I_Q < 1$ so that the distortion is not too high. However, decreasing the device size to meet this criterion will increase the noise. A compromise must be chosen between the device size that gives minimum noise and minimum distortion. The exact choice depends on the preamp gain and the overall system requirements.

Conclusion

Optimization of the performance of low-noise amplifier and mixer stages in the front end of a receiver have been discussed. Behavior of both noise and distortion in commonly used amplifier and mixer topologies has been examined. Optimum dynamic range has been shown to depend critically on the choice of device sizes. Careful distribution of gain between the preamp, mixer, and IF stages is also critical. Impedance matching and filtering requirements have also been discussed. Mixer and amplifier design examples have been presented.

[i] P.R. Gray and R.G. Meyer, *Analysis and Design of Analog Integrated Circuits, Second Edition.* p.692, Wiley, 1984.

[ii] P.R. Gray and R.G. Meyer, *Analysis and Design of Analog Integrated Circuits, Second Edition.* p.668, Wiley, 1984.

[iii] P.R. Gray and R.G. Meyer, *Analysis and Design of Analog Integrated Circuits, Second Edition.* p. 644-647, Wiley, 1984.G&M.

[iv] P.R. Gray and R.G. Meyer, *Analysis and Design of Analog Integrated Circuits, Second Edition.* pp.677-678.

[v] R.G. Meyer, *Noise in transistor mixers at high frequencies,* Proc. IEE, Vol. 115, No. 4, pp. 487-495, April 1968.

[vi] J. Wholey, I. Kipnis, and C. Snapp, *Silicon Bipolar Double Balanced Active Mixer MMIC's for RF and Microwave Applications up to 6 GHz,* 1989 Microwave and Millimeter-wave monolithic circuits Symposium Digest, pp.133-137.

[vii] J. Wholey, I. Kipnis, and C. Snapp, *Silicon Bipolar Double Balanced Active Mixer MMIC's for RF and Microwave Applications up to 6 GHz,* 1989 Microwave and Millimeter-wave monolithic circuits Symposium Digest, pp.133-137.

[viii] L.O. Chua, C.A. Desoer, and E.S. Kuh, *Linear and Nonlinear Circuits, Second Edition*, pp.727-731, McGraw-Hill, 1987.

[ix] REFERENCE TO CONVOLUTION FORMULA

[x] R.G. Meyer, *Intermodulation in High-Frequency Bipolar Transistor Integrated-Circuit Mixers,* Journal of Solid State Circuits, Vol 21, No. 4, pp. 534-537, August 1986.

[xi] E.A. Lee and D.G. Messerschmitt, *Digital Communication,* pp.46-47 Kluwer Academic Publications, 1988.

[xii] R.G. Meyer, *Intermodulation in High-Frequency Bipolar Transistor Integrated-Circuit Mixers,* Journal of Solid State Circuits, Vol 21, No. 4, pp. 534-537, August 1986.

[xiii] Reference to zero disto for ideal exponential AG